Petrological and geochemical constraints on the magmatic evolution at the Ampato-Sabancaya compound volcano (Peru)

Marco Rivera, Pablo Samaniego, François Nauret, Jersy Mariño, Céline Liorzou

Petrological and geochemical constraints on the magmatic evolution at the Ampato-Sabancaya compound volcano (Peru)

Marco RIVERA[1*], Pablo SAMANIEGO[2], François NAURET[2], Jersy MARIÑO[3] & Céline LIORZOU[4]

[1] Instituto Geofísico del Perú, Observatorio Vulcanológico del Sur, Asentamiento Humano José María Arguedas, Mz D, Lt 8, Sachaca, Arequipa, Peru

[2] Université Clermont Auvergne, Laboratoire Magmas et Volcans UMR 6524 CNRS & IRD R163, OPGC, Campus Universitaire des Cézeaux, 6 Avenue Blaise Pascal, TSA 60026 - CS 60026, 63178 Aubière Cedex, France

[3] Observatorio Vulcanológico del INGEMMET (Dirección de Geología Ambiental y Riesgo Geológico). Urb. Magisterial B-16, Umacollo, Arequipa, Peru

[4] Laboratoire Géosciences Océan, Institut Universitaire Européen de la Mer, Université de Bretagne Occidentale, Rue Dumont d'Urville, 29280, Plouzané, France

* Corresponding author

Instituto Geofísico del Perú, Observatorio Vulcanológico del Sur, Asentamiento Humano José María Arguedas Mz D, Lt 8, Sachaca, Arequipa, Peru (Phone and Fax: +51 952727739; e-mail: mrivera@igp.gob.pe)

Abstract

In order to gain insights into continental arc magmatic processes, we have conducted a petrological and geochemical study of major and trace elements and Sr, Nd, and Pb isotopes of the Ampato-Sabancaya compound volcano, which belongs to the Andean

Central Volcanic Zone (CVZ). Whole-rock compositions for Ampato and Sabancaya range from andesites to dacites (56.7–69.3 wt.% SiO_2) and both belong to a medium- to high-K calk-alkaline magmatic series. Ampato-Sabancaya samples are characterised by high contents of large-ion lithophile elements (LILE; *e.g.*, K, Rb, Ba, Th), low concentrations of high field strength elements (HFSE; *e.g.*, Nb, Zr) and heavy rare earth elements (HREE; *e.g.*, Yb), with consequently high La/Yb and Sr/Y ratios. An increase in these ratios is usually interpreted as a result of magmatic differentiation in the presence of garnet in the deep crust. A detailed analysis reveals that the rocks of Ampato-Sabancaya display three different compositional groups. (1) The first, composed mainly of andesites (56.7–59.8 wt.% SiO_2), corresponds to lavas from the early stage of the Ampato Basal edifice, as well as pyroclastic deposits from the Ampato Upper edifice. (2) The second group corresponds to andesitic and dacitic compositions (60.0–67.3 wt.% SiO_2) from the Ampato Basal edifice (Moldepampa stage), the Ampato Upper edifice, and the Sabancaya edifice. (3) The third group corresponds to dacitic compositions (65.0–69.3 wt.% SiO_2) associated with the Corinta Plinian fallout and pyroclastic flow deposits from the Ampato Upper edifice. This last group of dacites, erupted during the Ampato Upper edifice stage, have drastically different compositions from the other groups with Sr/Y (<27) and Sm/Yb (<4.7) ratios lower than other lavas and lacking evidence of amphibole and/or garnet fractionation during their genesis. As a whole, Sr, Nd, Pd isotopic ratios suggest that mantle-derived magmas are significantly affected by assimilation processes during their evolution, due to the thick (65–70 km) continental crust beneath the CVZ in southern Peru. In summary, the magmatic evolution of group 1 and 2 can be explained by a two-step model in which primitive magmas evolved in the deep crust in the so-called melting-assimilation-storage-homogenization (MASH)-type reservoirs by assimilation-fractional crystallization

(AFC) processes involving garnet and/or amphibole. Then, amphibole-dominated upper crustal AFC processes and magma mixing are responsible for the geochemical diversity of the main ASCV trend. In contrats, the group 3 dacites followed an upper crustal AFC process (without amphibole) from a different primitive magma, which did not suffer the high pressure, garnet-dominated AFC processes. This evolution highlights the complexities associated to magma genesis and differentiation at continental arcs contructed on a thick crust.

***Keywords**: Ampato, Sabancaya, Central Andes, Arc magmatism, Magmatic evolution, Geochemistry, Assimilation-fractional crystallization, Magma mixing.*

1. Introduction

The volcanic arc along the Andean Cordillera results from the subduction of the oceanic Nazca plate below the continental South American plate. This volcanic arc is divided into three active arc segments, the Northern (NVZ), Central (CVZ), and Southern (SVZ) volcanic zones (Fig. 1a). In addition, the Austral volcanic zone (AVZ) results from subduction of the Antartica plate below the South American plate. The CVZ is composed of volcanoes in southern Peru, Bolivia, and northern Chile and Argentina. This arc segment is constructed on one of world's thickest continental crusts and is considered the archetype for studying crustally-modified arc magmas (Barreiro and Clark, 1984; Harmon et al., 1984; Thorpe et al., 1984; Davidson et al., 1991; Mamani et al., 2010).

Quaternary lavas in the CVZ are high-K andesites, dacites and rhyolites that systematically display low heavy rare earth elements (HREE) and Y contents. In addition, these magmas are characterised by high $^{87}Sr/^{86}Sr$ and $\delta^{18}O$ ratios (typically >0.70534 and 8–12‰, respectively), low εNd (-2–12), and relatively low $^{206}Pb/^{204}Pb$ ratios (17.3–19.0)

(Barreiro and Clark, 1984; James, 1982; Wörner et al., 1988; Davidson et al., 1991; Haschke et al., 2006; Delacour et al., 2007; Kay et al., 2010; Mamani et al., 2010; Rivera et al., 2017). Petrogenetic models for the CVZ consider that the primitive calc-alkaline magmas are derived from partial melting of a mantle wedge previously metasomatised by hydrous fluids released through dehydration of the subducted lithosphere. These mantle-derived magmas evolved by fractional crystallization coupled with crustal assimilation or partial melting during magma storage and ascent through the thick continental crust.

Given that the CVZ magmas have systematically high La/Yb, Sm/Yb and Sr/Y ratios, some researchers support the idea that evolution of these magmas is dominated by crustal partial melting with garnet present in the residue (Kay, 2002; Mamani et al., 2010). While other authors (e.g., Hildreth and Moorbath, 1988; Davidson et al., 1991; Freymuth et al., 2015) consider that both mantle-derived and crust-derived magmas may have mixed and/or mingled at deep levels in the high-pressure melting, assimilation, storage and homogenization (MASH) zones, thereby producing large volumes of contaminated andesitic magmas. This model has been corroborated through recent seismic imaging studies that show low seismic velocity zones throughout the crust which are interpreted as the upper part of trans-crustal MASH zones (Delph et al., 2017). As a complement of the MASH model, several studies highlight the role of low pressure AFC processes as an explanation of the compositional diversity of magmas erupted at the large compound CVZ volcanoes (e.g., James, 1982; Barreiro and Clark, 1984; Harmon et al., 1984; Thorpe et al., 1984; Vatin-Pérignon et al., 1992; Feeley and Sharp, 1995; Godoy et al., 2014; Rivera et al., 2017). Recently, Blum-Oeste and Wörner (2016) proposed a slightly different model in which magma mixing (instead of the AFC process) is the dominant process, and identified three geochemical end-members for the CVZ magmas: (1) a slightly evolved calc-alkaline, mantle-derived basaltic andesite; (2) an enriched, mantle-

derived, shoshonitic basalt; and, (3) a crust-derived rhyodacite. Following these authors, the variable proportions of these three end-members could explain the compositional variability of CVZ magmas.

In order to provide constraints on the crustal contribution of the CVZ magmas, we focus on the petrogenetic evolution of a single volcanic centre of this arc segment, the Ampato-Sabancaya compound volcano (ASCV), a large, late Pleistocene volcanic centre of the Peruvian CVZ. Previous studies on this volcanic centre focused on reconstructing the eruptive chronology and identifing a large magmatic diversity of silica-rich end-members (dacites and rhyolites) that could represent different modalities of the crustal processes (Samaniego et al., 2016; Rivera et al., 2016). Based on a detailed reconstruction of the Ampato-Sabancaya eruptive chronology, we present major and trace element compositions, and Sr, Nd, and Pb isotope data for samples covering the entire Ampato-Sabancaya lifetime. These data record the compositional variations through the evolution of the Ampato-Sabancaya compound volcano and enable us to identify the main petrogenetical processes that control the composition of the erupted magmas. These hypotheses have been tested using different geochemical modelling approaches in order to describe the evolution of magma genesis at ASCV during the last 0.5 My.

2. Regional geological setting

In southern Peru, the CVZ arc segment results from subduction of the 40–45 Ma oceanic Nazca plate beneath the South American continental plate at a convergence direction of N80º and rate of 5–7 mm/yr (Norabuena et al., 1998). The resulting volcanic arc developed along the Western Cordillera and is constructed on continental crust reaching ~65-70 km thick along the main Andean keel (Beck et al., 1996). Geological mapping of the Western Cordillera indicates that the oldest rocks correspond to granulite-

facies gneisses (such as the Charcani gneiss portion of the Arequipa Massif, Boily et al., 1989) that crop out 32 km northwest (in Colca Canyon) and 34 km southwest of Ampato-Sabancaya volcano. The Arequipa Massif includes rocks with protolith ages of 1.9 Ga (Dalmayrac et al., 1977) and others with Mesoproterozoic protoliths and metamorphism ages of 1.2–1.0 Ga (Wasteneys et al., 1995; Loewy et al., 2004). These rocks arguably occur at depth beneath the volcanic arc of southern Peru (Harmon et al., 1981). This older massif is unconformably overlain by weakly folded, Mesozoic marine clastic (Yura Group) and volcano-sedimentary formations that have been intruded by Paleogene granites and granodiorites belonging to the Coastal Batholith (Tiabaya super-unit; Caldas, 1973; Romero and Ticona, 2003). These formations are covered by Oligocene-Miocene volcaniclastic and volcanic sequences (Tacaza Group) that in turn are overlain by Pliocene-Pleistocene volcanic sequences (Barroso Group). Late Quaternary volcanoes, such as Ampato-Sabancaya, are constructed on top of a high-altitude plateau formed by the older Barroso and Tacaza volcanic sequences.

The Quaternary volcanic arc in southern Peru is composed of at least 14 andesitic and dacitic compound volcanoes and several monogenetic volcanic fields (de Silva and Francis, 1991; Siebert et al., 2010; Bromley et al., 2019) (Fig. 1a, b). During historical time (*i.e.,* following the Spanish conquest beginning in 1532 CE), six of these volcanoes have experienced eruptive activity: Sabancaya, El Misti, Ubinas, Huaynaputina, Ticsani, and Tutupaca (Thouret et al., 2005; Thouret et al., 2001; Siebert et al., 2010; Samaniego et al., 2015). Some of these volcanoes experienced large explosive eruptions during the last few millenia and historical times, including the Plinian eruptions of El Misti (*c.* 2030 yr BP, Thouret et al., 2001; Harpel et al., 2011), Ubinas (*c.* 1000 yr BP, Thouret et al., 2005; Samaniego et al., 2020), and Huaynaputina (1600 CE, Prival et al., 2020), as well as the collapse-triggered explosive eruption of Tutupaca (1787–1802 CE, Samaniego et

al., 2015). In addition, Ubinas and Sabancaya are among the most active Central Andean volcanoes, with several small-to-moderate magnitude eruptions during the last centuries. The most recent such eruptions occurred during 2006–2009 CE, 2013–2017 CE and 2019 CE at Ubinas; and 1986–1998 CE and since 2016 CE at Sabancaya.

3. Ampato-Sabancaya volcanological evolution

The Ampato-Sabancaya compound volcano (ASCV, 15° 49.3'S, 71° 52.7'W) is located 75 km northwest of the city of Arequipa (Fig. 1), in the Western Cordillera of the Andean Central Volcanic Zone (CVZ, Fig. 1a). This compound volcano is situated southeast of the older, Pleistocene, Hualca Hualca edifice (6,025 m above sea level – a.s.l.). Ampato (6,280 m asl) and Sabancaya (5,980 m asl) form a massif, aligned along a N50° trend, decreasing in age from SW to NE. An andesitic lava flow emplaced over Pliocene ignimbrites forms the basement of the ASCV and has an age of 0.80 ± 0.04 Ma (Gerbe and Thouret, 2004), constraining the initiation of growth for Ampato and Sabancaya volcanoes to have been during the middle or upper Pleistocene.

Ampato volcano covers an area of 90–100 km^2 with an approximate volume of 38–42 km^3 (Samaniego et al., 2016). The volcano's current morphology is formed by at least three successive cones orientated SW-NE, hereafter termed the Southern, Central, and Northern cones, respectively located 1.2 and 2.5 km from the summit (the Southern cone) (Fig. 2). Ampato was affected by glacial erosion during the Last Glacial Maximum (LGM) which roughly occurred in this part of the Andes between 17 and 25 ka (Bromley et al., 2009). On Hualca Hualca volcano, cosmogenic exposure ages on blocks from LGM moraines indicate that this event occurred between 16 and 17 ka (Alcalá-Reygosa et al., 2017). This glacial event generated a variety of morphological features such as cirques

and U-shaped valleys on the western and southeastern flanks of Ampato. Following Rivera et al. (2016) and Samaniego et al. (2016), the eruptive chronology of Ampato compound volcano comprises:

(1) The Ampato Basal edifice (Fig. 2), which is an old, highly eroded volcano composed of a 600-m-thick succession of lava flows interlayered with scarce scoria-flow deposits (57.2–62.2 wt.% SiO_2) and spatter agglutinates that crop out on the proximal southwestern and western flanks of Ampato (AMI-1, Fig. 2). We include in this older stage, a 200–400 m-thick medial-to-distal succession of sub-horizontal andesitic lava flows (57.2–61.9 wt.% SiO_2) that crop out on the Jatun Pampa plain, on the southeast side of Ampato (AMI-2, Fig. 2). This, the oldest stage of the Ampato Basal edifice, was constructed between 450 ka and 400 ka (Samaniego et al., 2016). Another remnant of this edifice (Moldepampa stage, AMI-3, Fig. 2) consists of a 200–300 m-thick succession of dacitic lava flows (62.9–65.1 wt.% SiO_2). Age determinations by Samaniego et al. (2016) on lavas of this stage yield dates of about 230–200 ka. Samaniego et al. (2016) and Rivera et al. (2016) assumed that a 4–5 m-thick succession of rhyolitic tephra-fall deposits (74.2–76.9 wt.% SiO_2), which only crop out in the Chacramayo valley 10 km southwest of Ampato, were emplaced at the end of this stage. In this work, we challenge the origin of these rhyolitic deposits.

(2) The Ampato Upper edifice started with the Yanajaja stage (AMII-1, Fig. 2), which consists of a sucession of andesitic and dacitic lava flows (61.8–63.5 wt.% SiO_2) reaching 200–300 m thick that outcrop on the south and southwest flanks of Ampato. A sample from this unit was dated at 77 ± 4 ka. The successive construction of the Northern (AMII-2), Southern (AMII-3, 4, 6, 7), and Central (AMII-8) peaks is represented by lava flows and pyroclastic sequences with andesitic compositions (61.0–62.0 wt.% SiO_2). Two lavas of the south and southeast flanks of the Upper edifice yielded ages of 40 ± 3 and 34 ± 8

ka, respectively. Associated with this volcanic stage are the thick (>20 m) block-and-ash flow deposits that crop out 5–6 km east and west of the Ampato summit (AMII-5, Fig. 2). In addition, we include in this stage the scoria-rich Baylillas (56.7–59.0 wt.% SiO_2) and Corinta (65.0–68.0 wt.% SiO_2) tephra-fall and pyroclastic-density current deposits which crop out 10–12 km southwest of the volcano's summit. These pyroclastic successions are highly eroded and were likely emplaced before the LGM (i.e., 17–25 ka; Bromley et al., 2009; Alcalá-Reygoza et al., 2017). The central cone was discordantly constructed over the remnants of the northern and southern cones of the Ampato Upper edifice (Fig. 2). It is composed of a sequence of andesitic and dacitic (61.3–66.0 wt.% SiO_2) lava flows, with a maximum thickness of 400–600 m. A lava sample from this unit was dated at 17 ± 6 ka (Samaniego et al., 2016). An oblate, andesitic (61.3 wt.% SiO_2) lava dome lacking evidence for glacial erosion is located at the top of the northern cone between 5,700 m asl and 6,000 m asl and is Ampato volcano's youngest feature.

Sabancaya volcano covers an area of 65–70 km^2 and comprises a volume of approximatly 6–10 km^3 (Samaniego et al., 2016). Sabancaya is located northeast of the older Ampato edifice and has two coalescing cones orientated in a SW-NE direction. Sabancaya's eruptive chronology started with the older Basal edifice, which is represented by a sequence of blocky, andesitic-dacitic (60.6–65.6 wt.% SiO_2) lava flows (SA-1) that spilled out onto the older rocks of the Ampato and Hualca Hualca edifices. These blocky lava flows have individual thicknesses of 40–80 m, forming a 300–400 m thick lava pile that extends as far as 8 km from the west to southeast of the summit (Fig. 2). A lava flow from this stage was dated at 6.30 ± 0.31 ka by ^{3}He surface-exposure dating (Samaniego et al., 2016). We include in this stage the 400 m-high lava dome that forms the southwestern part of Sabancaya's current summit (SA-2); as well as three andesitic (60.9–

62.5 wt.% SiO_2) lava flow successions (SA-3) emplaced on the Sallalli plain (Fig. 2). Bulmer et al. (1999) and Samaniego et al. (2016) linked this sequence to a satellite vent located 4 km to the southwest of the active crater. Two samples from these blocky lava flows were dated by Samaniego et al. (2016) at 6.65 ± 0.32 ka and 12.34 ± 0.55 ka by ^{3}He surface-exposure dating (Fig. 2). More recently, Bromley et al. (2019) measured helium concentrations in two additional samples from Sabancaya lavas, obtaining ages of 5.2 ± 0.1 ka and 4.1 ± 0.1 ka (Fig. 2). In addition, a lava flow emplaced on the western flank of the volcano covering a peat bog yielded an age of 5,440 ± 40 ^{14}C yr BP (Gerbe and Thouret, 2004). Based on such geochronological information, Sabancaya's Basal edifice was constructed during the Holocene.

Sabancaya's eruptive chronology continued during the Late Holocene with the construction of a younger cone represented by a sequence of lava flows (SA-4) emplaced discordantly upon the lavas of the previous stage. These lava flows reach 4–5 km from the vent, have a thickness of 40–60 m and consist of andesites and dacites (61.7–65.7 wt.% SiO_2). This cone is covered by pyroclastic material and includes an active, semi-circular summit crater (Fig. 2) and a maximum diameter of 290 m. Explosive activity of Sabancaya continued until historic times. Two well-preserved ash-rich tephra-fall deposits in the Sallalli peat bog southeast of Sabancaya were emplaced between 4.5 ka and 3 ka (Samaniego et al., 2016). In the Quebrada Huaraya section, a 10–30 cm-thick coarse ash layer was found, where the underlying peat yielded an age of 265 ± 30 ^{14}C yr BP. This age agrees with the 300 ± 50 ^{14}C yr BP date obtained by Juvigné et al. (2008) and confirms the occurrence of explosive eruptions during the 17th or 18th century (Travada and Córdova, 1752).

During the 20th century, eruptive activity resummed at Sabancaya, lasting from 1986 until 1998. In December 1986, Sabancaya experienced enhanced fumarolic activity

followed by an increase of explosive activity that culminated with an eruption (VEI 2) on 29 May 1990 (Gerbe and Thouret, 2004). Explosions generated columns of ash and gas that rose 1–5 km above the crater during which ash was dispersed as far as 12 km from the summit. Then, recurrent at low to moderate explosive activity continued until 1998. The bulk volume of the tephra emitted during the major phase of the eruption from May to October 1990 was roughly estimated as 0.025 km^3 (Thouret et al., 1994). In 2013, Sabancaya experienced a significant increase in seismic activity and gas emissions that eventually rose to 2,000 m above the summit. Subsequently, in November 2016, a new eruptive period began and is ongoing through the time of writing (May 2023). This eruptive activity is characterised by vulcanian explosions associated with frequent gas and ash emissions which in July 2017 formed eruption columns reaching up to 5,000 m above the summit. Associated with the 2016–2020 eruptive activity, we observe newly emplaced lava domes inside the summit crater.

4. Sample collection and preparation, and analytical methods

4.1. Field sampling and sample preparation

Geological mapping, stratigraphic studies and sampling were conducted during several field campaigns between 2009 and 2020. We collected 138 samples that are representative of most volcanic units (Fig. 2).

4.2 Analytical methods

4.2.1. Mineral analyses

Thin sections of all samples were prepared for petrographic studies and electron microprobe analysis. The mineral analyses for 26 samples were obtained using a CAMECA SX-100 electron microprobe at the Laboratoire Magmas et Volcans

(Université Clermont Auvergne, Clermont-Ferrand, France). Operating conditions for mineral analyses were 15 keV accelerating voltage, 10 nA beam current and 10 s counting time. The estimated error for a single analysis is about 1% when the element concentration is higher than 10%, whereas for element concentrations lower than 10% uncertainty is 2–5%. Composition data for phenocrysts from each volcanic unit are presented in Supplementary Electronic Material (SEM 1).

4.2.2. Major and trace element whole-rock analyses

Major and trace element concentrations in 132 whole-rock samples were determined at the Laboratoire Geosciences Océan, Université de Bretagne Occidentale (Brest, France). Agate-ground powders were dissolved in HNO_3 and HF and then measured by ICP-AES (Inductively Coupled Plasma-Atomic Emission Spectroscopy), following the procedure of Cotten et al. (1995). Relative standard deviations are 1% for SiO_2 and <2% for the other major element oxides, except for low concentrations (<0.50%), for which the absolute standard deviation is 0.01%. For trace elements, the relative standard deviation is *ca.* 5%. Calibrations were performed using international standards JB2, BEN, ACE, WS-E, PM-S as well as specific reference samples. All analyses were recalculated on an anhydrous basis with iron expressed as Fe_2O_3*. We add to the database 6 major and trace element analyses from the 1990 eruptive products published by Gerbe and Thouret (2004). Representative whole-rock analyses are presented in Table 1, while all whole-rock analyses are presented in SEM 2.

4.2.3. Sr, Nd, and Pb whole-rock analyses

Sr and Nd isotope analyses of 37 samples from Ampato and Sabancaya lavas were performed at the Laboratoire Magmas et Volcans (Clermont-Ferrand, France) on whole-

rock powders, which were dissolved using an $HF/HNO_3/HClO_4$ mixture. Sr and Nd were separated by ion-exchange chromatography according to the procedures described in Pin et al. (1994) and Pin and Santos-Zalduegui (1997). $^{87}Sr/^{86}Sr$ and $^{143}Nd/^{144}Nd$ isotopic ratios were determined using either a VG Isomass 54E multicollector mass spectrometer or a Finnigan TRITON. During the period of measurements, SRM-987 and AMES Rennes standards gave $^{87}Sr/^{86}Sr=0.710239 \pm 0.00002$ (2σ, n=4) and $^{143}Nd/^{144}Nd=0.5119651 \pm 0.000015$ (2σ, n=4). Six additional Sr/Nd isotopic ratios published by Gerbe and Thouret (2004) and three published by Mamani et al. (2010) are also included. Pb isotopic ratios were measured by MC-ICP-MS (Multicollector Inductively Coupled Plasma Mass Spectrometer) at Laboratoire Magmas et Volcans (Clermont-Ferrand, France) following the procedure described by Nauret et al. (2018). Pb isotope ratios are normalized to values of the NIST SRM 981 standard provided in Galer and Abouchami (1998). Selected whole-rock major and trace elements, and Sr, Nd, and Pb isotopic ratios are presented in Table 1 and all the data are in SEM 2.

5. Characterisation of Ampato-Sabancaya volcanic rocks

5.1. Petrography and mineral chemistry

Textures and mineral assemblages are similar throughout the ASCV rocks. The lava and pyroclastic deposits of ASCV are often porphyritic with intersertal and/or vitreous groundmass (Fig. 3). Ampato eruptive products are dominated by andesitic (~50%) and dacitic compositions (~46%), although some scarce (~4%) rhyolitic samples were also reported (Table 2). The lavas contain up to 30 vol.% phenocrysts, which are generally 0.2–3.0 mm and rarely up to 6.0 mm, and are variably vesicular (2–8 vol.%). Less than 8% of the lavas are subaphyric to poorly porphyritic, especially the lavas of the Ampato Basal edifice. The pyroclastic products contain between 10–30 vol.%

phenocrysts, which are generally 0.2–2.2 mm and rarely up to 4.0 mm, and are variably vesicular (10–60 vol.%). Ampato andesites have a phenocryst assemblage of plagioclase (Pl), clinopyroxene (Cpx), amphibole (Amp), biotite (Bt), and magnetite (Mag) together with scarce orthopyroxene (Opx), and olivine (Ol). The Ampato dacites host phenocrysts of Pl + Cpx + Bt + Amp + Mag and scarce Opx. The fine-grained groundmass of these rocks consists of Pl + Cpx + Amp + Mag, and scarce colourless to brownish interstitial glass. The rhyolites contain Pl + Bt + Mag and scarce alkali feldspar (Kfs) and quartz (Qz).

Some dense juvenile blocks belonging to block-and-ash flow deposits from the Ampato Upper edifice have dark brown and light gray bands. The dark brown bands contain phenocrysts of plagioclase (20–25 vol.%), amphibole (5–10 vol.%), clinopyroxene (2–4 vol.%), and biotite (2–4 vol.%), included within a vesicular matrix. In contrast, the light gray bands contain less phenocrysts than the dark brown bands and have an assemblage of plagioclase (2–4 vol.%), biotite (2–4 vol.%), and clinopyroxene (1-2 vol.%) within a glassy matrix.

Sabancaya's eruptive products are andesitic (~62%) and dacitic (~38%) in composition (Table 2). The lavas contain up to 30 vol.% phenocrysts, which are generally 0.2–4.0 mm and rarely up to 7.0 mm. Samples are variably vesicular, with <8 vol.% for lavas and 4–10 vol.% for pyroclastic products. All andesites and dacites (e.g., SA-1, SA-2, SA-3) have an assemblage of Pl, Amp, Bt, Cpx, and Mag together with scarce Opx, and Ol. While such mineral phases are ubiquitous, their relative proportions are variable. The fine-grained groundmass (<80 μm) consists of Pl, Amp, Cpx, Mag, and scarce colourless, grey, or brownish interstitial glass.

The eruptive products emitted during the 1990–1998 eruption are andesites and dacites (60-64 wt.% SiO_2). According to Gerbe and Thouret (2004), all eruptive products

are porphyritic with 20-25 vol.% phenocrysts. Some dense juvenile blocks have dark brown and light grey bands. The mineral assemblage consists of plagioclase (0.2–4 mm), amphibole (>0.2 mm), clinopyroxene, biotite, and Fe-Ti oxides. Eruptive products emitted during the 2017 CE eruptions are homogeneous, porphyritic andesites (60-61 wt.% SiO_2), with 40-50 vol.% phenocrysts. These andesites have a mineral assemblage consisting of plagioclase (20–25 vol.%), amphibole (4–6 vol.%), clinopyroxene (4–6 vol.%),), orthopiroxene (<1-2 vol. %), biotite (<1-2 vol. %) and Fe-Ti oxides.

5.1.1. Plagioclase

Plagioclase is the most abundant phenocryst phase in Ampato-Sabancaya rocks and occurs as euhedral to subhedral phenocrysts (20-40 vol.%) as well as microlites (SEM 1). Based on textural and chemical characteristics, we identify two different plagioclase populations: (1) euhedral, non-altered phenocrysts with normal, oscillatory and/or reverse zoning patterns; and (2) sieve-cored or sieve-ringed phenocrysts with frequent dissolution zones and overgrowth rims displaying strong reverse zoning. In samples from Ampato Basal edifice, the anorthite content in plagioclase ranges from labradorite to oligoclase (An_{24-72}, Table 3, SEM 3). In Ampato Upper andesites the plagioclase is bytownite, labradorite, andesine, and oligoclase (An_{28-75}), while in Ampato Upper dacites (including those of the Corinta unit) the plagioclase is labradorite, andesine, and oligoclase (An_{28-57}). In both eruptive stages, normal zoning is frequent while reverse zoning is scarce. In Sabancaya andesites and dacites the anorthite content of plagioclase includes labradorite, andesine, and oligoclase (An_{27-63}). Normal zoning is frequent in some phenocrysts while reverse zoning is scarce. In the products of the 1990 activity, the composition varies from oligoclase to labradorite (An_{26-62}), of which andesine is predominant (Gerbe and Thouret, 2004). The andesites contain a mixed population of plagioclase

phenocrysts: Ca-rich clear plagioclase (An_{40-60}), Na-rich clear plagioclase (An_{25-35}), and inversely zoned "dusty rimmed" plagioclase with a sodic core (An_{25-40}) surrounded by a Ca-rich overgrowth rim (An_{45-65}) (Gerbe and Thouret, 2004). In the juvenile blocks of the 2017 CE eruptions the composition varies from andesine to labradorite (An_{36-55}).

5.1.2. Clinopyroxene

Clinopyroxene occurs as euhedral to subhedral phenocrysts (<8 vol.%; up to 1 mm in size) as well as microlites in the andesites and dacites (Table 2). In Ampato andesites and dacites (from both Basal and Upper edifices) clinopyroxenes have a restricted compositional range from diopside to magnesian augite (En_{39-46}-Fs_{12-19}-Wo_{40-47}, following Morimoto et al. 1988) with Mg# [where Mg# = 100*Mg/(Mg + Fe^T) in mol.%, and Fe^T is total iron as Fe^{2+}] from 74–84 (Table 3, SEM 1, SEM 4). They generally are normally zoned (e.g., SA-1102: Mg# 80-76), but rare reverse zoning also exists (e.g., SA-1137: Mg# 72-76). In Sabancaya andesites and dacites, clinopyroxenes also have a homogeneous compositional range from diopside to magnesian augite (En_{38-48}-Fs_{11-17}-Wo_{40-46}) with Mg# 72-85 (SEM 1 and SEM 4). They generally have normal (e.g., SA-0907: Mg#79-76) and reverse zoning patterns (e.g., SA-1152: Mg#73-79). The rocks of the 1990-1998 eruption contain clinopyroxenes, essentially augites (En_{40-46}-Fs_{15-16}-Wo_{40-46}), similar to the rocks from the 2017 CE eruption (En_{41-43}-Fs_{15-16}-Wo_{40-43}) with Mg# ranging from 77 to 79. Additionally, some Sabancaya and Ampato Upper edifice (AMII-3) clinopyroxene are Mg- and Cr-rich (Mg# 72-78, up to 0.1 wt % Cr_2O_3) (SEM 4). These high Mg# and Cr_2O_3 contents suggest that these minerals crystallized from more primitive magmas.

401 *5.1.3. Orthopyroxene*

402 Euhedral and subhedral orthopyroxene are present as phenocrysts and microlites
403 (<8 vol. %; up to 1 mm in size) in most andesites and some dacites (Table 3). In Ampato
404 andesites and dacites, orthopyroxene has a compositional range from $En_{62–76}$ (Table 3,
405 SEM 1 and SEM 4). While in andesites from Sabancaya they have a compositional range
406 from $En_{41–76}$. The orthopyroxene of the Ampato andesites are sligtly less magnesian
407 compared to Sabancaya orthopyroxene. In Ampato and Sabancaya rocks, orthopyroxene
408 has slight normal zoning patterns (e.g., Ampato andesite SA-1033C: Mg# 75–72;
409 Sabancaya andesite SA-0907: Mg# 78–76) and scarce reverse zoning (e.g., Ampato dacite
410 SA-0930: Mg# 72–78; Sabancaya andesite SA-0906: Mg# 66–78). The orthopyroxene
411 from the 2017 CE eruptions have homogeneous compositions (En_{71-72}). Orthopyroxene is
412 absent in the rhyolites.

413

414 *5.1.4. Amphibole*

415 Amphibole phenocrysts are present in different modal proportions (up to 10
416 vol.%; up to 4 mm in size) in andesite and dacite lavas and pyroclastic products from
417 Ampato and Sabancaya (Table 3). They are an accessory phase (~1 vol.%) in some
418 Ampato Basal andesites, with subhedral forms and frequent, thin opaque (black) reaction
419 rims. In contrast, amphibole phenocrysts in the Ampato Upper and Sabancaya andesites
420 and dacites are much more abundant (2–10 vol.%), are euhedral and subhedral, and
421 display scarse disequilibrium features. Indeed, thin opaque (black) reaction rims are
422 sometimes observed, and very scarsely some amphiboles are completly replaced
423 (pseudomorphs) by Fe-Ti oxides and pyroxene aggregates (e.g., SA-0918, 0911).
424 Amphibole phenocrysts in Ampato Basal rocks have magnesio-hastingsite compositions
425 while those of Ampato Upper and Sabancaya are edenite, magnesio-hastingsite,

426 magnesio-hornblende, and tschermakite (SEM 3) (Leake et al., 1997). Values of Mg# for
427 amphibole in Ampato andesites and dacites vary from 70–83. There is minimal variation
428 of Mg# among the different eruptive stages of Ampato, although normal (e.g., andesite
429 SA-1155: Mg# 74-71) and reverse zoning are observed (e.g., dacite SA-1127C: Mg# 74-
430 78). The amphiboles in Sabancaya andesites and dacites have Mg# values that vary from
431 70–89, with mainly normal (e.g., andesite SA-0907: Mg# 85-79) and reverse zoning
432 patterns (e.g., dacite SA-1015: Mg# 71-73). The rocks from the 2017 CE eruptions
433 contain amphiboles with magnesium-hornblende and magnesium-hastingsite
434 compositions (Mg# 72-77).
435
436 *5.1.5. Biotite*
437 Biotite crystals occur in andesites, dacites, and rhyolites from Ampato and
438 Sabancaya (SEM 1). Biotite (up to 6 vol.%, up to 3 mm in size) has euhedral and subhedral
439 habits. Some phenocrysts have inclusions of plagioclase, clinopyroxene, and Fe-Ti oxide
440 microlites. In some lavas, biotite crystals are armored by opaque minerals and plagioclase
441 microlites (e.g., SA-0905; SA-0919). Ampato biotite is characterized by high proportions
442 of $Fe^{+2}/(Fe^{+2}+Mg)$ (0.34-0.61) while Sabancaya biotite have narrow $Fe^{+2}/(Fe^{+2}+Mg)$
443 values (0.40-0.44). All biotite crystals display high Al_2O_3 (11.4-29.5 wt.%) (Table 2,
444 SEM 1), and TiO_2 (3.8-5.9 wt.%) concentrations, whereas Mg# is relatively low (49-66).
445
446 *5.1.6. Olivine*
447 Olivine appears only as an accessory phase (<2 vol.%) in mafic andesites of
448 Ampato Basal stage (Table 2 and 3) and are mostly subhedral and anhedral phenocrysts
449 (<0.8 mm). The olivines have low magnesium content with forsterite (Fo) contents that
450 vary in the range $Fo_{68–77}$. The phenocrysts have subtle normal zoning (e.g., SA-1102:

Fo_{73-72}). In Sabancaya, olivine is scarce and appears in some andesitic lavas with slightly higher forsterite contents in the range $Fo_{80–82}$. In this group, weak normal zoning is observed (e.g., SA-0906: Fo_{80-82}).

5.1.7. Fe-Ti oxides

Fe-Ti oxides (with sizes >40 µm) are present in the groundmass or as inclusions within pyroxenes, biotite, amphibole, and some olivine phenocrysts. All studied samples contain titano-magnetite, while some high-silica andesites and dacites of Sabancaya and Ampato also containt scarce ilmenite (SEM 1).

5.1.8. Accessory minerals

Quartz appears as anhedral microphenocrysts in the most silica-rich samples (SiO_2 >70 wt.%) or as small grains in the groundmass of some dacites. Alkaline feldspars appear as phenocrysts of sanidine (Or_{70-71}, Table 3, SEM 3) in some rhyolites. Apatite is found as inclusions in almost all mineral phases (amphibole, biotite, pyroxenes, and plagioclase).

5.2. Main geochemical characteristics

5.2.1. Major and trace elements

All analysed samples plot in the high-K calc-alkaline field of Peccerillo and Taylor (1976) (Fig. 4). The rocks of Ampato have a wide compositional range between basic andesites to dacites (56.7–69.33 wt.% SiO_2; 2.0–4.9 wt.% K_2O) while those of Sabancaya range between andesites and dacites (60.0–65.7 wt.% SiO_2; 2.7–3.6 wt.% K_2O). In this analysis, we also include the rhyolitic deposits that crop out to the west of Ampato-Sabancaya. The eruptive products of the 1990-1998 activity are andesites and

dacites (60.6–63.8 wt.% SiO_2), while the eruptive products of the 2017 activity are mainly andesitic (58.2–61.2 wt.% SiO_2).

In general, the ASCV samples display a single magmatic trend, but a more detailed analysis reveals that four different groups are present. (1) the first group, composed mainly of andesites (56.7–59.8 wt.% SiO_2), corresponds to lavas from the early andesitic stage of the Ampato Basal edifice, as well as to the scoriaceous tephra-fall and pyroclastic-flow deposits of Ampato Upper edifice (Fig. 4). These samples are porphyritic lavas and tephras with plagioclase, ortho- and clinopyroxene, and Fe-Ti oxides. (2) The second group corresponds to andesitic and dacitic compositions (60.0–67.3 wt.% SiO_2) from the Moldepampa stage, Ampato Upper edifice, and Sabancaya edifice. All these samples are porphyritic with phenocrysts of plagioclase, amphibole, biotite, ortho- and clinopyroxene, and Fe-Ti oxides. (3) The third group corresponds to dacitic compositions (65.0–69.3 wt.% SiO_2) associated with the Corinta Plinian tephra-fall and pyroclastic-flow deposits of the Ampato Upper edifice (Fig. 4). (4) A final group consists of the rhyolites (74.2–76.9 wt.% SiO_2) that correspond to tephra-fall deposits ascribed by Samaniego et al. (2016) to the Ampato Basal edifice.

A compositional evolution over time is not apparent. When plotted in Harker diagrams (Fig. 4), the andesites and dacites do not align along a single trend, and are separated from the rhyolitic eruptive products by a compositional gap between 69 wt.% SiO_2 and 74 wt.% SiO_2. In binary diagrams (Fig. 4), all major oxides (except K_2O) are negatively correlated to SiO_2, whereas trace elements show positive correlations with silica, especially for the Large-Ion Lithophile Elements (LILE, e.g., Rb, Th, Ba). In these diagrams, compared to dacites of group 2, group 3 dacites have slightly elevated concentrations in some major and trace elements (e.g., K_2O, Al_2O_3, Rb, Zr, Sm, La, Yb), and lower concentrations for other elements (e.g., MgO, CaO, Sr, Ni, Cr). The Rare Earth

Elements (REE) have a noteworthy pattern because the Middle REE (MREE, e.g., Sm) and Heavy REE (HREE, e.g., Dy, Yb) are reversely correlated with silica. In contrast, High Field Strength Elements (HFSE, e.g., Nb) are positively correlated, while Light REE (LREE, e.g., La, Ce) have a subtle positive correlation. Additionally, Y, Zr, Sr, and the transition metals (e.g., Sc, V, Cr, Ni) are negatively correlated with silica. Lastly, the rhyolites plot along the trend defined by group 2, except for LREE (e.g., La, Ce), LILE (e.g., Th), and HFSE (e.g., Nb).

Multi-element diagrams normalised to primitive mantle (Sun and McDonough, 1989) suggest that Ampato-Sabancaya lavas are typical of continental arc magmas (Fig. 5). Compared to the primitive mantle, these samples are enriched (~100 times) in LILE (e.g., Ba, Rb, Th, K) and LREE (e.g., La, Ce). The HFSE (e.g., Nb and Zr) show a marked negative anomaly as well as P and Ti. The rhyolites have more prominent P and Ti anomalies than group 3 dacites, which are in turn more prominent than group 2 dacites.

The REE patterns normalised to chondrites (Sun and McDonough, 1989) for ASCV rocks are almost parallel and have large LREE enrichments ($77.5<La_N<247.5$) and HREE depletions ($4.7<Yb_N<10.8$). In contrast, group 4 rhyolites have univesally lower REE contents with respect to groups 1 and 2 rocks, while group 3 dacites have higher values of MREE and HREE compared to groups 1, 2, and 4. The REE patterns for most andesites and dacites are also characterized by a relatively weak Eu anomaly (Fig. 5). Indeed, a detailed analysis of the behavior of HREE and other trace elements shows that the rhyolite samples do not follow the same geochemical trend, precluding a single differentiation process linking Ampato-Sabancaya andesites and dacites with the rhyolites (even if we include allanite and/or monazite as accessory minerals in the cumulate).

526 *5.2.2. Isotopic ratios*

527 The $^{87}Sr/^{86}Sr$ ratios of the Ampato-Sabancaya andesite and dacite lavas range from
528 0.70633–0.70765, while the $^{143}Nd/^{144}Nd$ ratios range from 0.51229–0.51243 (Table 1,
529 Fig. 6). The $^{87}Sr/^{86}Sr$ ratios of the rhyolites range from 0.7072–0.7088, while the
530 $^{143}Nd/^{144}Nd$ ratios range from 0.51211–0.51230 (Fig. 6). Excluding these rhyolitic
531 compositions, the most radiogenic Sr values (and conversely the most unradiogenic Nd
532 values) are displayed by group 3 dacites from the Ampato Upper edifice (Fig. 6b).

533 In the $^{87}Sr/^{86}Sr$ *versus* $^{143}Nd/^{144}Nd$ diagram (Fig. 6a), the Ampato-Sabancaya
534 samples display a negative correlation and plot far from the mantle domain represented
535 by the MORB field. Sr and Nd isotopic data have broadly homogeneous values at the
536 scale of the CVZ (Davidson et al., 1991; Fig. 6a). Such characteristics suggest that ASCV
537 magmas are contaminated by the continental crust, an interpretation corroborated by a
538 positive correlation observed in the $^{87}Sr/^{86}Sr$ *versus* SiO_2 diagram (Fig. 6b). This
539 relationship between SiO_2 content (or any other differentiation index) and the isotopic
540 composition of Ampato-Sabancaya magmas provides strong evidence for contamination
541 by continental crust, possibly through an AFC process or magma mixing involving a
542 crustally-derived end-member.

543 The $^{206}Pb/^{204}Pb$ ratios of the andesites and dacites eruptive products range from
544 18.172 to 18.489, the $^{207}Pb/^{204}Pb$ ratios range from 15.612 to 15.625, and the $^{208}Pb/^{204}Pb$
545 ratios are from 38.546 to 38.715 (Table 1). In contrats, the rhyolites display very
546 heterogeneous lead isotopic values ($^{206}Pb/^{204}Pb$: 17.817–18.214; $^{207}Pb/^{204}Pb$: 15.599–
547 15.614; $^{208}Pb/^{204}Pb$: 38.469–38.715). We stress that least differentiated sample (SA-
548 1033E, Fig. 7) display the highest Pb istopic ratios. The Ampato-Sabancaya samples plot
549 in the typical fields for the Andean Central Volcanic Zone field (Mamani et al., 2010),
550 southern part of Arequipa segment, and northern part of the Toquepala segment of the Peruvian

551 Coastal batholith (Mukasa, 1986) (Figs. 7a, b). In some diagrams (Fig. 7), the samples show
552 a well-defined negative correlation pointing towards the Charcani gneiss field from the
553 Arequipa Massif (Figs. 7c, d). Similar to the Sr isotope data, group 3 and group 2 dacites
554 have homogeneous Pb isotope compositions, with lower $^{206}Pb/^{204}Pb$ for a given
555 $^{207}Pb/^{204}Pb$ and $^{208}Pb/^{204}Pb$ value compared to andesites. A low $^{206}Pb/^{204}Pb$ reflects the
556 influence of Precambrian-age crust such as the Arequipa massif of southern Peru
557 (Barreiro and Clark, 1984; James, 1982; Mamani et al., 2010).

558 The lead isotopic data (Figs. 7c, d) shows that most samples plot in a roughly
559 linear distribution. However, dacites from group 3 and some samples of Ampato Upper
560 edifice (group 2) have systematically low $^{206}Pb/^{204}Pb$ and high $^{207}Pb/^{204}Pb$ and $^{208}Pb/^{204}Pb$
561 values. This distribution cannot be explained by a single assimilation-fractional
562 crystallization or binary mixing process, suggesting that at least three end-members must
563 be involved. We consider this hypothesis in the following sections and propose a model
564 that accounts for magma mixing, fractional crystallization, and different crustal
565 contaminants.

566

567 *5.2.3. Temporal change in magma composition*

568 Figure 8 plots selected major and trace element compositions and ratios, as well
569 as isotopic ratios against stratigraphic position of the erupted products established
570 according to geological and geochronological information (Rivera et al., 2016;
571 Samaniego et al., 2016). During the growth of Ampato Basal edifice, andesitic and dacitic
572 (57–65 wt.% SiO_2) magmas were emitted. Later, during construction of the Ampato
573 Upper edifice, volcanic products with a wide geochemical variability from andesites to
574 dacites (57–69 wt.% SiO_2) were erupted. In addition, the groups 2 and 3 dacites were
575 emitted at roughly the same time (i.e. Ampato Upper edifice). During Sabancaya´s

576 evolution, the SiO_2 content varies slightly between andesites and dacites (60–66 wt.%
577 SiO_2), but is relatively constant and similar to that of group 2 andesites and dacites of
578 Ampato Upper edifice. In recent times, the geochemical composition of erupted magmas
579 is roughly andesitic (57–63 wt.% SiO_2). Trace element ratios (e.g., Sr/Y) as well as
580 $^{87}Sr/^{86}Sr$, $^{206}Pb/^{204}Pb$, $^{207}Pb/^{204}Pb$ and $^{208}Pb/^{204}Pb$ ratios (Fig. 8) also have a wide
581 compositional variation throughout the Ampato Basal edifice and predominantly
582 homogeneous compositions throughout Sabancaya. It is worth noting that group 3 dacites
583 have low Sr/Y values, but high $^{87}Sr/^{86}Sr$ ratios, a pattern that contrasts with group 2
584 dacites (high Sr/Y and high $^{87}Sr/^{86}Sr$ ratios). Through its evolution, most differentiated
585 products (mostly dacites) were erupted between 40 ka and 20 ka, however, the
586 geochemical and isotopic signatures of these dacites (groups 2 and 3) suggest that the
587 crustal process responsible for their petrogenesis are not the same. Lastly, we would stress
588 that rhyolites display wide Pb isotopes values (*cf.* $^{208}Pb/^{204}Pb$), therefore based on this
589 data and their trace elements behaviour (see above), we conclude that rhyolites (group 4)
590 do not belong to the Ampato-Sabancaya magmatic series.
591
592 **6. Discussion**
593 **6.1. The sources of Ampato-Sabancaya magmas**
594 Previous studies suggest that the primitive magmas for volcanoes in Southern Peru
595 essentially result from partial melting of mantle peridotite that was previously
596 metasomatised by fluids released during dehydration of the subducting slab (Thorpe et
597 al., 1984; Vatin-Pérignon et al., 1992; Thouret et al., 2005; Delacour et al., 2007; Mamani
598 et al., 2010; Rivera et al., 2017; Huang et al., 2017; Samaniego et al., 2020). In the case
599 of the ASCV magmas, their chemical and isotopic signatures point out to intermediate to
600 differentiated compositions, precluding a purely mantle origin.

The source and evolution of magmas feeding the composite CVZ volcanoes has been extensively investigated wether on a regional (James, 1982; Barreiro and Clark, 1984; Hildreth and Moorbath, 1988; Davidson et al., 1991; Mamani et al., 2010; Blum-Oeste and Worner, 2016; Burns and de Silva, 2023) or single edifice scales (Davidson et al., 1990; Feeley and Sharp, 1995; Delacour et al., 2007; Sorensen and Holm, 2008; Thouret et al., 2005; Rivera et al., 2017; Samaniego et al., 2020). Because shallow differentiation processes affected magma composition, its mantle source is difficult to assess. For this reason, geochemists are interested for the scarce primitive compositions erupted in this arc segment. The Andahua-Huambo eruptive products display similar petrographic and geochemical characteristics than those of the other composite volcanoes, however they also display some key differences, namely the presence of olivine-rich, basaltic andesitic compositions ranking among the most primitive lavas erupted at the CVZ (Delacour et al., 2007). Among these characteristics, we can mention low silica contents (as low as 52 wt.% SiO_2), relatively high MgO and Mg# values (2.02–7.33 wt.% MgO; Mg# 39.31–61.55), and unradiogenic isotopic ratios (0.7059–0.7069 $^{87}Sr/^{86}Sr$; 0.5123–05125 $^{143}Nd/^{144}Nd$; 18.298–18.629 $^{206}Pb/^{204}Pb$; 15.558–15.601 $^{207}Pb/^{204}Pb$; 35.546–38.643 $^{208}Pb/^{204}Pb$). Thus, the Andahua-Huambo lavas represent a base-line magma composition in Southern Peru and provide a window to unravel the deep crustal processes active at the CVZ.

Petrological characteristics of the Andahua-Huambo magmas suggest that they evolved at deep reservoirs, being slightly modified at shallow levels in the crust. Indeed, the low HREE and Y contents, and high La/Yb and Sr/Y ratios, and the Sr, Nd-, Pb-, and O-isotope compositions of Andahua-Huambo lavas reveal that these magmas evolved at high pressure in the so-called MASH zone, wheater by garnet-dominated AFC processes or lower crust partial melting leaving a garnet-bearing residue (Delacour et al., 2007; Sorensen and Holm, 2008; Huang et al., 2017).

In order to identified the arc magma sources of this part of the Andes, we followed the systematics proposed by Blum-Oeste and Wörner (2016), which suggest that CVZ magmas resulted from a mixture of a mantle-derived basaltic andesite (BA); an enriched basalt (EB); a crust-derived rhyodacite (RD) (Fig. 9). In a Sr *vs.* SiO_2 plot most ASCV compositions (at least the most primitive ones) fall inside the triangle formed by the previous end-members, and seems to define two different trends, the first one composed by the andesites and dacites of the groups 1 and 2; and the second defined by the group 3 dacites. It is worth to note that SA 1033E sample, that represent the local mafic end-member for group 1 and group 2 fall relatively close to the mixing line formed between the two primitive end-members (BA and EB), whereas the intermediate and silica-rich compositions of groups 1 and 2 point to the high-silica end-member (RD). In contrats, the the group 3 dacites plot outside the previously defined triangle. In this diagram, Andahua-Huambo compositions define a trend with a break-in-slope around 57 wt.% SiO_2. The andesitic and dacitic compositions tend to merge the ASCV trend, whereas the low-silica compositions fall along the BA-EB side, confirming the fact that primitive magmas in this part of the arc are not homogeneous. Based on this analysis, we propose that parental magmas for the group 1 and 2 should be different than that of the group 3.

6.2. Intracrustal processes

Ampato-Sabancaya magmas resulted from extensive crustal processing that include fractional crystallization, crustal assimilation, and magma mixing. We discuss the mineralogical and geochemical evidence for each of these processes.

6.2.1. Fractional crystallization

Several mineralogical and geochemical characteristics indicate that fractional crystallization (FC) played an important role during the evolution of Ampato-Sabancaya magmas. Among these characteristics are: (a) the presence of zoned plagioclase, clinopyroxene, and olivine phenocrysts; (b) the modal compositions of the main minerals that vary with magmatic differentiation; (c) the well-correlated trends between some incompatible elements (*e.g.*, Rb *versus* Th, Fig. 10a); and (d) the depletion in compatible elements (*e.g.*, Ni, Cr, Sr, Yb) along differentiation trends (Fig. 4, 10b). Trace element variations clearly indicate mineral fractionation, such as decreases in Ni and Cr with increasing silica contents which suggest olivine and clinopyroxene fractionation. Depletion in MREE and HREE usually indicate amphibole and/or garnet crystallization, whereas the negative trend observed in the MREE/HREE (e.g., Dy/Yb) *vs.* SiO_2 diagram clearly suggests a leading role for amphibole fractionation (Fig. 11a). The decrease of Sr suggests plagioclase fractionation (Fig. 4), a process that is corroborated by the relatively weak negative Eu anomaly observed in most ASCV samples (Fig. 5).

To test our hypothesis that fractional crystallization occurred, we perform a two-step geochemical modelling procedure. First, major element mass-balance calculations (Störmer and Nicholls, 1978) between mafic and felsic end-members of the groups 1 and 2 (SA-1033E and SA-1169A, respectively) allow us to estimate the modal composition of the cumulate (64-65% Pl + 18-23% Amp + 5-7 Bt + 2-4% Cpx + 5-6% Ti-Mag), as well as the degree of crystallisation (72%) required to evolve from a basaltic andesite to a dacite magma. It is noteworthy that the modal composition of the cumulate estimated from such calculations is similar to the observed mineral assemblage in ASCV eruptive products. Second, the calculated values are entered into the trace-element modelling equations of Rayleigh (1896) (details on mathematical procedures are given in Janousek et al., 2015). For the trace element modelling, we used the partition coefficients for

siliceous liquids of Martin (1987), Rollinson (1993), and Bachmann et al. (2005). We would stress that the geochemical modelling approch is challenging for highly porphyritic rocks (up to 30-40 vol.% crystals), which cannot be considered as true magmatic liquids following a liquid-line-of-descent. In addition, the geochemical dispersion observed in some diagrams such as Rb *versus* Ni (Fig. 10b) suggests that fractional crystallization alone cannot explain the observed geochemical diversity, indicating a more complex scenario. For example, in this geochemical space, the olivine-clinopyroxene-dominated fractional crystallization trend produces a noticeable decrease in Ni contents whereas Rb should be slightly increased. In addition, during fractional crystallization the ratio between two incompatible elements will not change drastically and samples related through fractional crystallization should define an approximately horizontal line if plotted against a fractionation index. This is not the case, as demonstrated by the K/Rb ratio which decreases with increasing Rb concentration (Fig. 11b). Thus, despite mineralogical and geochemical data suggesting an important role of fractional crystallization of a cumulate composed of plagioclase, pyroxenes, amphibole, and Fe-Ti oxides, other processes such as magma mixing and crustal assimilation must also be involved.

6.2.2. Assimilation-fractional crystallization (AFC)

The ASCV data supports the hypothesis that crustal contamination played a key role in andesite and dacite magma genesis. The curved trend observed in K/Rb *vs.* Rb (Fig. 11b) demonstrates that Rb is more incompatible than K, a trend commonly present in other CVZ magmatic series and associated with AFC process (Davidson et al., 1990). In addition, $^{87}Sr/^{86}Sr$ positively correlates to SiO_2 content (Fig. 6b) while $^{143}Nd/^{144}Nd$ is negatively correlated to SiO_2 content in Ampato-Sabancaya samples (not shown). Such relationships are typical of crustal contamination (Leeman and Hawkesworth, 1986;

DePaolo, 1981) and are widely documented in lavas throughout the CVZ (e.g., Thorpe et al., 1984; Hildreth and Moorbath, 1988; Davidson et al., 1991; Gerbe and Thouret, 2004; Delacour et al., 2007; Sørensen and Holm, 2008; Mamani et al., 2010; Godoy et al., 2014; Rivera et al., 2017). Additionally, Pb isotope ratios for Ampato-Sabancaya eruptive products ($18.17<^{206}Pb/^{204}Pb<18.49$; $15.61<^{207}Pb/^{204}Pb<15.63$, and $38.55<^{208}Pb/^{204}Pb<38.72$) point to those reported for the regional metamorphic basement (Barreiro and Clark, 1984; Mamani et al., 2008; Figs. 7a and b), providing evidence that the Ampato-Sabancaya magmas assimilated significant amounts of Arequipa Massif basement during their ascent.

Consequently, to account for isotopic and trace element constraints, we test alternative models combining fractional crystallization with the assimilation of wall-rocks surrounding the magma reservoirs (AFC, DePaolo, 1981) (curve 1, Fig. 12). The amount of assimilated material correlates to the quantity of magma that has crystallized through ascent and cooling. For AFC modelling, we use the same parameters as the FC model, varying fractionation/assimilation ratios (r = 0.2), and the Precambrian Charcani gneiss to represent the local upper continental crust composition (Boily et al., 1989; Sorensen and Holm, 2008; Rivera et al., 2017; Samaniego et al., 2020). The modelling results for our AFC model are shown in Fig. 12. Using these parameters, we can reproduce the geochemical diversity of andesites and dacites of groups 1 and 2. We stress that group 3 dacites cannot be modeled because, as showed in a previous section (see Fig. 9), the parental magmas of these dacites are different than that of the other ASCV magmas.

6.2.3 Magma mixing

A magma mixing process is also suggested by the frequent disequilibrium textures and chemical zoning patterns observed in ASCV rocks. For example, rocks emitted in the 1990-1998 Sabancaya eruptions frequently have disequilibrium textures (*e.g.*, hybrid andesites with a mixed population of plagioclase phenocrysts). Gerbe and Thouret (2004) interpreted such features as evidence of mixing between andesitic and dacitic end-members during repeated injections of mafic magmas into the base of a ~6 km-deep reservoir. In general, we observe: (a) reversely zoned plagioclase phenocrysts with "wavy" dissolution surfaces between the core and rim, and Ca-rich overgrowth rims; (b) clinopyroxene, orthopyroxene, and amphibole phenocrysts have reverse zoning, particularly in the outermost rims; (c) high Mg# and Cr_2O_3 contents in some clinopyroxene phenocrysts suggest that these minerals crystallized from more primitive magmas. (d) banding textures observed at in some units of Ampato (AM-II5) and Sabancaya, indicating that magma mixing and mingling must be taken into account when interpreting the diversity of Ampato-Sabancaya magmas.

A magma mixing scenario is additionally suggested by the positive and negative correlations of some trace elements against silica (Fig. 4), linear correlations among incompatible trace elements, hyperbola-like trends in diagrams of incompatible trace element ratios (Clynne, 1999), and the distribution of compatible *versus* incompatible elements (e.g., Ni *vs.* Rb diagram, Fig. 9b). To identify the main process responsible for the geochemical diversity recorded by ASCV magmas, we follow the trace element systematics of Langmuir et al. (1978) and Schiano et al. (2010) which enable us to distinguish between partial melting, fractional crystallization, and mixing processes. Plotting Rb, an incompatible element, and V, a compatible element, in a Rb/V *versus* 1/V diagram, yields a a linear trend for most samples (Fig. 13) that suggests a binary mixing process between a mafic mantle-derived end-member and a silica-rich end-member.

To test the magma mixing hypothesis in the ASCV series, we apply a trace element mass-balance mixing model with mafic and siliceous end-members using the equations of Langmuir et al. (1978). This model accurately describes the geochemical diversity of both magmatic series (curve 2, Fig. 13), and allows us to constrain both basic and silicic end-members. The basic end-member is represented by the most magnesian (group 1), mantle-derived magmas of the Ampato edifice (*e.g.*, SA-1033E). This mafic end-member is depleted in incompatible trace elements, such as LILE and LREE, and has low values for trace element ratios (*e.g.*, Th/La, La/Yb). In contrast, this end-member has high concentrations of most compatible elements such as HREE and the transition metals. The silicic end-member is represented by group 2 dacites (*i.e.*, SA-0914), which are characterized by enrichment in most incompatible elements, as well as low concentrations of compatible elements. Additionally, in the geochemical spaces represented in Fig. 13, an extrapolation of the mixing model beyond the silicic end-member potentially leads to group 3 dacite compositions. We stress, however, that trace elements systematics (Fig. 4) demonstrate that group 2 dacites are geochemically different from group 3 dacites, implying that two different "recipes" are needed to produce these distinct silica-rich magmas.

6.3. The origin of Ampato dacites: different sources or different levels of differentiation?

As mentioned, Ampato dacites display two contrasting geochemical signatures. Group 2 dacites are characterized by depletion in HREE and Y, which yield high Sr/Y (50.91–60.50) and Dy/Yb (2.14–2.61) ratios (Fig. 11a). Additionally, they have high $^{87}Sr/^{86}Sr$ (0.7068–0.7070), $^{206}Pb/^{204}Pb$ (18.2098–18.2537), $^{207}Pb/^{204}Pb$ (15.6136–15.6159), and $^{208}Pb/^{204}Pb$ (38.5464–38.5791) ratios. In contrast, group 3 dacites have

774 particular geochemical and isotopic feature that differ from most Ampato-Sabancaya
775 eruptive products. These dacites show high concentrations in HREE and Y compared to
776 andesites and dacites from group 2, and as a result these dacites also yield very low Dy/Yb
777 ratios (1.76–2.14, Fig.11a). In addition, group 3 dacites yield very high Sr isotopic ratios
778 (0.7074–0.7075).

779 The relatively low Yb and Y contents of most Ampato-Sabancaya andesites and
780 dacites might have been acquired during the first stage of evolution in the lower crust
781 through AFC processes involving garnet and/or amphibole from primitive mantle-derived
782 parental magma (e.g., Davidson et al., 1990, 1991; Kay, 2002; Haschke et al., 2006;
783 Sørensen and Holm, 2008; Mamani et al., 2010). Then, in a second step, amphibole-
784 dominated, upper crustal AFC processes would be responsible for the formation of group
785 2 andesites and dacites.

786 In contrast, the low Sr/Y and Dy/Yb ratios of group 3 dacites clearly indicate a
787 magmatic evolution under conditions where garnet and/or amphibole are *not* stable
788 mineralogical phases (Taylor and McLennan, 1988; Alonso-Pérez et al., 2009). However,
789 given that Sr and Pb isotopic ratios are high for both dacite groups, significant crustal
790 contamination occurs. We propose that group 3 dacites formed at upper crustal levels,
791 following and AFC process in which amphibole do not play a leading role. Thus, two
792 contrasting processes are responsible for the origins of both dacite groups. These
793 processes differ on the depth at which crustal contaminations occurs, with deeper levels
794 for group 2 and shallow levels for group 3 (Fig. 14). This difference suggests that a
795 complex magma plumbing system exists below the ASVC and implies that the
796 voluminous explosive eruptions that produced the Corinta Plinian tephra-fall deposits of
797 the group 3 dacites required the development of large upper crustal reservoirs. In addition,
798 as mentioned before, the parental magmas of the group 3 dacites seems to be different of

that feeding the main ASCV plumbing system, which implies that these magmas by passed the deep crustal source and then they did not acquire the classical HREE-depleted garnet-signature of the other ASCV magmas.

7. Conclusions

During about the last 500 ky, Ampato-Sabancaya eruptive products have geochemical and isotopical variations that define three different geochemical groups: (1) a group of andesites corresponding to old eruptive products of Ampato Basal edifice and Ampato Upper edifice; (2) a group of andesites and dacites that represent the main magmatic series covering most eruptive products of Ampato and Sabancaya; and (3) a volumetrically minor group of dacites displaying a different geochemical signature (compared with group 2 dacites). On one hand, most eruptive products of Ampato and Sabancaya volcanoes (groups 1 and 2) follow a two-step differentiation model in which primitive mafic magmas generated by partial melting of the metasomatized mantle wedge rise and accumulate at lower crustal reservoirs, where they evolved by AFC processes involving garnet and/or amphibole. This step is responsible for the HREE depletion and highly radiogenic signature of ASCV magmas. Trace element and isotope concentrations suggest that the Precambrian Charcani gneiss is the most likely crustal contaminant. At upper crustal levels, magmatic evolution is dominated, on one hand by magma mixing between two end-members producing the most common andesites and dacites of group 2. On the other hand, group 3 dacites seem to result of upper crust AFC process from primitive magmas different than that produced the main ASCV trend.

Acknowledgements

This work is part of two Peruvian-French cooperation programmes carried out between the Institut de Recherche pour le Développement (IRD, France) and both the Instituto Geofísico del Perú (IGP) and the Instituto Geológico, Minero y Metalúrgico (INGEMMET). We thank J.L. Devidal (Laboratoire Magmas et Volcans, France) for help provided during the microprobe analyse. We warmly thank C. Harpel for comments and language improvements to the previous version of this manuscript. Constructive comments from the Editor, Dr. Greg Shellnutt, and the reviewers Drs. Chris Conway and John Adam have significantly improved the manuscript. This is Laboratory of Excellence ClerVolc contribution No. XX.

References

Alcalá-Reygosa, J., Palacios, D., Vázquez-Selem, L., 2017. A preliminary investigation of the timing of the local last glacial maximum and deglaciation on Hualca Hualca volcano – Patapampa Altiplano (arid Central Andes, Peru). Quaternary International 449; 149-160.

Alonso-Pérez, R., Müntener, O., Ulmer, P., 2009. Igneous garnet and amphibole fractionation in the roots of island arcs: experimental constraints on andesitic liquids. Contributions to Mineralogy and Petrology. 157, 541-558.

Ancellin, M.A., Samaniego, P., Vlastélic, I., Nauret, F., Gannoun, A., Hidalgo, S., 2017. Across-arc versus along-arc Sr-Nd-Pb isotope variations in the Ecuadorian volcanic arc, Geochemistry, Geophysics, Geosystems 18, 1163-1188.

Bachmann, O., Dungan, M. A., Bussy, F., 2005. Insights into shallow magmatic processes in large silicic magma bodies: the trace element record in the Fish Canyon magma body, Colorado. Contributions to Mineralogy and Petrology, 149; 338-349.

Barreiro, B.A., Clark, A.H., 1984. Lead isotopic evidence for evolutionary changes in magma-crust interaction, Central Andes, southern Peru. Earth and Planetary Science Letters 69, 30-42.

Beck, S.L., Zandt, G., Myers, S.C., Wallace, T.C., Silver, P.G., Drake, L., 1996. Crustal-thickness variations in the central Andes. Geology 24 (5), 407-410.

Blum-Oeste, M., Wörner, G., 2016. Central andean magmatism can be constrained by three ubiquitous end-members. Terra. Nova 28 (6), 434–440.

Boily, M., Brooks, C., Ludden, J.N., James, D.E., 1989. Chemical and isotopic evolution of the Coastal Batholith of southern Peru. Journal of Geophysical Research B, 94, 9, 12483–12498.

Bromley, G.R.M., Schaefer, J.M., Wincler, G., Hall, B.L., Todd, C.E., Rademaker, C.K.M., 2009. Relative timing of last glacial maximum and late-glacial events in the central tropical Andes. Quaternary Science Reviews, 28, 2514-2526.

Bromley, G., Thouret, J.-C., Schimmelpfennig, I., Mariño, J., Valdivia, D., Rademaker, K., del Pilar Vivanco Lopez, ASTER Team, Aumaitre, G., Bourles, D., Keddadouche, K., 2019. In situ cosmogenic ^{3}He and ^{36}Cl and radiocarbon dating of volcanic deposits refine the Pleistocene and Holocene eruption chronology of SW. Peru. Bulletin of Volcanology 81:64.

Bulmer, M., Johnston, A. Engle, F., 1999. Analysis of Sabancaya volcano, souther Peru using Radarsat and Landsat TM data. Application Development and Research Opportunity (ADRO) 10 pp.Burns D., H. de Silva S., L. (2023), Andesites and evolution of the continental crust: Perspectives from the Central Volcanic Zone of the Andes. Frontiers in Earth Science. 10:961130.

Caldas, J., 1973. Cuadrángulo de Huambo (32-r), escala 1:100000. INGEMMET, Peru. 1 geological map.

872 Clynne, M.A. 1999. A complex magma mixing origin for rocks erupted in 1915, Laseen
873 Peak, California. Journal of Petrology 40(1): 105–132.
874 Cotten, J., Le Dez, A., Bau, M., Carroff, M., Maury, R.C., Dulski, P., Fourcade, S., Bohn,
875 M., Brousse, R., 1995. Origin of anomalous rare-earth element and Yttrium
876 enrichments in subaerial exposed basalts: Evidence from French Polynesia. Chemical
877 Geology 119, 115–138.
878 Dalmayrac, B., Lancelot, J.R., Leyreloup, A. 1977. Two-billion-year granulites in the
879 Late Precambrian metamorphic basement along the Southern Peruvian coast. Science
880 198: 49–51.
881 Davidson, J.P., McMillan, N.J., Moorbath, S., Wörner, G., Harmon, R.S., López Escobar,
882 L., 1990. The Nevados de Payachata volcanic region (18°S/69°W, N. Chile) II.
883 Evidence for widespread crustal involvement in Andean magmatism. Contributions to
884 Mineralogy and Petrology 105, 412–432.
885 Davidson, J.P., Harmon, R.S., Wörner, G., 1991. The source of the Central Andes
886 magmas; some considerations. *In* Andean magmatism and its tectonic setting.
887 Geological Society of America-Special Paper, 265, 233–243.
888 Delacour, A., Gerbe, M.-C., Thouret, J.-C., Wörner, G., Paquereau-Lebti, P., 2007.
889 Magma evolution of Quaternary minor volcanic centres in southern Peru, Central
890 Andes. Bulletin of Volcanology, 69 (6): 581–608.
891 Delph, J. R., Ward, K. M., Zandt, G., Ducea, M. N., Beck, S. L., 2017. Imaging a magma
892 plumbing system from MASH zone to magma reservoir. Earth and Planetary Science
893 Letters, 457, 313–324.
894 DePaolo, D.J., 1981. Trace element and isotopic effects of combined wallrock
895 assimilation and fractional crystallization. Earth Planetary Science Letters 53, 89–202.

De Silva S.L., Francis P.W., 1991. Volcanoes of the Central Andes. Berlin: Springer - Verlag, 216 p.

Feeley T.C., Sharp Z.D., 1995. $^{18}O/^{16}O$ isotope geochemistry of silicic lava flows erupted from Volcan Ollagüe, Andean Central Volcanic Zone. Earth and Planetary Science Letters 133:239–254.

Freymuth, H., Brandmeier, M., Wörner, G., 2015. The origin and crust/mantle mass balance of central andean ignimbrite magmatism constrained by oxygen and strontium isotopes and erupted volumes. Contributions to Mineralogy and Petrology 169 (6), 58.

Galer, S.J.G., Abouchami, W., 1998. Practical application of lead triple spiking for correction of instrumental mass discrimination. Mineralogical Magazine 62A:491–492.

Gerbe, M.C., Thouret, J.C., 2004. Role of magma mixing in the petrogenesis of lavas erupted through the 1990-98 explosive activity of Nevado Sabancaya in south Peru. Bulletin of Volcanology 66, 541–561.

Godoy, B., Wörner, G., Kojima, S., Aguilera, F., Simnon, K., 2014. Low-pressure evolution of arc magmas in thickened crust: The San Pedro-Linzor volcanic chain, Central Andes, Northern Chile. Journal of South American Earth Sciences 52, pp. 24–42.

Harpel, C., de Silva, S., Salas, G., 2011. The 2 ka eruption of Misti volcano, southern Peru-The most recent Plinian eruption of Arequipa's iconic volcano. Geological Society of America Special papers 484, 72 pp.

Harmon, R.S., Thorpe, R.S., Francis, P.W., 1981. Petrogenesis of Andean andesites from combined O-Sr relationship. Nature 290, 396–399.

Harmon, R.S., Barreiro, B.A., Moorbath, S., Hoefs, J., Francis, P.W., Thorpe, R.S, Déruelle, B., McHugh, J., Viglino, J.A., 1984. Regional O-, Sr-, and Pb-isotope

relationships in late Cenozoic calc-alkaline lavas of the Andean Cordillera. Journal of the Geological Society of London 141, 5, 803–822.

Haschke, M.R., Siebel, W., Günther, A., Scheuber, E., 2002. Repeated crustal thickening and recycling during the Andean orogeny in north Chile (21°-26°S): Journal of Geophysical Research, 107, 1–18.

Haschke, M., Günther, A., Melnick, D., Echtler, H., Reutter, K.-J., Scheuber, E., Oncken, O., 2006. Central and Southern Andean tectonic evolution inferred from arc magmatism. In: Oncken, O., Chong, G., Franz, G., Giese, P., Götze, H.-J., Ramos, V.A., Strecker, M.R., Wigger, P. (Eds.), The Andes Active Subduction Orogeny, Frontiers in Earth Sciences, vol. 1. Springer, Heidelberg, Berlin, Germany, pp. 337–353.

Hildreth, W., Moorbath, S., 1988. Crustal contributions to arc magmatism in the Andes of Central Chile. Contributions to Mineralogy and Petrology 98(4): 455–489.

Huang, F., Sorensen, E., Holm, P., Zhang, Z.-F., Lundstrom, C., 2017. U-series disequilibria of trachyandesites from minor volcanic centers in the Central Andes. Geochimica et Cosmochimica Acta 215, 92–104.

James, D.E., 1982. A combined O, Sr, Nd, and Pb isotopic and trace element study of crustal contamination in central Andean lavas, I. Local geochimical variations. Earth and Planetary Science Letters 57, 47–62.

Janoušek, V., Moyen, J-F., Martin, H., Erban, V., Farrow, C., 2015. Geochemical modelling of igneous processes: Bringing the power of R to a geochemical community. Springer Geochemistry; Springer-Verlag Berlin and Heidelberg, 345 p.

Juvigné, E., Thouret, J.-C., Loutsch, I., Lamadon, S., Frechen, M., Fontugne, M., Rivera, M., Marino, J., 2008. Téphrostratigraphie et chronologie dans la region des Nevados Ampato et Sabancaya, sud du Pérou. Quaternaire 19, 161–178.

946 Kay, S.M., Mpodosiz, C., Coira, B., 1999. Neogene magmatism, tectonics, and mineral
947 deposits of the Central Andes (22 to 33° S). *In:* Skinner B.S. (ed) Geology and Ore
948 deposits of the Central Andes. Society of Economic Geological Special Publication, 7,
949 27–59.
950 Kay, S.M., 2002. Andean adakites from slab melting, crustal thickening, and fore-arc
951 subduction erosion. 5th International Symposium of Andean Geodynamics, 405–408.
952 Kay, S.M., Coira, B., Caffe, P.J., Chen, C-H., 2010. Regional chemical diversity, crustal
953 and mantle sources and evolution of central Andean Puna Plateau Ignimbrites. Journal
954 of Volcanology and Geothermal Research, 198: 81–111.
955 Langmuir, C.H., Vocke, R.D., Hanson, G.N., Hart, S.R., 1978. A general mixing equation
956 with applications to Icelandic basalts. Earth and Planetary Science Letters 37 (3), 380–
957 392.
958 Leake, B.E., Woolley, A.R., Arps, C.E.S., Birch, W.D., Gilbert, M.C., Grice, J.D.,
959 Hawthorne, F.C., Kato, A., Kish, H.J., Krivovichev, V.G., Linthout, K., Laird, J.,
960 Mandarino, J., Maresch, W.V., Nickel, E.H., Schumaker, J.C., Smith, D.C.,
961 Stephenson, N.C.N., Ungaretti, L., Whittaker, E., J.W., Youzhi, G., 1997.
962 Nomenclature of Amphiboles; report of the subcommittee on amphiboles of the
963 International Mineralogical Association Commission on New Minerals and Mineral
964 Names. Mineralogical Magazine 61, 295–321.
965 Leeman, W. P., Hawkesworth, C. J., 1986. Open magma systems: Trace element and
966 isotopic constraints: Journal of Geophysical Research, v. 91, p. 5901–5912.
967 Loewy, S.L, Connelly, J.N., Dalziel, I.W.D., 2004. An orphaned basement block: The
968 Arequipa-Antofalla Basement of the central Andean margin of South America.
969 Geological Society of America Bulletin 166, 171–187.

970 Mamani, M., Tassara, A., Worner, G., 2008. Composition and structural control of
971 cortical domains in the central Andes. Geochemistry Geophysics Geosystems 9, 3, 1–
972 13.
973 Mamani, M., Worner, G., Sempere, T., 2010. Geochemical variation in igneous rocks of
974 the Central Andean orocline (13 ºS to 18 ºS): Tracing crustal thickening and magmas
975 generation through time and space. Geological Society of America Bulletin 97:241–
976 254.
977 Martin, H., 1987. Archaean and modern granitoids as indicators of changes in
978 geodynamic processes. Revista Brasileira de Geociências 17, 360–365.
979 Morimoto, N., Fabries, J., Ferguson, A.K., Ginzburg, I.V., Ross, M., Seifert, F.A.,
980 Zussman, J., 1988. Nomenclature of pyroxenes. American Mineralogist 73, 1123–
981 1133.
982 Mukasa, S.B., 1986, Zircon U-Pb Ages of Super-Units in the Coastal Batholith, Peru -
983 Implications for Magmatic and Tectonic Processes: Geological Society of America
984 Bulletin, v. 97, p. 241–254.
985 Nauret, F., Samaniego, P., Ancellin, M.A., Tournigand, P.Y., Le Pennec, J.L., Vlastélic,
986 I., Gannoun, A., Hidalgo, S., Schiano, P., 2018. The genetic relationship between
987 andesites and dacites at Tungurahua volcano, Ecuador. Journal of Volcanology and
988 Geothermal Research 349:283–297.
989 Norabuena, E., Leffler-Griffin, L., Mao, A., Dixon, T., Stein, S., Sacks, I.S., Ocola, L.,
990 Ellis, M., 1998. Space geodetic observation of Nazca-South America convergence
991 across Central Andes. Science 279, 358–362.
992 Peccerillo, P., Taylor, S.R., 1976. Geochemistry of Eocene calc-alkaline volcanic rocks
993 from the Kastamonu area. Northern Turkey. Contributions to Mineralogy and
994 Petrology 58, 63–81.

995 Pin, C., D. Briot, Bassin, C., Poitrasson F., 1994. Concomitant separation of strontium
996 and samarium-neodymium for isotopic analysis in silicate samples, based on specific
997 extraction chromatography. Analytica Chimica Acta, 298, 209–217.
998 Pin, C. Santos Zalduegui, J. F., 1997. Sequential separation of light-rare-earth elements,
999 thorium and uranium by miniaturized extraction chromatography: Application to
1000 isotopic analyses of silicate rocks. Analytica Chimica Acta 339, 79–89.
1001 Prival J.M., Thouret, J.C., Japura, S., Gurioli L., Bonadonna, C., Mariño, J., Cueva, K.,
1002 2020. New New insights into eruption source parameters of the 1600 CE Huaynaputina
1003 Plinian eruption, Peru. Bulletin of Volcanology 82:7
1004 Rayleigh, J., 1896. Theorical considerations respecting the separation of gases by
1005 diffusion and similar processes. Philosophical Magazine 42, 77–107.
1006 Rehkamper, M., Hofmann, A.W. 1997. Recycled ocean crust and sediment in Indian
1007 Ocean MORB. Earth and Planetary Science Letters 147(1-4):93–106
1008 Rivera, M., Mariño, J., Samaniego, P., Delgado, R., Manrique, N., 2016. Geología y
1009 evaluación de peligros del complejo volcánico Ampato - Sabancaya (Arequipa),
1010 INGEMMET. Boletín, Serie C: Geodinámica e Ingeniería Geológica, 61, 122 p., 2
1011 maps.
1012 Rivera, M., Martin, H., Le Pennec J.L., Thouret, J.C., Gourgaud, A., Gerbe, M.Ch., 2017.
1013 Petro-geochemical constraints on the source and evolution of magmas at El Misti
1014 volcano (Peru). Lithos 268-271, 240–259.
1015 Rollinson H. R., 1993. Using Geochemical Data: Evaluation, Presentation, and
1016 Interpretation. Longman Scientific and Technical, Wiley and Sons, New York. 352 p.
1017 Romero, D., Ticona, P. 2003. Memoria descriptiva de la revisión y actualización del
1018 cuadrángulo de Huambo (32–r), scale 1:50 000. INGEMMET, 27 p, 4 maps.

1019 Samaniego, P., Valderrama, P., Mariño J., Van Wyk de Vries, B., Roche, O., Manrique,
1020 N., Chedeville C., Liorzou, C., Fidel L., Malnati, J., 2015. The historical (218±14 aBP)
1021 explosive eruption of Tutupaca volcano (Southern Peru). Bulletin of Volcanology 77,
1022 51–69.
1023 Samaniego, P., Rivera, M., Mariño, J., Guillou, H., Liorzou, C., Zerathe, S., Delgado, R.,
1024 Valderrama, P., 2016. The eruptive chronology of the Ampato-Sabancaya volcanic
1025 complex (Southern Peru). Journal of Volcanology and Geothermal Research 323:110–
1026 128.
1027 Samaniego, P., Rivera, M., Manrique, N., Schiavi, F., Nauret, F., Liorzou, C., Ancellin,
1028 M.-A., 2020. Linking magmatic processes and magma chemistry during the post-
1029 glacial to recent explosive eruptions of Ubinas volcano (southern Peru). Journal of
1030 Volcanology and Geothermal Research, 407, 107095.
1031 Schiano, P., Monzier, M., Eissen, J.-P., Martin, H., Koga, K.T., 2010. Simple mixing as
1032 the major control of the evolution of volcanic suites in the Ecuadorian Andes.
1033 Contributions to Mineralogy and Petrology 160 (2), 297–312.
1034 Siebert, L., Simkim, T., Kimberley, P., 2010. Volcanoes of the World. Third Edition.
1035 Smithsonian Institution, Washington, University of California, pp. 537.
1036 Sørensen, E.V., Holm, P.M., 2008. Petrological inferences on the evolution of magmas
1037 erupted in the Andahua Valley, Peru (Central Volcanic Zone). Journal of Volcanology
1038 and Geothermal Research 177, 378–396.
1039 Stern, Ch. R., 2004. Active Andean volcanism: its geologic and tectonic setting. Revista
1040 Geológica de Chile 31, 161–206.
1041 Störmer, J.-C., Nicholls, J., 1978. Xlfrac: a program for the interactive testing of
1042 magmatic differentiation models. Computers Geosciences 4, 143–159.

1043 Sun, S., McDonough, W.F., 1989. Chemical and isotopic systematics of oceanics basalts:
1044 Implications for mantle composition and processes. En Saunders A., and Norry M.
1045 (eds). Magmatism in the Ocean Basins. Geological Society of London Special
1046 Publication 42, 313–345.
1047 Taylor, S.R., McLennan, S.M., 1988. The significance of the rare earths in geochemistry
1048 and cosmochemistry. In: Gschneidner Jr., K.A., Eyring, L. (Eds.), Handbook on the
1049 Physics and Chemistry of Rare Earths, vol. 11, pp. 485–578.
1050 Thorpe, R.S., Francis, P.W., Callaghan, O.L., 1984. Relative roles of source composition,
1051 fractional crystallization and crustal contamination in the petrogenesis of Andean
1052 volcanic rocks, *In:* S. Moorbath, A.B. Thompson, E.R. Oxburgh, (editors), The relative
1053 contributions of mantle, oceanic crust and continental crust to magma genesis, Volume
1054 310: Series A: Mathematical and Physical Sciences, Philosophical Transactions of the
1055 Royal Society of London, 675–692.
1056 Thouret, J.-C., Guillande, R., Huamán, D., Gourgaud, A., Salas, G., Chorowicz, J. 1994.
1057 L'activité actuelle du Nevado Sabancaya (Sud Pérou): reconnaissance géologique et
1058 satellitaire, évaluation et cartographie des menaces volcaniques. Bulletin de la Société
1059 Géologique de France, 1(165): 49–63.
1060 Thouret, J.-C., Finizola, A., Fornari, M., Suni, J., Legeley-Padovani, A., Frechen, M.,
1061 2001. Geology of El Misti volcano nearby the city of Arequipa, Peru. Geological
1062 Society of America Bulletin 113 (12), 1593–1610.
1063 Thouret, J.C., Rivera, M., Worner, G., Gerbe, M.C., Finizola, A., Fornari, M., Gonzales,
1064 K., 2005. Ubinas: the evolution of the historically most active volcano in southern
1065 Peru. Bulletin of Volcanology 67:557–589.

Travada y Córdova, V., 1752. El Suelo de Arequipa Convertido en Cielo. In: de Odriozola, M. 1877. Documentos Literarios del Perú. Tomo X. Imprenta del Estado, Lima, p. 415.

Vatin Perignon, N., Oliver, R.A., Goemans, P., Keller, F, Briqueu, L., Salas G., 1992. Geodynamic interpretations of plate subduction in the northernmost part of the Central Volcanic Zone from the geochemical evolution and quantification of the crustal contamination of the Nevado Solimana volcano, Southern Peru, Tectonophysics, 205, 329–355

Wasteneys, H.A., Clark, A.H.F., Langridege, R.J., 1995. Grenvillian granulite-facies metamorphism in the Arequipa Massif, Peru. Earth and Planetary Science Letters 132, 63–73.

Whitney, D.L., Evans, B., 2010. Abbreviations for names of rock-forming minerals. American mineralogist 95, 185–187.

Wörner, G., Harmon, R.S., Davidson, J., Moorbath, S., Turner, D., McMillan, N., Nye, C., Lopez-Escobar, L., Moreno, H., 1988. The Nevados de Payachata volcanic region (18°S/69°W, N. Chile). I. Geological, geochemical and isotopic observations. Bulletin of Volcanology 50:287–303.

Table captions

Table 1. Selected whole-rock analyses from the Ampato-Sabancaya volcanic complex: major (wt.%) and trace elements (ppm), and Sr, Nd, Pb isotopic ratios.

Table 2. Textural and mineralogical characteristics of Ampato-Sabancaya compound volcano. Mineral assemblages for each petrographic type are reported (*Pl* plagioclase, *Ol*

olivine, *Opx* orthopyroxene, *Cpx* clinopyroxene, *Amp* amphibole, *Bt* biotite, *Mag* Magnetite, *Ap* Apatite). Mineral abbreviations after Whitney and Evans (2010).

Table 3. Summary of mineralogical characteristics of Ampato-Sabancaya rocks.

Fig. 1. (a) Map showing the locations of the South American volcanic zones: Northern (NVZ), Central (CVZ), Southern (SVZ) and Austral (AVZ), modified after Stern (2004). (b) Northernmost part of CVZ in southern Peru (modified after Thouret et al., 2005). Ampato-Sabancaya compound volcano is in the middle of the Plio-Quaternary volcanic range in southern Peru, ~70 km NW of the city of Arequipa. (c) View of the western flank of Ampato and Sabancaya.

Fig. 2. Geological map of ASVC complex overlaid on a hillshade base map generated from a Digital Elevation Model (modified after Samaniego et al., 2016). Sampling sites for lavas and tephra analysed in this study are indicated by red dots. We also include the age determinations available for this volcanic centre.

Fig. 3. Microphotographs of thin sections from Ampato-Sabancaya samples. (**a)** Andesite (SA-1165) from Yanajaja stage showing a mineral assemblage composed of plagioclase, clinopyroxene, amphibole, biotite, and Fe-Ti oxides. Note the thin black aureole around the amphibole and biotite. (**b)** Dacite (SA-1159) from Ampato Upper showing a mineral assemblage composed of plagioclase, amphibole, clinopyroxene, and Fe-Ti oxides. (**c)** Dacite (SA-1155) from Ampato Upper showing a mineral assemblage composed of plagioclase, clinopyroxene, amphibole, biotite, and Fe-Ti oxides. (**d)** Rhyolitic pumice (SA-1142A) showing a mineral assemblage composed of plagioclase and biotite. (**e)**

Dacitic pumice (SA-1127D) from the Corinta tephra-fall deposit composed of plagioclase, clinopyroxene, and Fe-Ti oxides. **(f)** Disequilibrium textures in the andesite (SA-0917) from Sabancaya showing a plagioclase phenocryst with an altered (sieve) rim and a fresh overgrowth rim. Mineral abbreviations are the same as Table 2.

Fig. 4. Major and trace elements variation diagrams. Petrographic fields in the K_2O *vs.* SiO_2 diagram after Peccerillo and Taylor (1976). All major elements (except K_2O), transition elements (e.g., Ni, Cr), Sr, Sm, Zr, and possibly Yb are negatively correlated with SiO_2, while K_2O, Rb, and to some extent La are positively correlated. G1-4 correspond to the four groups identified (see text for more details).

Fig. 5. (a) Trace elements normalized to primitive mantle and (b) REE normalized to chondritic values (both after Sun and McDonough, 1989) for rocks of the evolutionary stages of ASCV. Brown area represents normalized composition of lavas and tephras from the Early andesitic stage (Ampato Basal edifice), as well as to the scoriaceous tephra-fall and pyroclastic-flow deposits of Ampato Upper edifice (Group 1). Green area represents normalized composition of lavas from the Moldepampa stage, Ampato Upper edifice, and Sabancaya edifice (Group 2). G1-4 correspond to the four groups identified.

Fig. 6. (a) $^{87}Sr/^{86}Sr$ *vs.* $^{143}Nd/^{144}Nd$ diagram for Ampato-Sabancaya rocks, compared with other published isotopic data for the CVZ, SVZ, and NVZ (Davidson et al., 1991). (b) SiO_2 *vs.* $^{87}Sr/^{86}Sr$ wt.% diagram. Insets depict the evolution of the isotopic composition during fractional crystallization (FC), mixing, and assimilation-fractional crystallization (AFC) processes. Symbols are the same as Fig. 4.

Fig. 7. (a) $^{208}Pb/^{204}Pb$ and (b) $^{207}Pb/^{204}Pb$ vs. $^{206}Pb/^{204}Pb$ diagrams of ASCV bulk rock compositions. Compositional fields of Pb isotopic values for Andean volcanic zones are from Ancellin et al. (2017). I= Isotopic fields of the southern Arequipa segment and northern Toquepala segment; II= Isotopic fields of the northern Arequipa segment; III= mafic and intermediate magmatic rocks of the Lima segment. In $^{207}Pb/^{204}Pb$ and $^{208}Pb/^{204}Pb$ *vs.* $^{206}Pb/^{204}Pb$ diagram, Ampato-Sabancaya rocks plot in the isotopic field of the southern part of Arequipa segment and northern Toquepala segment of the Peruvian Coastal batholith. DMM is Depleted MORB Mantle (Rehkamper and Hofmann, 1997). (c) $^{208}Pb/^{204}Pb$ and (d) $^{207}Pb/^{204}Pb$ vs. $^{206}Pb/^{204}Pb$ diagram of ASCV have trends consistent with assimilation in shallow crust and assimilation in deep crust (MASH processes). CG is Charcani gneiss. Symbols are the same as Fig. 4.

Fig. 8. Compositional changes of Ampato-Sabancaya's lavas and juvenile pyroclastic products through time. The chronological axis is inverse-logarithmic to account for higher sampling density and wider compositional range in young eruptive products.

Fig. 9. Sr *vs.* SiO_2 contents for Ampato-Sabancaya rocks and Andahua-Huambo volcanic province with the three end-member involved in the genesis for CVZ magmatism from Blum-Oeste and Wörner (2016).

Fig. 10. Th and Ni *vs.* Rb diagrams for Ampato-Sabancaya whole-rock samples. The plot Ni *versus* Rb display a large diversity of values which suggest a more complex scenario than simply fractional crystallization (FC). Arrows depict the evolution of magmas

composition during fractional crystallization (FC) and mixing processes. Symbols are the same as Fig. 4.

Fig. 11. a) K/Rb *vs.* Rb diagram. Arrows illustrate differentiation by fractional crystallization and AFC, binary mixing, and variable degrees of partial melting. The curved trend of the Ampato-Sabancaya samples indicate that fractional crystallization alone cannot explain the variation. b) Dy/Yb *vs.* SiO_2 wt.% diagram. The arrows show the expected effects of garnet, amphibole, and plagioclase-pyroxene fractionation. Note that amphibole is the only mineral able to efficiently fractionate MREE over HREE (i.e., Dy/Yb). Legend is given in Fig. 4.

Fig. 12. (**a)** $^{87}Sr/^{86}Sr$ *vs.* Sr (ppm), (**b)** Y (ppm), and **(c)** Co (ppm) *vs.* $^{87}Sr/^{86}Sr$ diagrams showing the curves of two petrogenetic models (indicated by numbers in parentheses) such as assimilation-fractional crystallization (AFC) and magma mixing for Ampato-Sabancaya magmas. (1) AFC model showing the effects of contamination of sample SA-1033E by the Charcani gneiss (James, 1982; Boily et al., 1990). AFC parameters are given in the figure. Circles in the curves represent the remaining proportion of melt after assimilation. Curves have been calculated according to DePaolo (1981). (2) Bulk mixing models between a basic end-member (sample SA-1033E) and a silicic end-member (sample SA-0914). Symbols are the same as Fig. 4.

Fig. 13. (a) Rb/V versus 1/V diagram for Ampato-Sabancaya wholerock samples. The linear trend highlights a binary mixing process (Schiano et al., 2010). b) Plot of Rb versus Rb/V for lavas from Ampato-Sabancaya illustrating mixing curves. A schematic C^I *vs.* C^I/C^C and $1/C^C$ *vs.* C^I/C^C diagrams are also shown with curves ilustrating melt

compositions produced by mixing, fractional crystallization, and partial melting processes. Symbols are the same as Fig. 4.

Fig. 14. Schematic diagrams illustrating the two mechanisms for andesite and dacites formation of Ampato-Sabancaya in the CVZ. (A) Mechanisms for andesite and dacites formation of group 1 and 2. (B) Mechanisms for dacites formation of group 3 (modified after Burns and de Silva, 2023).

SEM 1. Selected plagioclase, clinopyroxene, orthopyroxene, amphibole, biotite, olivine, magnetite, and ilmenite compositions (in wt.%) from Ampato-Sabancaya compound volcano lavas.

SEM 2. Major element (wt.%), trace element (ppm), Sr, Nd and Pb isotopic ratios for the Ampato-Sabancaya volcanic complex.

SEM 3. a) Ab-An-Or ternary projections for Ampato-Sabancaya plagioclase. b) Mg/(Mg + Fe^{2+}) *versus* Si (a.p.f.u., atoms per formula unit) diagram for calcic amphibole (nomenclature after Leake et al., 1997) showing that Ampato-Sabancaya amphiboles are edenite-pargasite (with: $Ca_B \geq 1.50$, $(Na+K)_A \geq 0.50$ and $Ti < 0.5$) and Magnesiohornblende-tschermakite (with: $Ca_B \geq 1.50$, $(Na+K)_A < 0.50$ and $Ca_A < 0.5$).

SEM 4. Pyroxene compositions for Ampato-Sabancaya rocks. (a) En-Wo-Fs ternary projections for pyroxene and (b) pyroxenes discriminated by Cr_2O_3 and Mg# contents.

Fig. 1

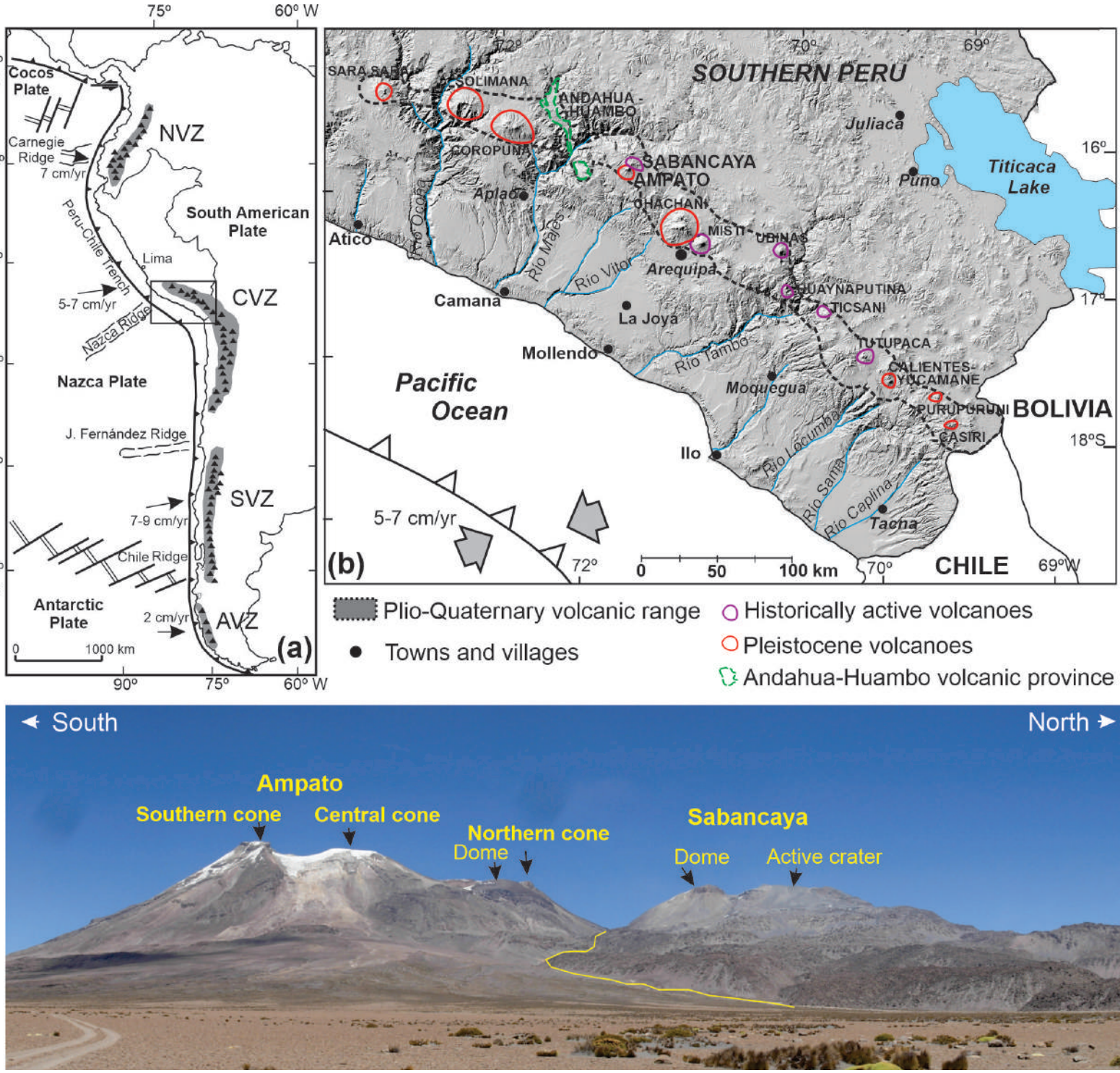
75°
60° W
10° N
0°
10°
20°
30°
40° S
Cocos Plate
Carnegie Ridge
7 cm/yr
NVZ
South American Plate
Peru-Chile Trench
Lima
5-7 cm/yr
CVZ
Nazca Ridge
Nazca Plate
J. Fernández Ridge
SVZ
7-9 cm/yr
Chile Ridge
Antarctic Plate
2 cm/yr
AVZ
0
1000 km
(a)
90°
75°
60° W
SOUTHERN PERU
SARA SARA
SOLIMANA
ANDAHUA - HUAMBO
COROPUNA
SABANCAYA
AMPATO
HACHANI
MISTI
UBINAS
Aplao
Río Ocoña
Río Majes
Río Vitor
Arequipa
HUAYNAPUTINA
TICSANI
TUTUPACA
CALIENTES-YUCAMANE
PURUPURUNI
CASIRI
Atico
Camana
La Joya
Mollendo
Río Tambo
Moquegua
Pacific Ocean
Ilo
Río Locumba
Río Sama
Río Caplina
Tacna
Juliaca
Puno
Titicaca Lake
BOLIVIA
CHILE
5-7 cm/yr
(b)
72°
70°
69°
16°
17°
18°S
0
50
100 km
69°W
Plio-Quaternary volcanic range
Towns and villages
Historically active volcanoes
Pleistocene volcanoes
Andahua-Huambo volcanic province

South
North
Ampato
Southern cone
Central cone
Northern cone
Dome
Sabancaya
Dome
Active crater

Fig. 2

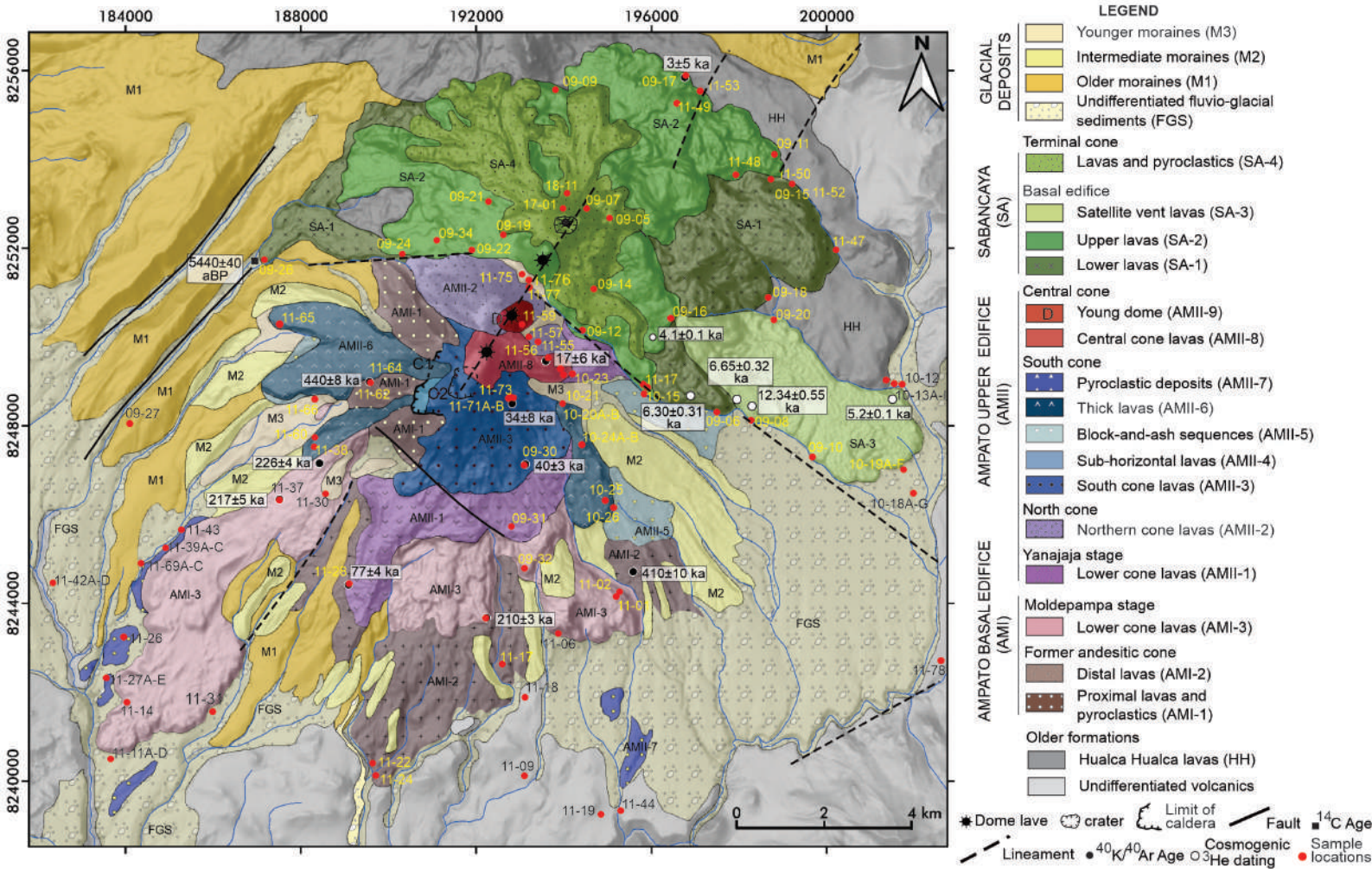
184000
188000
192000
196000
200000
8256000
8252000
8248000
8244000
8240000
N
0
2
4 km
LEGEND
GLACIAL DEPOSITS
Younger moraines (M3)
Intermediate moraines (M2)
Older moraines (M1)
Undifferentiated fluvio-glacial sediments (FGS)
SABANCAYA (SA)
Terminal cone
Lavas and pyroclastics (SA-4)
Basal edifice
Satellite vent lavas (SA-3)
Upper lavas (SA-2)
Lower lavas (SA-1)
AMPATO UPPER EDIFICE (AMII)
Central cone
Young dome (AMII-9)
Central cone lavas (AMII-8)
South cone
Pyroclastic deposits (AMII-7)
Thick lavas (AMII-6)
Block-and-ash sequences (AMII-5)
Sub-horizontal lavas (AMII-4)
South cone lavas (AMII-3)
North cone
Northern cone lavas (AMII-2)
Yanajaja stage
Lower cone lavas (AMII-1)
AMPATO BASAL EDIFICE (AMI)
Moldepampa stage
Lower cone lavas (AMI-3)
Former andesitic cone
Distal lavas (AMI-2)
Proximal lavas and pyroclastics (AMI-1)
Older formations
Hualca Hualca lavas (HH)
Undifferentiated volcanics
Dome lave
crater
Limit of caldera
Fault
14C Age
Lineament
40K/40Ar Age
3He dating
Cosmogenic
Sample locations
5440±40 aBP
440±8 ka
226±4 ka
217±5 ka
77±4 ka
210±3 ka
34±6 ka
17±6 ka
40±3 ka
410±10 ka
4.1±0.1 ka
6.65±0.32 ka
6.30±0.31 ka
12.34±0.55 ka
5.2±0.1 ka
3±5 ka

Fig. 3

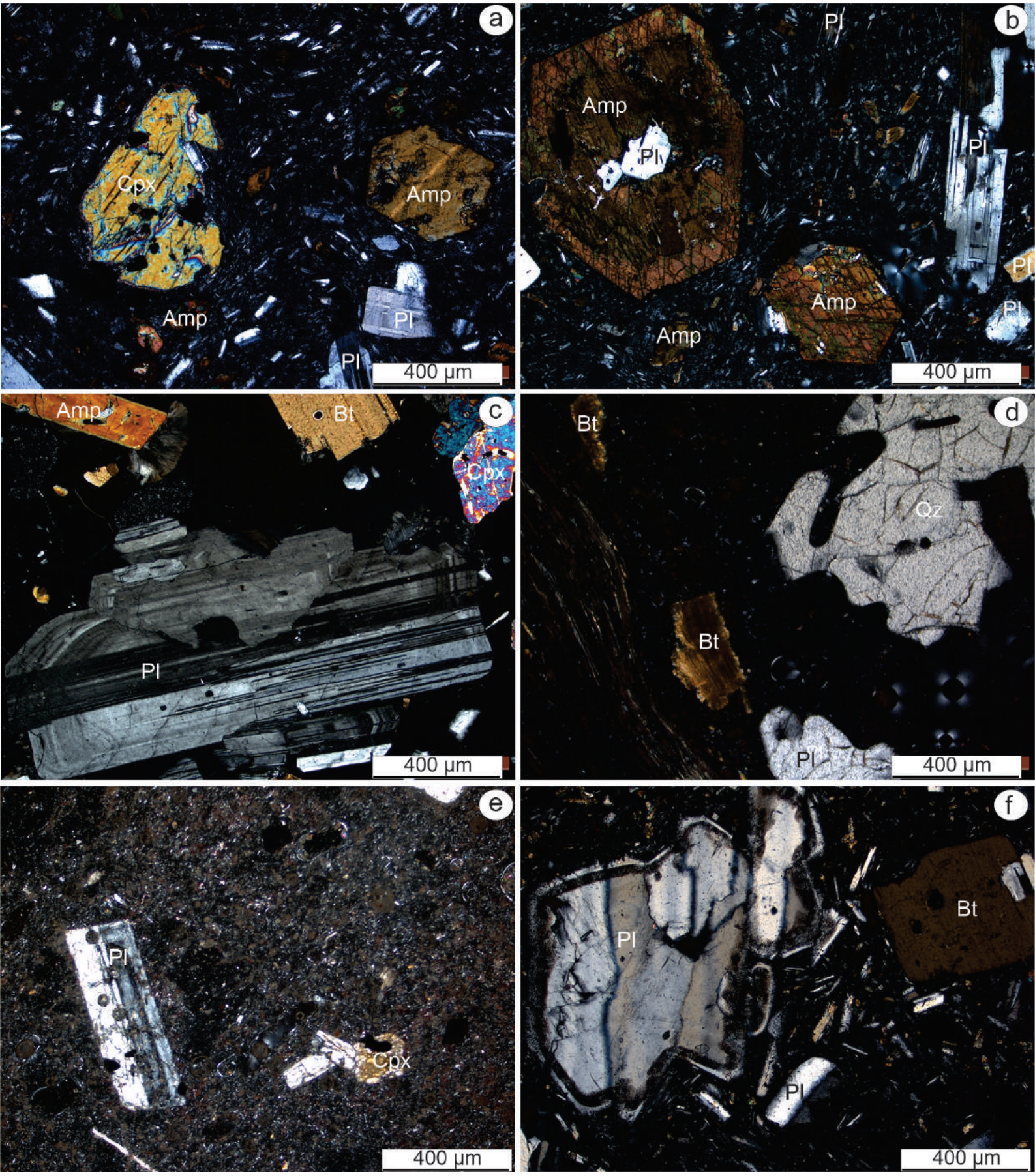
a
Cpx
Amp
Amp
Pl
Pl
400 µm
b
Pl
Amp
Pl
Pl
Pl
Amp
Amp
400 µm
c
Amp
Bt
Cpx
Pl
400 µm
d
Bt
Qz
Bt
Pl
400 µm
e
Pl
Cpx
400 µm
f
Pl
Bt
Pl
400 µm

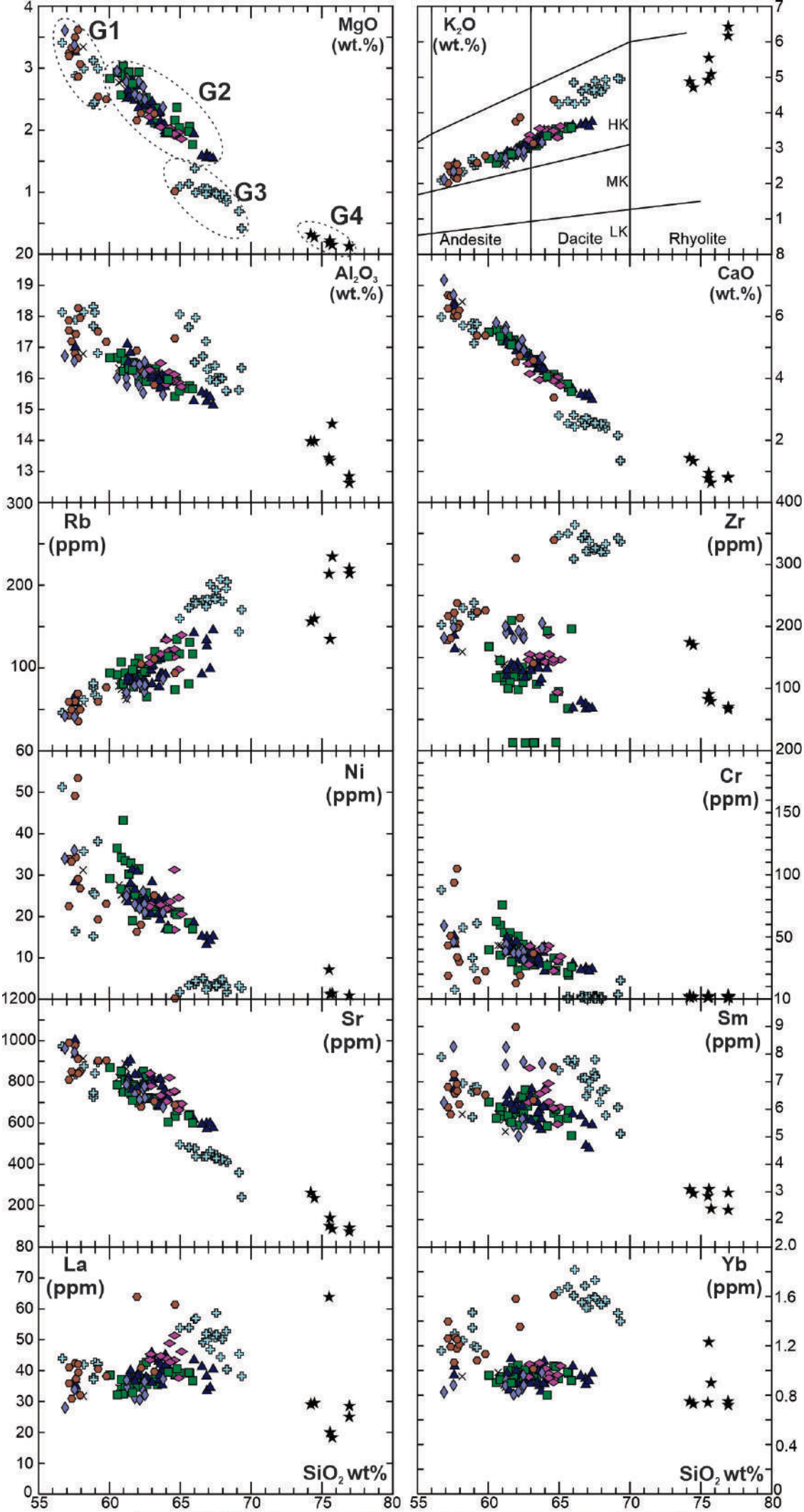
MgO (wt.%)
G1
G2
G3
G4
K2O (wt.%)
HK
MK
LK
Andesite
Dacite
Rhyolite
Al2O3 (wt.%)
CaO (wt.%)
Rb (ppm)
Zr (ppm)
Ni (ppm)
Cr (ppm)
Sr (ppm)
Sm (ppm)
La (ppm)
Yb (ppm)
SiO2 wt%
SiO2 wt%
BASAL AMPATO
Rhyolitic tephra
Moldepampa stage
Former andesitic cone
UPPER AMPATO
Corinta tephra and related scoriaceous depositis
Yanajaja stage
North, South and Central cones
SABANCAYA
2017-2018 lava
1992-1997 lava
Lava flows

Fig. 4

Fig. 5

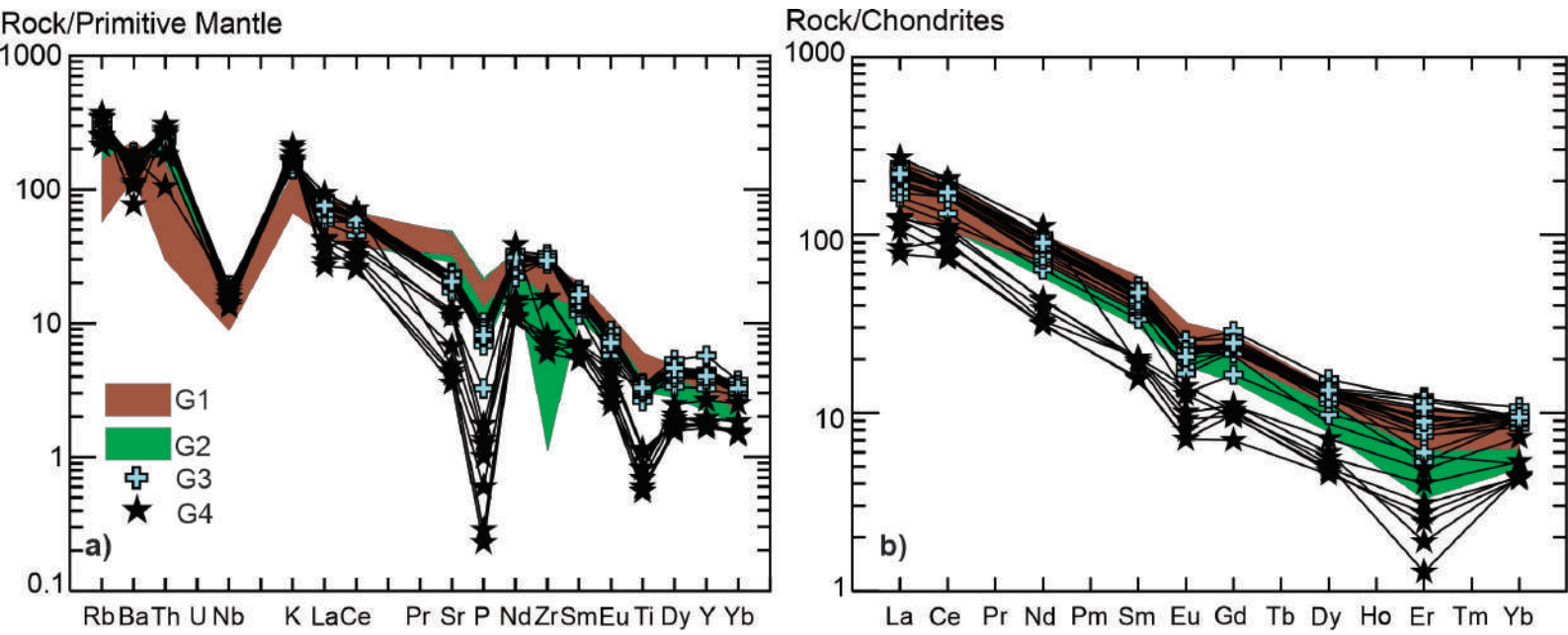
Rock/Primitive Mantle
1000
100
10
1
0.1
G1
G2
G3
G4
a)
Rb Ba Th U Nb K La Ce Pr Sr P Nd Zr Sm Eu Ti Dy Y Yb
Rock/Chondrites
1000
100
10
1
b)
La Ce Pr Nd Pm Sm Eu Gd Tb Dy Ho Er Tm Yb

Fig. 6

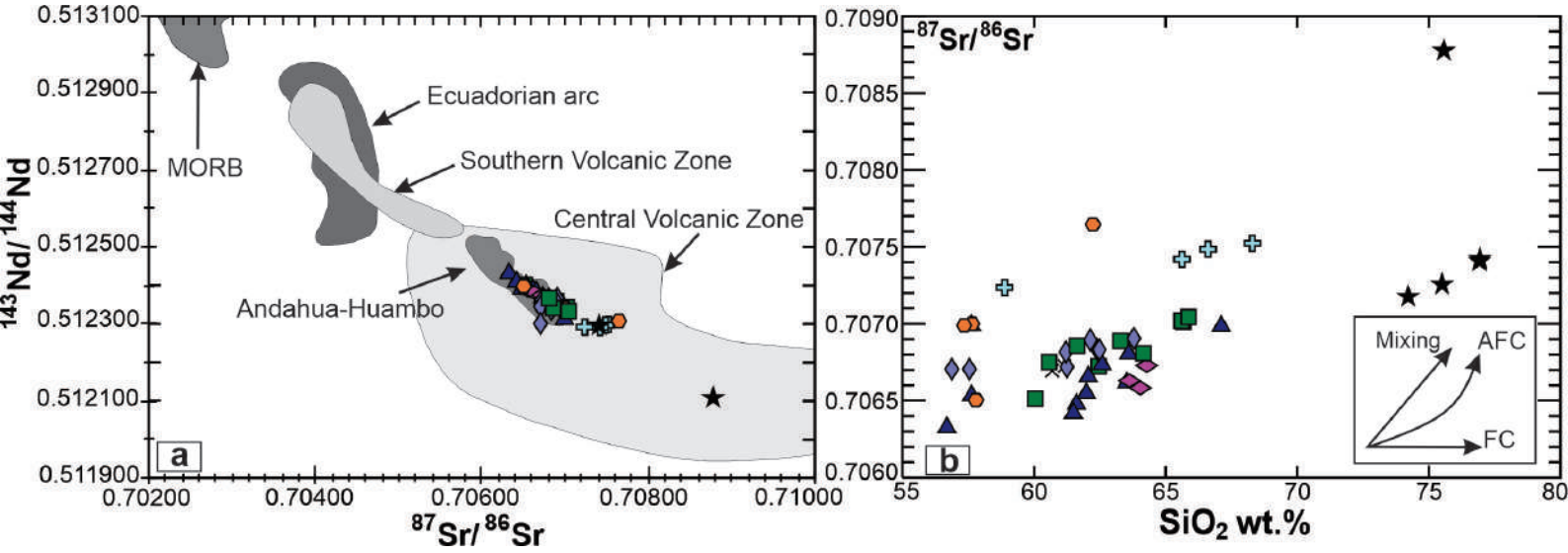
0.513100
0.512900
0.512700
0.512500
0.512300
0.512100
0.511900
143Nd/144Nd
MORB
Ecuadorian arc
Southern Volcanic Zone
Central Volcanic Zone
Andahua-Huambo
a
0.70200
0.70400
0.70600
0.70800
0.71000
87Sr/86Sr
0.7090
0.7085
0.7080
0.7075
0.7070
0.7065
0.7060
87Sr/86Sr
b
Mixing
AFC
FC
55
60
65
70
75
80
SiO2 wt.%

Fig. 7

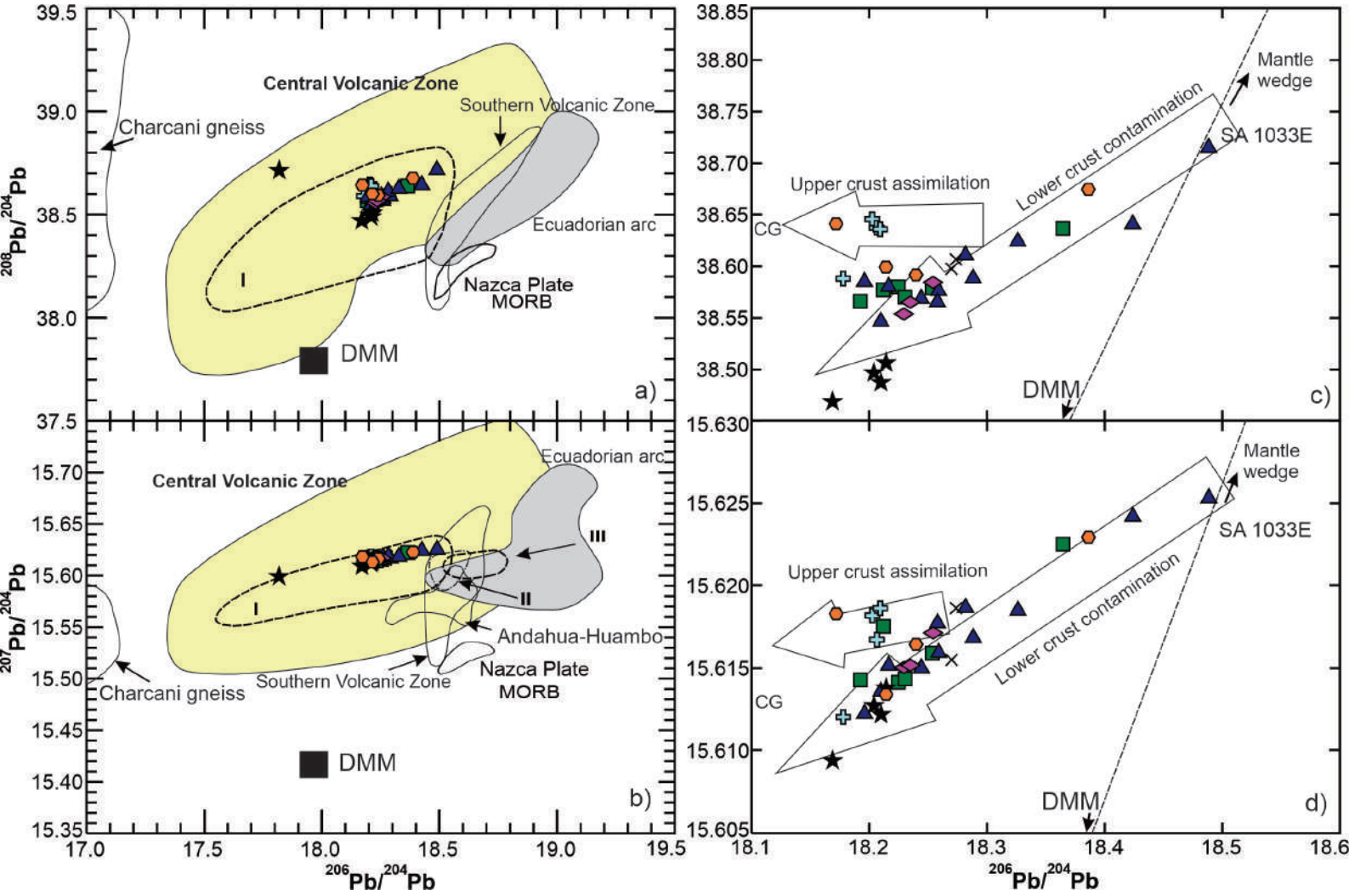
Central Volcanic Zone
Southern Volcanic Zone
Charcani gneiss
Ecuadorian arc
Nazca Plate
MORB
DMM
a)
Central Volcanic Zone
Ecuadorian arc
III
II
I
Andahua-Huambo
Southern Volcanic Zone
Nazca Plate
MORB
Charcani gneiss
DMM
b)
$^{208}Pb/^{204}Pb$
$^{207}Pb/^{204}Pb$
$^{206}Pb/^{204}Pb$
Mantle
wedge
SA 1033E
Upper crust assimilation
Lower crust contamination
CG
DMM
c)
Mantle
wedge
SA 1033E
Upper crust assimilation
Lower crust contamination
CG
DMM
d)
$^{206}Pb/^{204}Pb$

Fig. 8

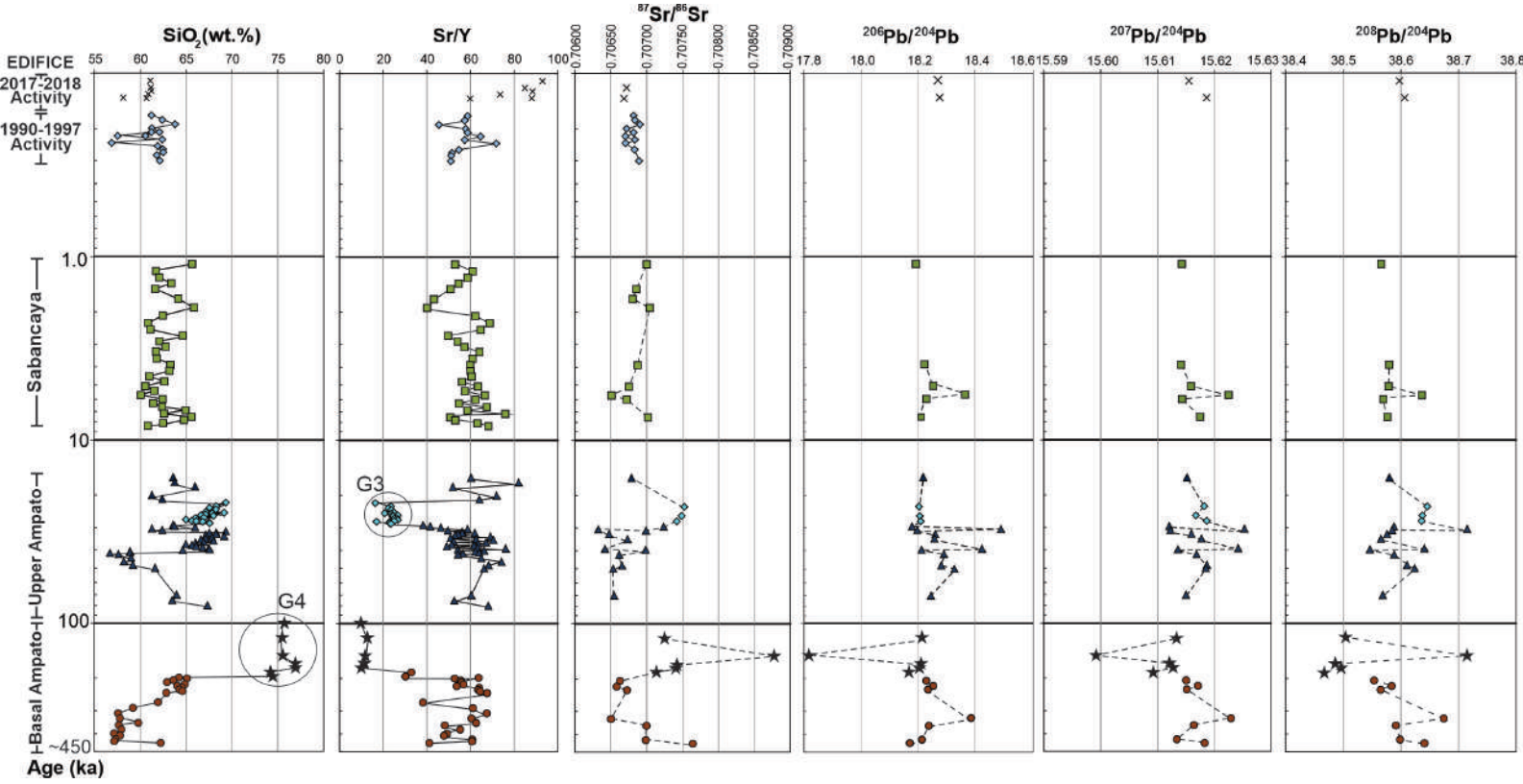
EDIFICE
2017-2018 Activity
1990-1997 Activity
SiO2(wt.%)
Sr/Y
87Sr/86Sr
206Pb/204Pb
207Pb/204Pb
208Pb/204Pb
Sabancaya
Upper Ampato
Basal Ampato
G3
G4
1.0
10
100
~450
Age (ka)

Fig. 9

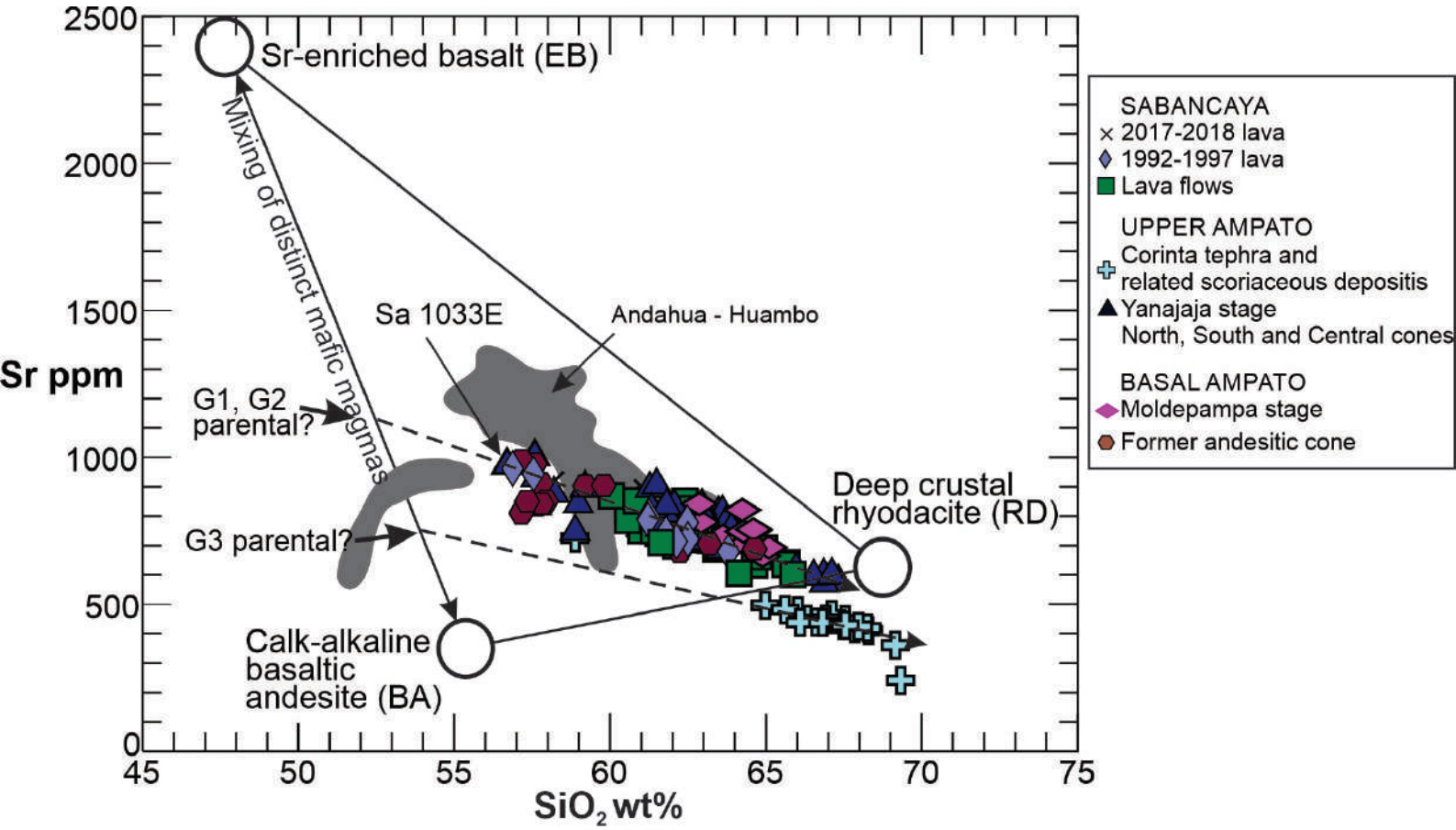
Sr-enriched basalt (EB)
Mixing of distinct mafic magmas
Sa 1033E
Andahua - Huambo
G1, G2 parental?
G3 parental?
Deep crustal rhyodacite (RD)
Calk-alkaline basaltic andesite (BA)
Sr ppm
SiO2 wt%
2500
2000
1500
1000
500
0
45
50
55
60
65
70
75
SABANCAYA
2017-2018 lava
1992-1997 lava
Lava flows
UPPER AMPATO
Corinta tephra and related scoriaceous depositis
Yanajaja stage
North, South and Central cones
BASAL AMPATO
Moldepampa stage
Former andesitic cone

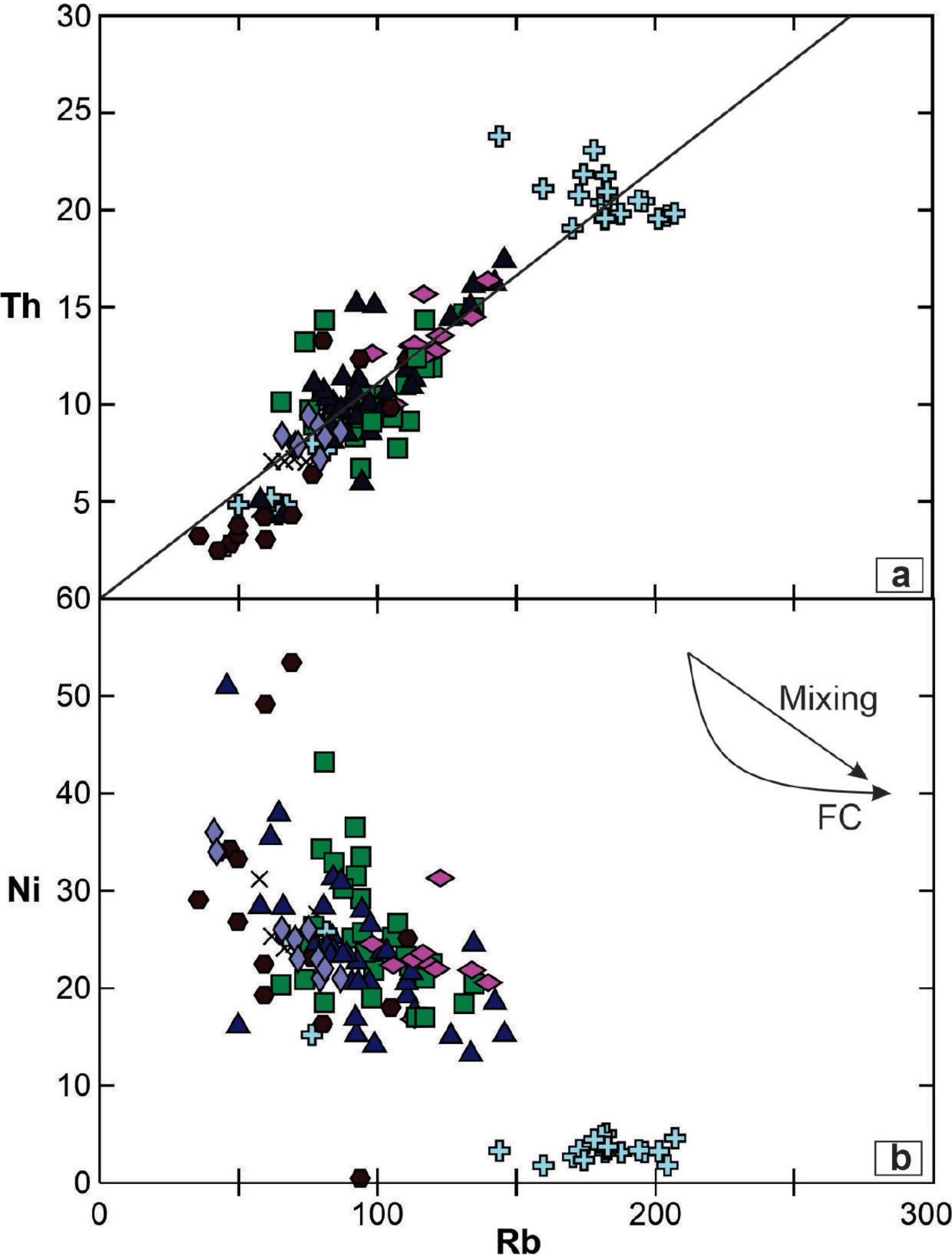

Fig. 10

Fig. 11

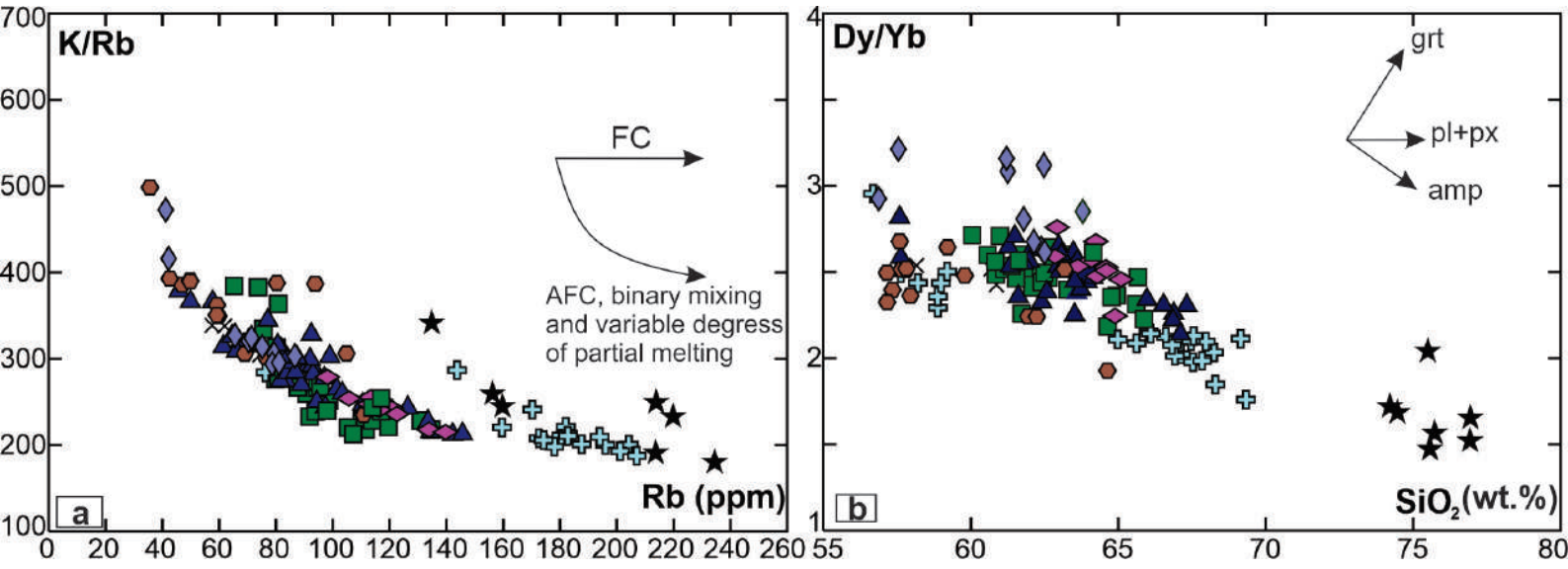
K/Rb
FC
AFC, binary mixing
and variable degress
of partial melting
Rb (ppm)
a
Dy/Yb
grt
pl+px
amp
SiO2(wt.%)
b

Fig. 12

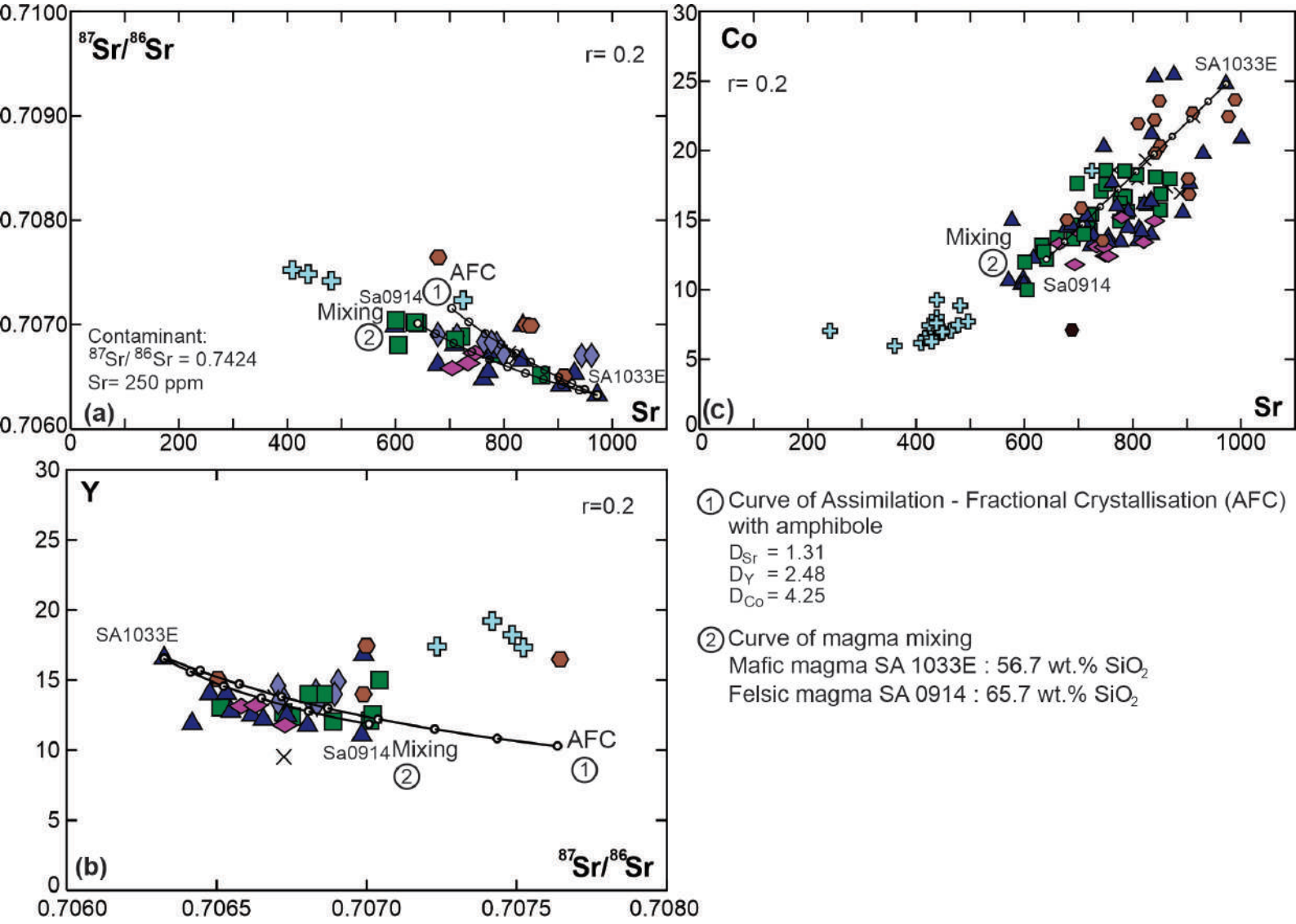

① Curve of Assimilation - Fractional Crystallisation (AFC) with amphibole

D_{Sr} = 1.31
D_Y = 2.48
D_{Co} = 4.25

② Curve of magma mixing

Mafic magma SA 1033E : 56.7 wt.% SiO_2
Felsic magma SA 0914 : 65.7 wt.% SiO_2

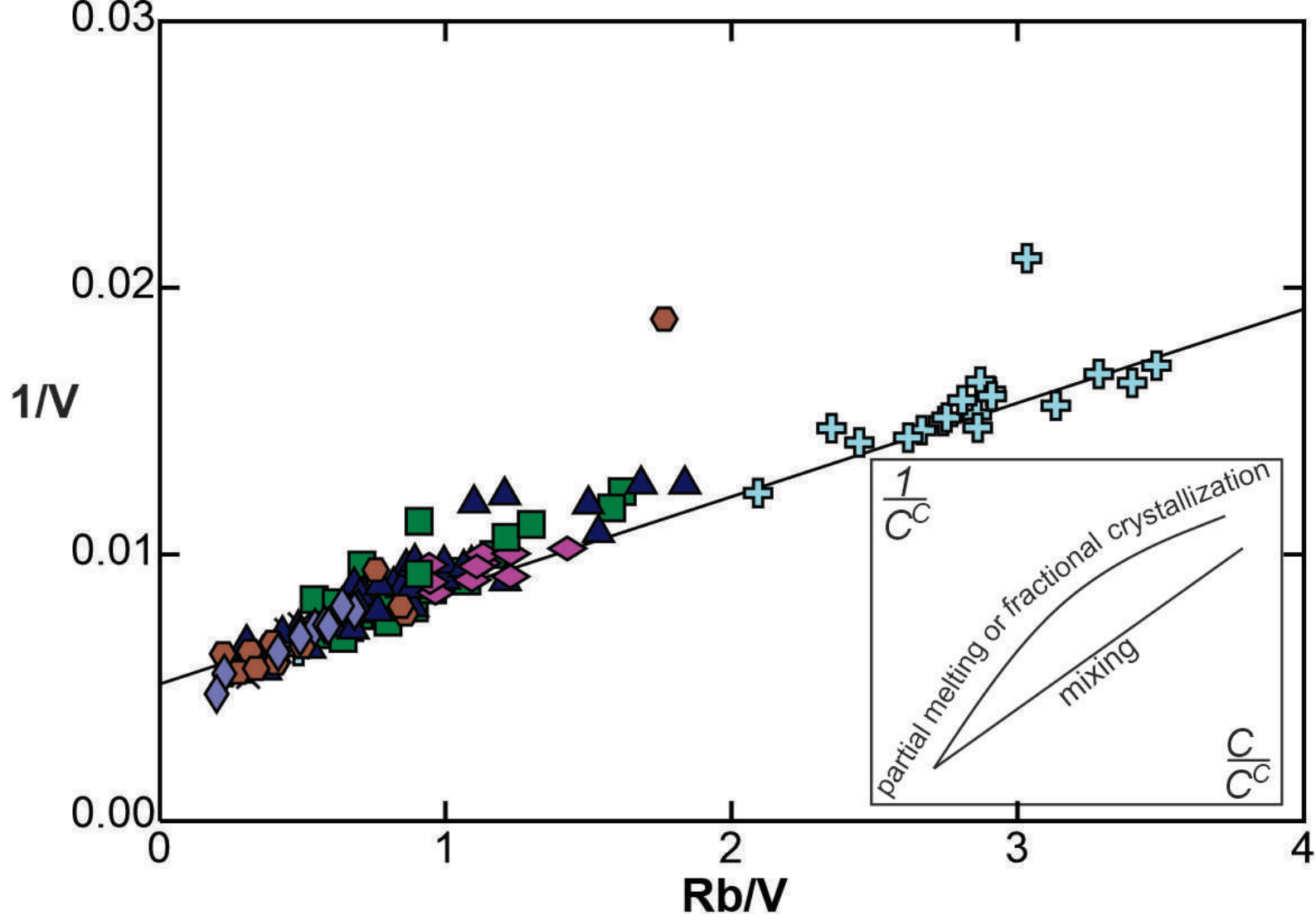
0.03
0.02
0.01
0.00
1/V
0
1
2
3
4
Rb/V
1/C_C
partial melting or fractional crystallization
mixing
C/C_C

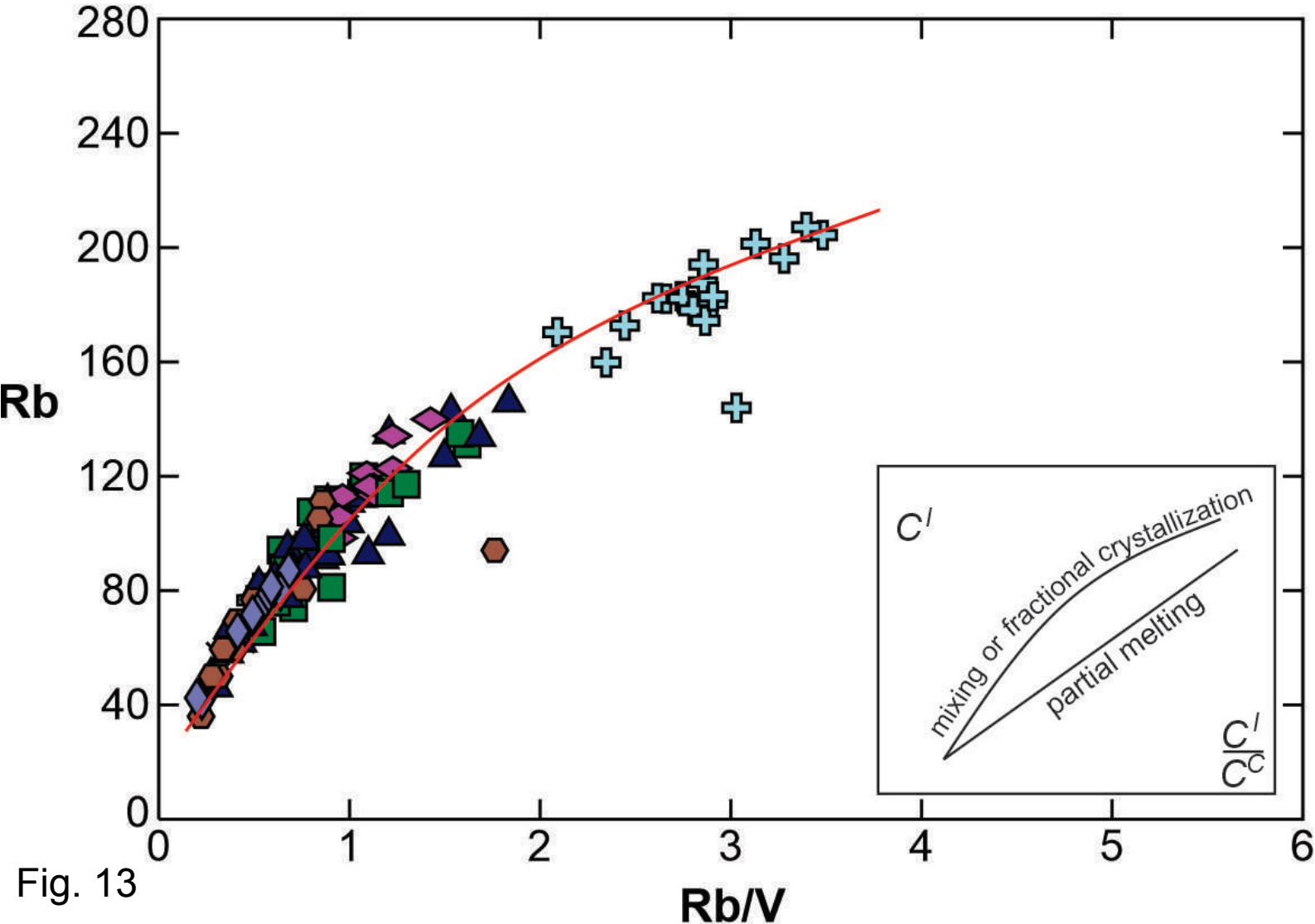
280
240
200
160
120
80
40
0
Rb
0
1
2
3
4
5
6
Rb/V
C'
mixing or fractional crystallization
partial melting
C'/C_C

Fig. 13

Fig. 14

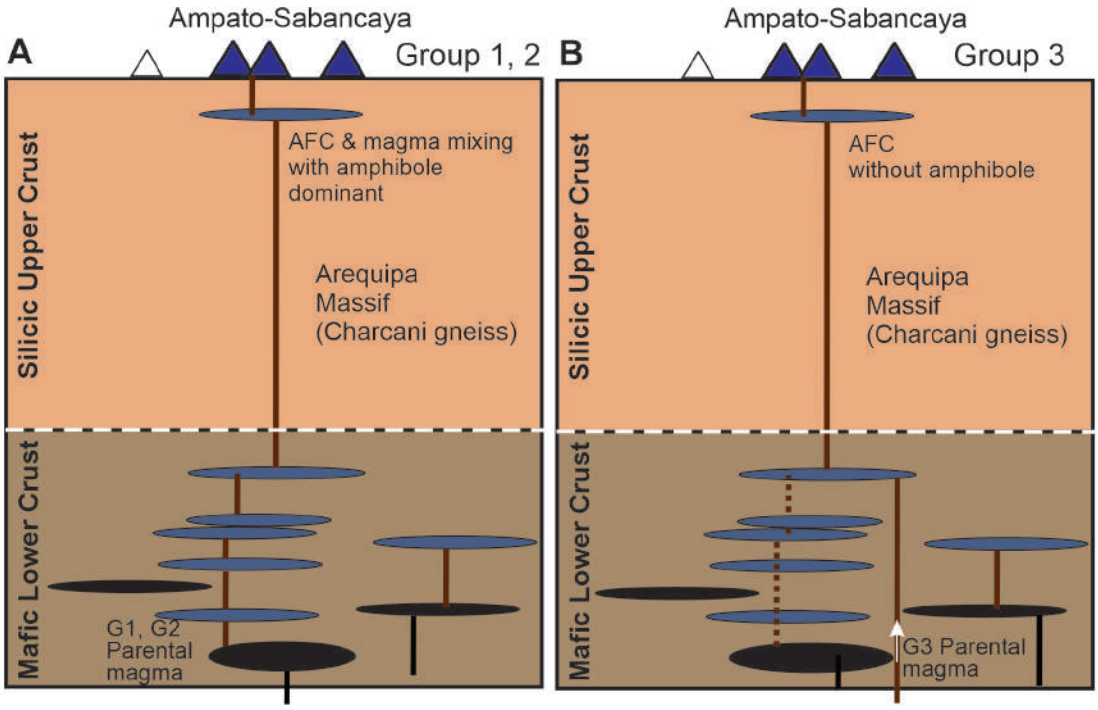
A
Ampato-Sabancaya
Group 1, 2
Silicic Upper Crust
AFC & magma mixing
with amphibole
dominant
Arequipa
Massif
(Charcani gneiss)
Mafic Lower Crust
G1, G2
Parental
magma
B
Ampato-Sabancaya
Group 3
Silicic Upper Crust
AFC
without amphibole
Arequipa
Massif
(Charcani gneiss)
Mafic Lower Crust
G3 Parental
magma

Table 1

Edifice	Ampato Basal						Ampato Upper							
Volcanic stage	Former andesitic cone		Moldepampa		Rhyolitic sequence		Yanajaja	North Cone		South Cone		Scoriaceus tephra		Corinta tephra-fall deposit
Group	G1	G2	G2	G2	G4	G4	G2	G2	G2	G2	G2	G1	G1	G3
Sample	SA-1161	SA-1010	SA-1105	SA-0927	SA-1184A	SA-1184D	SA-0931	SA-1175B	SA-1176	SA-1016A	SA-1016C	SA-1033E	SA-1119	SA-1139A
UTM-North	8,249,025	8,248,399	8,243,190	8,247,869	8,234,467	8,234,467	8,245,728	8,251,299	8,251,058	8,248,912	8,248,912	8,237,181	8,239,566	8,245,165
UTM-East	189,617	201,368	194,897	184,099	809,521	809,521	192,947	193,121	193,196	195,902	195,902	190,762	195,040	184,842
Rock type	Lava flow	Lava flow	Lava flow	Lava flow	Tephra-fall deposit	Tephra-fall deposit	Lava flow	Lava flow	Lava flow	Scoria flow	Scoria flow	Scoria	Scoria flow	Tephra-fall deposit
Major oxide (*wt.%*)														
SiO_2	56.43	60.53	63.4	61.94	70.62	71.71	62.00	57.04	61.48	59.6	65.4	53.4	57.7	61.8
TiO_2	1.10	0.83	0.82	0.91	0.16	0.11	0.83	1.23	0.96	1.07	0.63	1.22	1.02	0.71
Al_2O_3	16.92	16.51	15.7	16.03	12.47	11.97	15.54	16.84	16.25	16.3	15.0	17.1	17.9	16.6
Fe_2O_3	7.34	5.27	4.77	5.01	0.98	0.62	5.03	7.25	5.54	6.03	3.84	7.43	6.80	4.02
MnO	0.10	0.08	0.06	0.06	0.08	0.04	0.07	0.08	0.07	0.07	0.05	0.10	0.09	0.05
MgO	3.28	2.11	2.00	2.18	0.21	0.12	2.23	3.23	2.33	2.49	1.52	3.21	2.37	1.07
CaO	6.54	4.4	3.97	4.41	0.89	0.74	4.43	6.38	4.83	4.92	3.39	5.63	5.44	2.40
Na_2O	4.04	4.0	4.28	4.47	2.84	2.16	4.09	4.11	4.32	3.27	3.96	3.76	3.79	3.24
K_2O	2.30	3.7	3.33	3.19	5.18	5.75	3.10	2.44	2.93	2.76	3.51	1.97	2.56	4.07
P_2O_5	0.36	0.3	0.31	0.33	0.03	0.00	0.28	0.45	0.35	0.39	0.13	0.41	0.30	0.19
LOI	0.5	1.0	0.77	0.36	4.71	4.81	1.45	0.5	0.25	0.50	2.41	4.94	2.02	4.39
TOTAL	98.94	98.7	99.46	98.89	98.16	98.02	99.04	99.57	99.30	97.40	99.80	99.21	99.98	98.52
Trace elements (*ppm*)														
Rb	49.8	80.3	116	105.7	134.8	219.8	87.5	66.1	83.1	94.4	99.0	46	76	173
Sr	849.7	744.5	747	840.7	140.9	74.6	686.6	1001.2	833.6	905.1	599.1	972	725	481
Ba	920.1	1589.0	1129	1155.1	1173.8	530.8	1001.1	1009.9	1083.6	1008.9	920.8	1132	1026	1222
Sc	11.8	9.9	8.0	8.6	2.6	2.5	9.3	12.1	8.8	9.1	7.1	12.9	13.1	6.4
V	179.4	106.2	105	111.7	5.6	4.7	113.5	177.4	118.4	139.4	81.9	150	157	70
Cr	50.8	12.7	25.0	27.7	1.7	1.5	32.3	50.6	32.5	41.9	22.4	87.7	33.0	0.2
Co	23.6	13.5	13.1	15.0	0.3	0.3	14.6	20.9	16.4	17.6	10.4	24.8	18.6	8.9
Ni	33.3	16.3	23.6	22.4	1.2	0.9	23.4	28.3	23.3	28.0	14.2	51.3	15.2	3.4
Y	14.0	19.5	11.8	12.4	12.0	7.4	13.1	13.5	12.2	11.9	11.1	16.6	17.4	19.2
Zr	180.8	309.7	155	146.1	90.9	66.5	132.0	185.2	140.1	191.8	67.8	203	221	350
Nb	6.7	12.6	8.9	9.5	12.8	10.9	7.8	8.3	9.6	9.0	8.6	8.3	8.1	12.7
La	30.90	63.9	43	45.2	20.0	25.0	38.4	37.0	39.4	40.0	34.5	44	38	54
Ce	64.74	119.3	87	89.8	56.4	46.2	77.8	80.4	82.4	80.7	66.4	87	78	113
Nd	32.18	45.9	36	38.5	15.2	14.7	32.9	38.5	35.5	36.9	26.7	45	36	43
Sm	5.82	9.0	6.3	6.2	3.1	2.4	5.9	7.1	6.3	6.6	4.6	7.9	6.6	7.8
Eu	1.53	1.8	1.36	1.5	0.6	0.4	1.3	1.7	1.6	1.6	1.0	1.86	1.57	1.30
Gd	4.16	5.4	4.2	4.3	2.3	1.4	3.9	4.9	4.1	4.2	3.0	5.6	4.9	5.1
Dy	2.85	3.5	2.3	2.5	1.8	1.1	2.5	2.7	2.3	2.3	2.0	3.4	3.4	3.5
Er	1.35	1.6	0.9	1.0	0.8	0.5	1.2	1.2	0.9	0.9	0.7	1.5	1.6	1.3
Yb	1.19	1.6	0.94	0.9	1.2	0.7	1.0	1.0	0.9	0.8	0.9	1.16	1.47	1.68
Th	3.75	13.3	12.4	10.0	8.8	23.8	11.3	4.3	8.9	6.0	15.1	2.7	8.0	20.8
$^{87}Sr/^{86}Sr$	0.706989		0.706728		0.708776	0.707407	0.706548	0.707523	0.706656	0.706418	0.706989	0.706325	0.707235	0.707419

±2σ error	0.000007	0.000007	0.000007	0.000009	0.000006	0.000006	0.000006	0.000005	0.000006	0.000006	0.000008	0.000007
^{143}Nd/^{144}Nd	0.512342	0.512375	0.512108	0.512296	0.512394	0.512299	0.512383	0.512409	0.512343	0.512431	0.512292	0.512291
±2σ error	0.000022	0.000004	0.000007	0.000003	0.000005	0.000004	0.000004	0.000007	0.000005	0.000006	0.000005	0.000006
^{206}Pb_^{204}Pb	18.214174	18.234976	17.816697	18.203983	18.252469		18.281801	18.4239471	18.209770	18.4885391	18.177839	18.209318
±2σ error	0.0006	0.0004	0.0006	0.0007			0.0007	0.0006	0.0008	0.0006	0.0006	0.0007
^{207}Pb_^{204}Pb	15.613417	15.615174	15.599191	15.612741	15.61723		15.618665	15.6241859	15.613583	15.6253023	15.612039	15.618626
±2σ error	0.0006	0.0004	0.0006	0.0008			0.0006	0.0006	0.0007	0.0006	0.0005	0.0006
^{208}Pb_^{204}Pb	38.599166	38.565258	38.714973	38.496811	38.58141		38.610682	38.6407370	38.546364	38.7149278	38.588029	38.635910
±2σ error	0.0015	0.001	0.0018	0.002			0.0018	0.0015	0.002	0.0015	0.0015	0.0017

Sabancaya							
	Central Cone	Basal Sabancaya			Terminal Cone	2017-2018 Activity	
G3	G2	G2	G2	G2	G2	G2	G2
SA-1126	SA-1159	SA-0915	SA-0934	SA-0907	SA-0919	SA-1701	SA-1811
8,243,053	8,250,248	8,253,513	8,252,006	8,252,810	8,252,245	8252130	8252221
183,819	192,988	199,052	191,086	194,470	192,587	194412	194322
Bomb	Dome	Lava flow	Lava flow	Lava flow	Lava flow	Juvenile bomb	Juvenile bomb
65.2	62.5	64.9	59.65	61.1	62.5	60.2	61.18
0.60	0.86	0.73	1.07	0.95	0.87	1.00	0.95
14.9	15.597	15.5	16.55	16.3	15.8	16.2	16.44
3.29	5.02	4.17	6.23	5.63	5.15	6.2	5.89
0.05	0.07	0.06	0.08	0.07	0.07	0.076	0.08
0.88	2.25	1.96	2.81	2.51	2.26	2.74	2.66
2.41	4.36	3.77	5.45	5.04	4.54	5.46	5.48
3.53	4.131	4.12	4.43	4.20	4.14	4.34	4.35
4.52	3.17	3.50	2.68	2.85	3.03	2.63	2.67
0.16	0.30	0.23	0.38	0.30	0.27	0.337	0.33
2.78	1.03	0.52	0.24	0.15	0.25	0.09	0.10
98.36	99.25	99.48	99.59	99.16	98.84	99.22	100.13
196	110.7	80.9	94.0	77.1	110.2	78	70.0
419	709.0	635.7	868.9	783.9	687.4	823	808.7
1168	995.8	1051.5	1091.9	1033.2	992.7	998	1004.4
5.5	8.1	7.5	10.7	10.0	9.0	9.7	9.2
60	124.9	89.0	146.2	132.8	115.4	144	138.7
	29.0	21.2	39.5	30.6	33.0	43.1	38.1
6.6	14.9	12.7	18.0	16.7	14.7	19.3	18.0
3.2	19.2	18.5	29.2	26.3	23.2	27.6	24.5
17.7	12	12.5	13.1	12.9	12.6	13.8	9.5
320	109	67.8	167.4	130.7	106.8	148	139.4
11.9	7.9	8.5	8.1	7.3	8.2	7.7	7.4
53	39	39.4	38.5	35.9	35.5	34.4	35.1
106	79.6	79.8	76.3	75.7	76.3	70.4	74.3
41	34.6	32.2	35.7	33.1	32.0	32.3	33.2
6.7	6.0	5.7	6.3	6.1	5.6	5.8	5.7
1.29	1.5	1.2	1.6	1.5	1.3	1.27	1.3
4.4	4	3.8	4.4	4.3	3.9	4.5	4.4
3.2	2.4	2.3	2.6	2.3	2.4	2.5	2.2
1.5	1	1.2	1.1	1.0	1.1	0.6	1.1
1.57	1	1.0	1.0	1.0	0.9	0.98	0.9
20.4	11.8	14.3	6.7	8.9	11.0	7.2	7.2
	0.706803	0.707020	0.7065126			0.706695	0.706724

0.000005	0.000006	0.000007	0.000004	0.000006
0.512367	0.512343	0.5124024	0.512371	0.512365
0.000004	0.000005	0.000006	0.000003	0.000002
18.216489	18.211948	18.364697	18.273684	18.269987
	0.0008	0.0007		
15.615155	15.617531	15.622513	15.618642	15.615501
	0.0008	0.0006		
38.580263	38.577030	38.636606	38.606640	38.597552
	0.0022	0.0019		

Table 2

« Stage »	**Ampato Basal edifice**	**Ampato Upper edifice**	**Sabancaya**
Rock type		Lava flow	
Compositional range	Andesite (57.2 – 62.9 wt.% SiO_2)	Andesite (57.6 – 62.1 wt.% SiO_2)	Andesite (60.9 – 62.8 wt.% SiO_2)
Mineral assemblage	Pl+Cpx±Opx±Amp±Bt±Ol+Mag	Pl+Cpx±Opx±Amp±Bt+Mag	Pl+Cpx±Opx+Amp+Bt+Mag
Phenocrysts % vol.	20–60%	30–60%	30–55%
Texture	porphyritic and microlitic, sometimes with intersertal groundmass	porphyritic, sometimes with intersertal groundmass	porphyritic, sometimes with intersertal groundmass
Vesicularity (%)	4–8	4–8	4–8
Other characteristics	Some plagioclase phenocrysts with sieve-cored and/or sieve-ringed.	Some plagioclase phenocrysts with sieved cores and/or rings. Amphibole phenocryst sometimes have thin reaction rims composed of oxides. Some biotite phenocrysts have thin reaction rims composed of plagioclase and oxides.	Some plagioclase phenocrysts with sieved cores and/or rings. Amphibole phenocryst sometimes have altered rims or black-type of alteration (completely replaced by an aggregate of Fe-Ti oxides and pyroxene).
Compositional range	Dacite (63.6 – 65.1 wt.% SiO_2)	Dacite (63.1 – 67.3 wt.% SiO_2)	Dacite (63.2 – 65.7 wt.% SiO_2)
Mineral assemblage	Pl+Cpx±Opx+Amp+Bt+Mag	Pl+Cpx±Opx+Amp+Bt+Mag	Pl+Cpx±Opx+Amp+Bt+Mag
Phenocrysts % vol.	10–50%	10–50%	30–50%
Texture	porphyritic, sometimes with intersertal groundmass	porphyritic, sometimes with intersertal groundmass	porphyritic, sometimes with intersertal groundmass
Vesicularity (%)	2–6	0–4	4–8
Other characteristics	Some plagioclase phenocrysts are sieve-cored and/or sieve-ringed. Amphibole and biotite phenocrysts sometimes have altered rims or black-type of alteration (completely replaced by an aggregate of Fe-Ti oxides and pyroxene).	Some plagioclase phenocrysts are sieve-cored and/or sieve-ringed. Amphibole phenocryst sometimes have altered rims or black-type of alteration. Some biotite phenocrysts have thin reaction rims composed of plagioclase and Fe-Ti oxides.	Some plagioclase phenocrysts are sieve-cored and/or sieve-ringed. Amphibole phenocryst sometimes have altered rims or black-type of alteration (completely replaced by an aggregate of Fe-Ti oxides and pyroxene).
Rock type	Pumice or scoria belonging to pyroclastic-flow and tephra-fall deposits, or ballistic bombs		
Compositional range	---	Andesite (57.6 – 59.2 wt.% SiO_2)	Andesite (61.1 – 61.2 wt.% SiO_2)
Mineral assemblage		Pl+Cpx±Opx±Amp+Mag	Pl+Cpx+Opx+Amp+Bt+Mag
Phenocrysts % vol.		10–30%	40–50%
Texture		Vitroclastic	porphyritic with intersertal groundmass
Vesicularity (%)		40–60	4–10
Other characteristics		Some plagioclase phenocrysts are sieve-cored and/or sieve-ringed. Amphibole phenocryst sometimes have thin reaction rims composed of oxides.	Some plagioclase phenocrysts are sieve-cored and/or sieve-ringed. Biotite phenocryst have thin reaction rims composed of plagioclase and oxides.
Compositional range	Rhyolite (74.2 – 75.7 wt.% SiO_2), G4	Dacite (65.0 – 69.2 wt.% SiO_2), G2, G3	---
Mineral assemblage	Pl+Bt+Mag±Qz	Pl+Cpx±Opx+Amp+Bt+Mag	
Phenocrysts % vol.	10–20%	10–20%	
Texture	Vitroclastic	porphyritic, sometimes with intersertal groundmass; vitroclastic	
Vesicularity (%)	30–40	50–60	
Other characteristics	Biotite phenocryst sometimes has altered rims or black-type of alteration (completely replaced by an aggregate of Fe-Ti oxides and pyroxene).	Some plagioclase phenocrysts are sieve-cored and/or sieve-ringed. Amphibole phenocryst sometimes have altered rims.	

Table 3

« Stage »	Ampato Basal edifice	Ampato Upper edifice	Sabancaya
Compositional range[a]	Andesite to rhyolite (57.2 – 75.7 wt.% SiO_2)	Andesite to dacite (57.6 – 67.3 wt.% SiO_2)	Andesite to dacite (60.9 – 65.7 wt.% SiO_2)
Plagioclase % An pheno[b]	24 – 72	28 – 75	27 – 63
Type of zoning[b]	Normal (e.g., andesite SA-1162: $An_{70–63}$; rhyolite 1142D: $An_{33–22}$) and reverse zoning (e.g., andesite SA-1102: $An_{48–54}$)	Normal (e.g., andesite SA-1165: $An_{31–26}$; dacite SA-1014A: $An_{35–31}$) and reverse zoning (e.g., andesites SA-1165: $An_{34–48}$; dacite SA-1014B: $An_{29–46}$)	Normal (e.g., andesite SA-0904: $An_{34–29}$; dacite SA-1015: $An_{34–32}$) and reverse zoning (e.g., andesite SA-0911: $An_{33–60}$; dacites SA-0919: $An_{32–52}$)
Clinopyroxene compositional range[b]	$En_{39–52}$-$Fs_{12–19}$-$Wo_{34–46}$	$En_{39–46}$-$Fs_{13–19}$-$Wo_{40–46}$	$En_{39–48}$-$Fs_{11–17}$-$Wo_{41–48}$
Orthopyroxene % En[b]	65 – 76	62 – 75	41 – 76
Amphibole Mg#[c]	74 – 78	72 – 83	70 – 89
Biotite[b]	$1.14<Al^T<2.09$	$1.12<Al^T<1.17$	$1.12<Al^T<1.18$
Olivine % Fo[b]	68 – 77		80 – 82
Fe-Ti oxides[b]	Ulvospinel-magnetite and ilmenite series	Ulvospinel-magnetite and ilmenite series	Ulvospinel-magnetite and ilmenite series

[a]XRF analyses of bulk juvenile clasts on an anhydrous basis; *n* n°. of samples

[b]Range of microprobe analyses of phenocrysts

[c]Range of microprobe analyses; Mg# [where Mg# = 100*Mg/(Mg + Fe^T) in mol.%, and Fe^T is total iron as Fe^{2+}]

SEM 1

Plagioclase

Bend Antipathy — Sample: 6A-11-66

Analysis	8	9	10	11	12	13	14	15	16	17	18	19	20	21	22	23	24	25	26	27	28	29	30	31	32	33	34	35	36	37	38	39	40	41	42	43	44	45	46	47	48	49	50	51	52	53	54	55	56	57	58	59	60	61	62	63	64	65	66	67
	core																																																																			
SiO2 (wt%)	49.61	49.41	49.47	49.53	49.48	49.61	49.58	49.61	49.61	49.61	49.61	49.61	49.61	49.61	49.61	49.61	49.61	49.61	49.61	49.61	49.61	49.61	49.61	49.61	49.61	49.61	49.61	49.61	49.61	49.61	49.61	49.61	49.61	49.61	49.61	49.61	49.61	49.61	49.61	49.61	49.61	49.61	49.61	49.61	49.61	49.61	49.61	49.61	49.61	49.61	49.61	49.61	49.61	49.61	49.61	49.61
TiO2	0.02	0.03	0.03	0.00	0.03	0.00	0.00	0.03	0.03	0.02	0.14	0.02	0.00	0.02	0.01	0.03	0.08	0.03	0.04	0.03	0.00	0.04	0.00	0.02	0.00	0.02	0.00	0.02	0.00	0.02	0.00	0.02	0.00	0.02	0.00	0.02	0.00	0.02	0.00	0.02	0.00	0.02	0.00	0.02	0.00	0.02	0.00	0.02	0.00	0.02	0.00	0.02	0.00	0.02	0.00	0.02
Al2O3	30.88	31.60	28.38	27.90	29.01	28.12	28.18	28.07	28.60	28.15	30.49	29.53	30.02	29.47	29.62	29.66	30.80	30.07	29.58	32.62	30.52	27.14	28.32	27.22	27.93	29.68	29.48	27.29	24.21	24.99	27.19	24.83	26.52	23.61	25.99	26.23	25.51	24.13	23.91	24.84	24.99	23.84	23.66	19.89	19.61	22.62	19.58	19.65	24.75	23.38
Cr2O3	0.00	0.00	0.00	0.00	0.01	0.00	0.00	0.01	0.02	0.00	0.00	0.00	0.00	0.00	0.02	0.01	0.02	0.00	0.00	0.00	0.00	0.00	0.00	0.00	0.00	0.00	0.00	0.00	0.00	0.00	0.00	0.00	0.00	0.00	0.00	0.00	0.00	0.00	0.00	0.00	0.00	0.00	0.00	0.00	0.00	0.00	0.00	0.00	0.00	0.00	0.00	0.00	0.00	0.00	0.00	0.00
FeO*	0.64	0.64	0.71	0.67	0.42	0.62	0.63	0.66	0.76	0.73	0.75	0.76	1.14	0.64	0.79	0.65	0.66	0.69	0.67	0.71	1.10	1.35	1.04	0.96	1.07	1.13	1.05	0.99	0.33	0.51	0.32	0.52	0.28	0.45	0.22	0.27	0.29	0.25	0.28	0.19	0.23	0.15	0.09	0.09	0.18	0.14	0.09	0.16	0.21	0.21	0.20	0.20
MnO	0.00	0.00	0.00	0.00	0.00	0.00	0.00	0.00	0.00	0.00	0.00	0.00	0.00	0.00	0.00	0.00	0.00	0.00	0.00

MgO	14.45	15.17	14.92	15.41	15.06	15.14	15.40	14.91	15.02	15.25	15.42	14.84	14.84	15.16	14.92	15.08	14.24	14.83	14.83	14.75	15.22	15.03	14.43	14.54	14.99	14.76	14.85	14.85	14.67	14.86	15.46	14.04	14.26	15.44	15.18	14.91	15.03	15.30	14.52	15.43	14.66	15.19	14.40	14.04	14.80	14.98	14.29	14.86
CaO	0.00	0.00	0.05	0.01	0.02	0.03	0.00	0.00	0.00	0.03	0.00	0.00	0.00	0.02	0.02	0.00	0.02	0.01	0.00	0.02	0.02	0.05	0.01	0.00	0.01	0.00	0.03	0.02	0.02	0.01	0.01	0.05	0.00	0.05	0.05	0.03	0.03	0.01	0.00	0.04	0.02	0.00	0.01	0.00	0.00	0.00	0.05	0.00
Na2O	0.59	0.67	0.67	0.63	0.80	0.69	0.71	0.73	0.64	0.62	0.70	0.48	0.65	0.69	0.68	0.61	0.67	0.67	0.68	0.84	0.78	0.71	0.63	0.68	0.76	0.70	0.73	0.70	0.73	0.68	0.66	0.62	0.63	0.76	0.76	0.70	0.63	0.69	0.66	0.71	0.61	0.76	0.66	0.74	0.74	0.66	0.62	0.64
K2O	9.08	9.19	8.92	9.30	9.14	9.07	9.23	9.21	9.20	9.37	9.04	8.97	9.00	9.21	8.99	9.00	9.24	9.02	9.18	8.79	8.85	9.04	9.21	9.19	8.96	9.06	8.69	9.21	8.92	9.09	9.14	9.12	9.14	9.04	9.16	8.90	8.97	9.15	9.09	9.16	8.88	9.25	8.97	9.01	9.48	9.24	9.09	9.30
Total	95.02	94.91	95.62	97.31	95.62	96.17	95.95	95.69	95.75	95.88	95.30	94.48	95.63	96.44	95.16	95.18	95.81	95.39	95.58	95.50	95.71	95.36	95.02	95.49	95.52	94.11	95.27	95.17	94.64	94.81	95.77	94.85	95.29	95.73	95.39	94.70	95.17	95.42	95.56	95.90	95.32	96.04	94.68	93.67	95.87	94.91	94.73	95.91
Fe/(Fe+Mg)	0.42	0.42	0.41	0.41	0.41	0.41	0.40	0.41	0.41	0.40	0.41	0.43	0.42	0.41	0.41	0.41	0.43	0.41	0.42	0.43	0.41	0.41	0.43	0.43	0.42	0.42	0.42	0.42	0.41	0.41	0.40	0.45	0.44	0.40	0.41	0.41	0.41	0.40	0.44	0.40	0.43	0.40	0.44	0.44	0.42	0.41	0.43	0.42
Mg#	57.9	58.1	58.5	59.4	59.4	58.8	59.9	59.0	59.0	60.0	59.4	57.3	57.9	58.6	59.0	59.4	57.5	58.6	57.5	57.4	59.3	59.3	57.3	56.9	58.3	58.4	58.2	58.3	58.8	58.8	59.9	55.3	56.3	60.4	59.1	58.6	59.1	59.6	56.4	59.8	57.1	59.6	56.4	56.4	58.1	59.2	57.0	58.0

c: Phenocryst core , r: phenocryst rim

Olivine

	Basal Ampato																**Basal Sabancaya**			
Sample	**Sa-11-64**	**SA-11-62**								**Sa-1102**							**SA-09-06**			
Analyse	c	c	b	c	b	c	b	c	b	c	c	b	c	b	c	c	c	r	c	r
	21	46	47	62	63	85	86	94	95	109	110	111	112	116	122	128	80	81	108	109
SiO_2 (wt%)	37.03	39.40	39.18	39.01	38.64	38.71	38.77	38.81	38.38	38.22	38.10	37.46	37.83	37.05	51.63	37.60	40.07	39.66	39.60	39.80
TiO_2	0.03	0.01	0.05	0.04	0.02	0.00	0.01	0.00	0.05	0.06	0.04	0.14	0.06	0.09	0.99	0.05	0.00	0.04	0.05	0.00
Al_2O_3	0.00	0.02	0.02	0.04	0.00	0.02	0.04	0.01	0.03	0.02	0.01	0.05	0.03	0.05	2.10	0.00	0.00	0.02	0.02	0.01
Cr_2O_3		0.00	0.00	0.00	0.00	0.00	0.01	0.00	0.00	0.02	0.00	0.00	0.02	0.00	0.03	0.01	0.01	0.01	0.03	0.04
FeOt	27.32	21.09	18.78	21.70	21.69	21.26	21.35	21.75	21.45	23.04	24.11	24.92	24.50	27.43	8.47	24.86	16.90	18.52	18.85	18.87
MnO	0.50	0.27	0.28	0.34	0.32	0.31	0.32	0.34	0.35	0.53	0.50	0.50	0.50	0.61	0.30	0.60	0.29	0.23	0.24	0.25
MgO	34.58	40.14	41.76	39.76	39.51	39.81	39.60	39.78	39.60	37.20	36.63	35.56	36.44	32.66	16.25	36.08	42.80	42.20	41.98	41.71
CaO	0.15	0.09	0.16	0.16	0.10	0.15	0.14	0.11	0.15	0.19	0.18	0.19	0.15	0.21	19.11	0.14	0.14	0.15	0.13	0.11
Na_2O	0.00	0.00	0.01	0.01	0.02	0.02	0.00	0.00	0.00	0.05	0.00	0.00	0.01	0.02	0.51	0.02	0.01	0.00	0.02	0.03
K_2O	0.00	0.00	0.00	0.01	0.02	0.01	0.05	0.04	0.00	0.01	0.00	0.01	0.00	0.03	0.01	0.03	0.00	0.00	0.01	0.04
Total	99.7	101.0	100.2	101.1	100.3	100.3	100.3	100.8	100.0	99.3	99.6	98.8	99.5	98.2	99.4	99.4	100.2	100.8	100.9	100.9
Fo	69.3	77.2	79.9	76.6	76.5	76.9	76.8	76.5	76.7	74.2	73	71.8	72.6	68	77.4	72.1	81.9	80.2	79.9	79.8
Mg#	69.27	77.25	79.84	76.56	76.44	76.93	76.76	76.52	76.69	74.21	73.02	71.77	72.60	67.98	77.38	72.14	81.85	80.22	79.87	79.74

c: Phenocryst core , r: phenocryst rim

Magnetite

	Basal Ampato																									**Upper Ampato**																									
Sample	**SA-11-62**									**Sa-1102**					**SA-11-37**							**Sa-1142d**				**SA-09-30**		**SA-10-14A**	**SA-10-14B**										**SA-11-65**					**SA-10-33C**	**Sa 1119**			**SA-11-12A**			
Analyse	48	49	53	56	66	69	84	90	93	117	98	105	108	115	94 / 1 .	96 / 1 .	98 / 1 .	6 / 1 .	7 / 1 .	18 / 1 .	25 / 1 .	3	4	5	6	23	42	26	9	10	12	22	26	27	28	51	52	70	12 / 1 .	13 / 1 .	22 / 1 .	25 / 1 .	38 / 1 .	5	64 / 1 .	66 / 1 .	67 / 1 .	4	7	10	11
	c	c	c	c	c	c	c	c	c	c	c	c	c	c	c	c	c	c	c	c	c	c	c	c	c	c	c	c	c	c	c	c	c	c	c	c	c	c	c	c	c	c	c	c	c	c	c	c	c	c	c
SiO_2 (wt%)	0.09	0.35	0.11	0.08	0.14	0.09	0.18	0.10	0.07	0.07	0.08	0.18	0.08	0.05	0.14	0.09	0.06	0.21	0.10	0.09	0.08	0.01	0.04	0.03	0.01	0.08	0.05	0.02	0.04	0.03	0.05	0.06	0.08	0.06	0.06	0.05	0.08	0.15	0.06	0.00	0.08	0.10	0.08	0.14	0.19	0.14	0.14	0.11	0.09	0.14	0.09
TiO_2	8.67	8.81	9.00	9.21	9.11	9.20	9.14	9.07	8.80	10.69	10.10	11.55	11.99	10.89	8.27	9.11	7.79	9.08	8.09	14.62	11.24	4.51	4.37	4.45	4.55	8.50	8.88	4.59	5.59	3.39	2.70	1.33	4.67	4.02	6.90	15.07	10.11	2.93	5.69	3.96	6.18	5.20	7.94	11.25	8.00	8.76	9.14	3.69	9.03	8.49	8.76
Al_2O_3	5.20	4.48	4.88	4.87	4.90	4.84	4.75	4.89	4.88	0.70	1.66	1.01	1.67	1.63	2.29	2.32	2.04	2.62	2.18	2.11	2.92	0.96	0.97	0.94	0.97	1.97	2.70	0.67	2.08	0.58	2.07	1.46	1.10	1.21	1.02	0.66	1.03	0.79	2.21	1.72	2.64	2.11	1.94	3.19	4.77	4.14	4.43	1.86	2.26	2.36	2.30
Cr_2O_3	1.02	0.37	0.11	0.14	0.17	0.25	0.13	0.14	0.14	0.06	2.03	0.04	0.17	0.49	0.27	0.23	0.14	0.23	0.19	0.03	0.21	0.01	0.02	0.00	0.03	0.24	0.16	0.15	0.17	0.15	0.12	0.12	0.15	0.19	0.20	0.20	0.16	0.09	0.17	0.15	0.15	0.18	0.14	0.04	0.78	0.25	0.28	0.14	0.09	0.12	0.09
FeOt	74.53	74.30	76.28	75.71	75.81	75.44	72.80	75.34	75.72	80.87	78.72	79.17	77.97	78.68	80.85	80.12	81.64	78.79	81.43	73.50	76.61	86.44	86.53	86.15	85.79	80.47	79.97	85.56	81.90	85.86	83.92	85.66	85.30	85.08	78.94	79.76	77.87	87.20	83.07	85.78	81.88	84.07	82.07	75.57	75.77	77.01	75.61	79.66	78.29	79.05	79.41
MnO	0.27	0.26	0.28	0.28	0.27	0.31	0.27	0.29	0.22	0.42	0.42	0.57	0.47	0.47	0.37	0.43	0.33	0.41	0.39	0.48	0.46	1.03	1.19	1.06	1.08	0.44	0.34	0.36	0.40	0.30	0.44	0.46	0.32	0.46	0.38	0.50	0.18	0.32	0.37	0.28	0.37	0.40	0.36	0.46	0.24	0.28	0.31	0.40	0.43	0.49	0.42
MgO	4.55	4.09	4.45	4.52	4.62	4.53	4.82	4.50	4.47	0.86	1.66	1.08	1.97	1.46	1.79	1.58	1.80	1.69	1.84	2.27	2.61	0.58	0.59	0.63	0.67	1.75	2.15	0.87	2.68	2.42	2.31	2.59	1.66	1.04	1.91	0.76	0.48	1.96	1.54	1.02	1.94	1.69	1.42	3.85	4.52	3.05	3.40	2.12	2.20	2.31	2.16
CaO	0.03	0.05	0.00	0.00	0.02	0.03	0.12	0.03	0.02	0.16	0.00	0.22	0.16	0.06	0.04	0.03	0.01	0.04	0.02	0.05	0.06	0.00	0.00	0.13	0.08	0.02	0.01	0.01	0.02	0.01	0.05	0.06	0.10	0.29	0.03	0.04	0.23	0.08	0.02	0.10	0.00	0.02	0.05	0.05	0.20	0.20	0.06	0.26	0.18	0.30	0.04
Na2O	0.01	0.04	0.00	0.00	0.01	0.01	0.03	0.02	0.00	0.00	0.02	0.00	0.03	0.00	0.01	0.05	0.00	0.04	0.00	0.00	0.02	0.01	0.03	0.03	0.04	0.00	0.00	0.00	0.02	0.06	0.02	0.03	0.01	0.05	0.04	0.06	0.03	0.01	0.00	0.00	0.07	0.02	0.00	0.02	-0.02	-0.02	0.02	0.06	0.03	0.06	0.00
K2O	0.00	0.01	0.00	0.00	0.03	0.00	0.04	0.01	0.00	0.03	0.00	0.02	0.01	0.03	0.00	0.02	0.00	0.02	0.00	0.01	0.03	0.00	0.00	0.02	0.00	0.03	0.00	0.00	0.00	0.02	0.00	0.00	0.00	0.01	0.00	0.00	0.03	0.00	0.00	0.01	0.02	0.00	0.00	0.00	0.01	0.02	0.02	0.01	0.02	0.01	0.00
Total	94.36	92.76	95.10	94.80	95.07	94.69	92.27	94.40	94.32	93.85	94.69	93.83	94.53	93.76	94.03	93.97	93.81	93.13	94.25	93.16	94.24	93.56	93.74	93.43	93.22	93.50	94.26	92.24	92.89	92.80	91.67	91.76	93.40	92.42	89.47	97.10	90.21	93.53	93.12	93.01	93.32	93.78	94.01	94.58	94.47	93.85	93.40	88.32	92.62	93.33	93.27

c: Phenocryst core , r: phenocryst rim

																				Basal Sabancaya																								**Terminal cone**										**2017-2018 Activity**							
Sample	**SA-11-27C**				**SA-11-55**				**SA-11-59**	**SA-09-06**										**Sa-11-52**		**Sa0911**								**SA-10-15**							**SA-09-04**			**SA-09-10**				**SA-09-07**				**SA-09-19**						**Sa-1701**							
Analyse	9	12	17	22	51 / 1 .	52 / 1 .	59 / 1 .	69 / 1 .	39 / 1 .	46 / 1 .	49 / 1 .	54 / 1 .	55	56	62	69	92	100	113	73	74	15	16	54	55	56	57	76	68	11	32	34	40	56	59	62	17	34	56	101	16	44	48	60	62	85	99	16	18	32	33	40	52	19	20	25	26	41	42	63	64
	c	c	c	c	c	c	c	c	c	c	c	c	c	c	c	c	c	c	c	c	r	c	c	c	r	c	r	c	r	c	c	c	c	c	c	c	c	c	c	c	c	c	c	c	c	c	c	c	c	c	c	c	c	c	r	c	r	c	r	r	r
SiO_2 (wt%)	0.08	0.03	0.07	0.06	0.04	0.05	0.08	0.06	0.14	0.09	0.06	0.01	0.08	0.02	0.01	0.07	0.08	0.02	0.26	0.04	0.05	0.06	0.00	0.06	0.11	0.07	0.09	0.11	0.56	0.07	0.08	0.06	0.03	0.08	0.07	0.08	0.05	0.07	0.04	0.05	0.13	0.19	0.07	0.10	0.09	0.12	0.04	0.04	0.08	0.04	0.01	0.07	0.07	0.09	0.09	0.08	0.06	0.16	0.10	0.11	0.15
TiO_2	9.22	9.26	9.24	9.64	5.76	5.61	5.56	5.55	29.98	6.04	7.05	22.82	11.75	5.57	5.91	5.71	10.73	20.72	10.99	1.37	1.31	25.29	41.71	8.18	8.04	11.46	11.09	11.40	11.05	5.01	6.14	5.55	5.66	6.62	5.64	11.30	5.92	9.33	6.36	5.70	13.27	11.35	12.39	11.50	11.11	7.37	10.26	5.38	6.13	5.81	5.98	6.09	5.47	10.83	10.71	7.26	8.05	11.21	11.17	11.59	11.44
Al_2O_3	2.60	2.55	2.52	2.64	1.18	1.31	1.28	1.27	0.38	1.54	2.63	0.42	2.32	1.35	1.45	1.26	2.60	0.98	1.99	2.33	2.26	0.63	0.37	2.51	2.66	2.92	2.65	1.54	1.69	1.41	1.89	1.18	1.34	1.71	1.60	2.34	1.38	1.75	1.97	1.27	1.53	2.75	3.68	1.06	1.12	1.57	1.62	1.24	1.61	1.35	1.63	1.59	1.29	2.05	1.86	2.17	2.26	1.71	1.80	1.65	1.53
Cr_2O_3	0.04	0.05	0.01	0.04	0.18	0.19	0.14	0.18	0.07	0.18	0.16	0.05	0.00	0.20	0.23	0.20	0.16	0.07	0.01	0.22	0.19	0.17	0.00	0.16	0.16	0.14	0.05	0.24	0.22	0.17	0.17	0.14	0.20	0.10	0.12	0.07	0.14	0.09	0.16	0.12	0.02	0.06	0.19	0.02	0.02	0.14	0.15	0.19	0.16	0.20	0.12	0.14	0.16	0.15	0.15	0.17	0.18	0.05	0.00	0.01	0.05
FeOt	80.23	79.98	79.03	78.86	84.29	84.09	85.14	84.56	61.99	84.14	82.86	68.66	78.18	85.46	84.88	84.57	78.58	70.95	79.14	85.56	84.98	63.77	50.36	80.82	78.08	77.44	76.70	79.10	78.14	85.97	83.09	85.37	84.74	84.25	84.93	77.75	85.29	81.41	83.81	85.42	75.82	76.55	73.26	79.91	80.18	83.13	80.79	85.95	83.63	85.30	84.30	84.86	85.71	78.63	78.52	81.79	80.51	78.08	78.01	77.84	77.28
MnO	0.40	0.44	0.35	0.38	0.54	0.48	0.55	0.56	0.42	0.39	0.39	0.48	0.45	0.48	0.53	0.43	0.41	0.39	0.45	0.64	0.68	0.57	0.43	0.29	0.29	0.33	0.39	0.43	0.41	0.48	0.36	0.46	0.51	0.42	0.42	0.36	0.47	0.37	0.32	0.49	0.49	0.43	0.39	0.44	0.42	0.36	0.37	0.42	0.50	0.51	0.39	0.34	0.42	0.38	0.45	0.29	0.28	0.47	0.43	0.47	0.44
MgO	2.34	2.45	2.43	2.53	1.09	0.93	1.05	1.07	1.23	1.16	1.60	1.52	1.09	1.11	1.15	1.42	1.14	2.03	0.98	2.82	2.92	3.16	3.45	2.09	2.14	2.32	2.41	1.50	1.53	1.22	1.34	1.12	0.99	1.52	1.42	1.09	1.43	1.73	1.42	1.30	1.41	1.70	3.04	1.46	1.39	1.33	1.73	1.02	1.08	1.17	1.17	1.67	1.27	2.60	2.51	2.25	2.03	2.12	2.20	1.90	2.04
CaO	0.02	0.02	0.03	0.02	0.02	0.06	0.09	0.00	0.18	0.00	0.03	0.00	0.02	0.00	0.00	0.01	0.02	0.04	0.08	0.08	0.06	0.00	0.08	0.00	0.43	0.00	0.19	0.05	0.10	0.00	0.07	0.00	0.05	0.02	0.01	0.09	0.02	0.04	0.01	0.01	0.06	0.05	0.05	0.03	0.08	0.03	0.04	0.00	0.18	0.15	0.06	0.02	0.01	0.00	0.04	0.00	0.07	0.06	0.04	0.02	0.11
Na2O	0.00	0.00	0.03	0.00	0.08	0.00	0.03	0.00	0.04	0.00	0.00	0.03	0.00	0.00	0.00	0.00	0.00	0.00	0.03	0.00	0.00	0.00	0.00	0.02	0.04	0.00	0.01	0.00	0.02	0.00	0.00	0.01	0.00	0.00	0.00	0.00	0.04	0.00	0.02	0.00	0.00	0.01	0.02	0.00	0.01	0.00	0.00	0.02	0.01	0.00	0.00	0.00	0.00	0.00	0.00	0.00	0.00	0.05	0.00	0.00	0.00
K2O	0.00	0.00	0.00	0.00	0.00	0.01	0.00	0.01	0.04	0.02	0.00	0.00	0.02	0.00	0.03	0.00	0.00	0.01	0.02	0.00	0.00	0.00	0.00	0.00	0.01	0.01	0.02	0.03	0.03	0.00	0.00	0.00	0.00	0.00	0.04	0.04	0.01	0.02	0.02	0.01	0.06	0.04	0.01	0.03	0.00	0.00	0.00	0.00	0.03	0.00	0.01	0.04	0.06	0.02	0.03	0.00	0.00	0.00	0.01	0.02	0.04
Total	94.93	94.78	93.71	94.17	93.18	92.73	93.92	93.26	94.47	93.54	94.78	93.98	93.90	94.19	94.19	93.68	93.72	95.21	93.95	93.07	92.44	93.65	96.40	94.14	91.97	94.69	93.60	94.41	93.76	94.33	93.14	93.89	93.52	94.71	94.25	93.11	94.74	94.80	94.13	94.36	92.77	93.14	93.11	94.56	94.42	94.06	95.00	94.27	93.43	94.53	93.66	94.83	94.46	94.75	94.34	94.00	93.44	93.90	93.76	93.60	93.08

Ilmenite

	Basal Ampato																		**Basal Sabancaya**							**Terminal cone**
Sample	**SA-11-37**			**SA-11-76**		**SA-10-14A**		**SA-10-14B**						**SA-11-27C**		**SA-11-12A**	**SA-11-55**		**SA-09-06**	**SA-10-15**						**SA-09-19**
Analyse	95	1	5	27	28	24	25	8	11	13	23	29	69	26	27	9	50	76	96	21	28	57	58	60	61	19
	c	c	c	c	c	c	c	c	c	c	c	c	c	c	c	c	c	c	c	c	c	c	c	c	c	c
SiO_2	0.68	0.22	0.19	0.10	0.02	0.06	0.03	0.01	0.01	0.00	0.03	0.05	0.02	0.00	0.02	0.07	0.03	0.01	0.00	0.00	0.02	0.03	0.00	0.03	0.00	0.02
TiO_2	44.47	45.36	34.84	50.88	36.10	36.27	37.05	38.36	38.06	37.76	38.51	36.83	35.23	35.91	36.21	34.99	37.21	37.96	40.85	37.85	38.58	41.53	40.29	40.46	38.94	40.98
Al_2O_3	0.46	0.25	0.33	0.28	0.16	0.24	0.25	0.28	0.27	0.27	0.38	0.28	0.35	0.48	0.42	0.41	0.13	0.18	0.18	0.18	0.26	0.13	0.15	0.41	0.16	0.25
Cr_2O_3	0.05	0.06	0.04	0.07	0.04	0.01	0.06	0.08	0.02	0.04	0.00	0.04	0.04	0.00	0.02	0.03	0.01	0.00	0.04	0.06	0.00	0.06	0.04	0.00	0.04	0.01
FeOt	50.70	48.24	57.30	42.29	57.73	56.03	54.79	52.57	51.52	52.74	53.04	54.08	55.15	57.14	57.00	58.06	56.21	55.67	54.30	56.92	55.44	53.44	55.24	50.72	56.82	55.12
MnO	0.45	0.39	0.72	0.25	0.48	0.48	0.58	0.27	0.34	0.30	0.26	0.34	0.31	0.27	0.32	0.23	0.59	0.57	0.33	0.41	0.46	0.52	0.44	0.68	0.51	0.61
MgO	2.59	3.52	1.73	1.80	1.80	1.98	2.21	3.08	4.03	3.83	1.49	4.04	4.17	2.48	2.58	2.18	1.78	1.68	2.35	1.65	2.14	2.36	2.07	2.43	1.83	2.00
CaO	0.03	0.03	0.37	0.35	0.10	0.04	0.13	0.01	0.08	0.02	0.02	0.09	0.03	0.00	0.03	0.11	0.08	0.00	0.02	0.08	0.05	0.13	0.10	0.15	0.07	0.06
Na_2O	0.03	0.04	0.00	0.00	0.00	0.00	0.00	0.04	0.02	0.00	0.00	0.05	0.00	0.00	0.01	0.04	0.00	0.00	0.00	0.00	0.02	0.00	0.00	0.00	0.00	0.05
K_2O	0.01	0.02	0.02	0.01	0.00	0.02	0.01	0.01	0.03	0.01	0.03	0.01	0.00	0.01	0.02	0.01	0.00	0.00	0.02	0.03	0.05	0.04	0.01	0.05	0.00	0.02
Total	99.46	98.14	95.53	96.03	96.44	95.13	95.11	94.70	94.39	94.98	93.76	95.81	95.30	96.28	96.62	96.13	96.04	96.08	98.10	97.18	97.03	98.23	98.34	94.94	98.36	99.12

c: Phenocryst core , r: phenocryst rim

SEM 2

Edifice	Ampato Basal														
Volcanic stage	Former andesitic cone													Moldepampa	
Sample	SA-1161	SA-1162	SA-1164	SA-1102	SA-1103	SA-1124	SA-1117	SA-1122	SA-1166	SA-1010	SA-1108	SA-1109	SA-1032	SA-1101	SA-1105
Location	W flank, Ampato	W flank, Ampato	W flank, Ampato	SE flank Ampato	SE flank Ampato	South flank Ampato	South flank Ampato	South flank Ampato	W flank, Ampato	E flank, Ampato	South flank Ampato	South flank Ampato	SE flank Ampato	SE flank Ampato	South flank Ampato
UTM-North	8,249,025	8,249,025	8,249,025	8,244,360	8,244,656	8,240,139	8,242,674	8,240,517	8,248,393	8,248,399	8,240,399	8,240,220	8,239,778	8,244,253	8,243,190
UTM-East	189,617	189,617	189,617	195,403	195,706	189,809	192,847	189,949	188,439	201,368	194,111	193,453	195,234	195,369	194,897
Rock type	Lava flow	Lava flow	Lava flow	Lava flow	Lava flow	Lava flow	Lava flow	Lava flow	Lava flow	Lava flow	Lava flow	Lava flow	Lava flow	Lava flow	Lava flow
Major oxide (*wt.%*)															
SiO_2	56.43	56.19	60.28	57.3	58.0	57.3	59.5	57.8	58.52	60.53	56.61	57.51	57.15	64.1	63.4
TiO_2	1.10	1.12	0.86	1.21	1.17	1.05	1.07	1.16	1.04	0.83	1.09	1.10	1.24	0.79	0.82
Al_2O_3	16.92	17.25	15.76	16.7	16.6	17.8	17.1	17.5	17.30	16.51	17.69	18.17	17.86	15.8	15.7
Fe_2O_3	7.34	7.24	5.46	7.26	7.13	6.70	6.30	7.31	6.56	5.27	7.12	6.82	6.22	4.57	4.77
MnO	0.10	0.10	0.07	0.08	0.08	0.09	0.07	0.09	0.08	0.08	0.09	0.09	0.07	0.06	0.06
MgO	3.28	3.14	2.20	3.48	3.58	3.03	2.48	3.31	2.51	2.11	3.21	2.85	2.61	1.90	2.00
CaO	6.54	6.15	4.57	5.99	5.97	6.13	5.35	6.15	5.32	4.4	6.6	6.0	5.4	3.91	3.97
Na_2O	4.04	4.22	3.61	4.52	4.48	4.19	4.48	4.39	4.57	4.0	4.3	4.5	4.4	4.39	4.28
K_2O	2.30	2.46	3.74	2.50	2.60	2.32	2.76	2.18	2.56	3.7	2.0	2.1	2.4	3.46	3.33
P_2O_5	0.36	0.42	0.28	0.45	0.44	0.34	0.38	0.38	0.38	0.3	0.3	0.4	0.4	0.30	0.31
LOI	0.5	1.0	1.8	0.21	-0.03	0.79	0.09	0.06	0.05	1.0	0.3	0.4	1.5	0.44	0.77
TOTAL	98.94	99.30	98.65	99.78	100.02	99.72	99.52	100.25	98.90	98.7	99.3	99.9	99.3	99.76	99.46
Trace elements (*ppm*)															
Rb	49.8	59.2	104.8	60	61	50	77	47	59.3	80.3	42.6	35.7	54.9	113	116
Sr	849.7	988.9	679.2	977	917	851	904	840	902.7	744.5	810.0	841.4	927.2	750	747
Ba	920.1	1147.7	1014.5	1138	1122	1019	1164	1041	1139.2	1589.0	835.8	957.8	1046.1	1084	1129
Sc	11.8	12.8	9.8	13.2	13.3	12.5	11.1	13.3	10.5	9.9	15.0	12.0	11.9	7.7	8.0
V	179.4	174.9	124.2	170	169	157	153	178	149.5	106.2	182.6	159.7	175.7	100	105
Cr	50.8	18.8	19.0	93.7	97.7	30.0	22.5	45.8	14.9	12.7	43.2	33.6	73.7	23.7	25.0
Co	23.6	23.6	15.0	22.5	21.7	20.3	16.9	22.2	18.0	13.5	21.9	19.8	18.6	12.4	13.1
Ni	33.3	22.5	18.0	49.1	50.8	26.8	23.1	34.3	19.3	16.3	33.9	29.1	36.6	16.8	23.6
Y	14.0	16.3	16.5	14.5	14.6	15.4	14.4	17.4	14.8	19.5	16.5	17.6	18.4	11.7	11.8
Zr	180.8	216.6	213.5	222	233	204	226	197	223.5	309.7	177.9	198.1	214.7	142	155
Nb	6.7	8.1	9.6	8.8	8.9	6.9	8.5	7.0	8.5	12.6	6.2	7.1	12.5	8.7	8.9
La	30.90	41.1	40.9	45	44	37	42	38	40.5	63.9	35.9	39.4	19.9	43	43
Ce	64.74	86.0	84.8	90	90	74	85	73	85.6	119.3	68.6	85.7	39.0	87	87
Nd	32.18	39.1	35.6	41	42	35	39	38	36.8	45.9	36.7	46.5	13.6	35	36
Sm	5.82	6.8	6.5	7.3	7.6	6.2	6.5	6.6	6.7	9.0	6.1	6.7	9.0	6.0	6.3
Eu	1.53	1.8	1.4	1.79	1.78	1.69	1.52	1.79	1.7	1.8	1.7	1.7	2.4	1.29	1.36
Gd	4.16	4.8	4.4	5.0	4.7	4.6	4.6	4.9	4.5	5.4	4.9	5.3	6.2	3.8	4.2
Dy	2.85	3.2	3.0	2.8	2.9	2.9	2.8	3.2	2.9	3.5	3.1	3.2	3.6	2.3	2.3
Er	1.35	1.5	1.7	1.1	1.2	1.1	1.1	1.4	1.3	1.6	1.4	1.5	1.5	0.5	0.9
Yb	1.19	1.4	1.4	1.06	1.10	1.21	1.13	1.27	1.1	1.6	1.3	1.3	1.3	0.93	0.94

Th	3.75	4.2	9.8	3.0	4.2	3.3	6.4	2.8	4.3	13.3	2.5	3.2	4.2	13.1	12.4
$^{87}Sr/^{86}Sr$	0.706989		0.707645		0.706504			0.706999							0.706728
±2σ error	0.000007		0.000009		0.000008			0.000006							0.000007
$^{143}Nd/^{144}Nd$	0.512342		0.512308		0.512398			0.512341							0.512375
±2σ error	0.000022		0.000008		0.000005			0.000004							0.000004
$^{206}Pb\_^{204}Pb$	18.214174		18.171811		18.386253			18.239666							18.234976
±2σ error	0.0006		0.0007		0.001			0.0008							0.0004
$^{207}Pb\_^{204}Pb$	15.613417		15.618304		15.622931			15.616444							15.615174
±2σ error	0.0006		0.0006		0.0008			0.0007							0.0004
$^{208}Pb\_^{204}Pb$	38.599166		38.641206		38.674637			38.591577							38.565258
±2σ error	0.0015		0.002		0.002			0.0021							0.001

															Ampato Upper	
							Riolitic sequence								Yanajaja	
SA-1114	SA-1115	SA-1137	SA-1138	SA-1106	SA-0927	SA-1130	SA-1142A	SA-1142D	SA-1184C	SA-1186A	SA-1186B	SA-1184A	SA-1184D	SA-1023	SA-1128
W flank Ampato	South flank Ampato	SW flank, base Ampato	SW flank Ampato	South flank Ampato	W flank, Ampato	SW flank	Road to Cabanaconde	Road to Cabanacon de	Road Pedregal-Querque	Road Huambo-Querque	Road Huambo-Querque	Road Pedregal - Querque	Road Pedregal - Querque	East flank Ampato	S flank Ampato "Yanajaja"
8,241,698	8,243,491	8,246,350	8,247,137	8,243,432	8,247,869	8,245,701	8,244,160	8,244,160	8,234,467	8,248,692	8,248,692	8,234,467	8,234,467	8,249,155	8,244,402
184,106	192,405	187,567	188,471	194,252	184,099	188,519	182,345	182,345	809,521	808,904	808,904	809,521	809,521	194,225	189,043
Lava flow	Lava flow	Lava flow	Lava flow	Lava flow	Lava flow	Lava flow	Fallout tephra	Fallout tephra	Fallout tephra	Fallout tephra	Fallout tephra	Fallout tephra	Fallout tephra	Lava flow	Lava flow
62.1	64.2	61.9	62.8	63.3	61.94	63.0	70.74	71.12	74.7	72.3	71.6	70.62	71.71	61.51	61.1
0.97	0.80	0.85	0.88	0.77	0.91	0.91	0.14	0.16	0.12	0.24	0.23	0.16	0.11	1.01	0.93
16.0	15.5	16.0	15.5	15.8	16.03	15.9	13.58	12.65	12.3	13.6	13.4	12.47	11.97	16.32	16.1
5.22	4.54	4.83	4.95	4.52	5.01	5.07	0.80	1.30	0.71	1.32	1.26	0.98	0.62	5.55	5.42
0.06	0.05	0.06	0.06	0.06	0.06	0.06	0.04	0.04	0.043	0.051	0.051	0.08	0.04	0.07	0.07
2.28	1.83	2.00	1.99	1.90	2.18	1.98	0.14	0.22	0.13	0.31	0.27	0.21	0.12	2.47	2.66
4.10	3.72	3.84	3.91	3.84	4.41	4.06	0.59	0.69	0.79	1.39	1.28	0.89	0.74	5.01	4.81
4.27	4.12	4.01	4.19	4.10	4.47	3.29	2.62	3.17	2.09	3.41	3.47	2.84	2.16	4.39	4.18
3.32	3.57	3.45	3.44	3.41	3.19	3.47	4.76	4.36	6.24	4.75	4.53	5.18	5.75	2.85	2.93
0.36	0.28	0.30	0.32	0.29	0.33	0.36	0.01	0.02	0.006	0.037	0.028	0.03	0.00	0.34	0.32
0.86	0.64	0.74	0.26	1.01	0.36	0.03	5.3	4.2	4.74	5.26	5.30	4.71	4.81	0.17	1.22
99.58	99.30	98.02	98.28	99.01	98.89	98.16	98.75	97.92	101.79	102.72	101.45	98.16	98.02	99.69	99.71
113	140	117	134	123	105.7	121	234.5	231.4	214	156	160	134.8	219.8	97.4	87
780	693	734	704	755	840.7	820	86.9	106.1	92	263	237	140.9	74.6	834.8	771
1048	1020	1065	983	1073	1155.1	1112	791.6	1086.2	747	1190	1167	1173.8	530.8	1047.0	977
8.7	7.5	7.8	7.5	7.8	8.6	7.7	3.0	3.0	2.6	2.6	2.4	2.6	2.5	9.09	10.6
117	98	103	109	100	111.7	111	5.0	8.9	4.8	12	10	5.6	4.7	127.45	125
42.6	34.3	39.7	39.8	22.7	27.7	42.8			0.9	1.3	1.7	1.7	1.5	38.94	46.1
15.2	11.8	13.1	14.1	12.4	15.0	13.4	0.8	1.7	0.0	0.4	3.9	0.3	0.3	16.35	16.0
22.9	20.6	22.8	21.8	31.3	22.4	22.0	1.4	3.7	0.0	0.0	0.0	1.2	0.9	26.49	30.9
14.0	13.1	13.2	13.1	11.7	12.4	12.9	8.8	10.0	8.0	8.0	7.8	12.0	7.4	12.24	12.8
155	146	152	143	147	146.1	186	79.3	84.7	70	174	170	90.9	66.5	136.09	133
9.5	9.3	9.4	9.3	8.7	9.5	10.0	12.0	12.0	9.9	9.9	9.4	12.8	10.9	12.75	7.8
51	45	46	44	43	45.2	49	19.9	24.2	29	29	29	20.0	25.0	36.48	38
101	92	95	89	86	89.8	99	39.0	52.2	54	67	63	56.4	46.2	76.33	79
45	38	40	39	35	38.5	42	13.6	17.7	18	20	20	15.2	14.7	34.62	35
7.5	6.1	6.6	6.7	6.0	6.2	6.9	2.4	3.3	3.0	3.1	2.9	3.1	2.4	5.99	6.1
1.63	1.32	1.38	1.38	1.32	1.5	1.54	0.4	0.6	0.53	0.81	0.73	0.6	0.4	1.46	1.53
5.0	4.2	4.3	4.5	4.3	4.3	4.4	2.0	2.4	2.0	2.1	1.9	2.3	1.4	4.17	4.2
2.9	2.5	2.7	2.6	2.3	2.5	2.6	1.4	1.6	1.2	1.3	1.2	1.8	1.1	2.28	2.6
1.0	0.7	1.0	1.2	0.9	1.0	1.0	0.7	0.6	0.4	0.2	0.5	0.8	0.5	1.05	1.0
1.05	1.04	1.06	1.02	0.90	0.9	0.97	0.9	0.9	0.72	0.75	0.73	1.2	0.7	0.90	1.00

13.0	16.4	15.7	14.5	13.5	10.0	12.7	25.9	21.3	22.8	15.1	15.3	8.8	23.8	8.54	9.7
		0.706630	0.706582					0.707254	0.707421	0.707176		0.708776	0.707407		0.706548
		0.000016	0.000007					0.000007	0.000007	0.000007		0.000007	0.000009		0.000006
		0.512382	0.512386									0.512108	0.512296		0.512394
		0.000004	0.000004									0.000007	0.000003		0.000005
		18.229431	18.254171					18.214337	18.209962	18.168753		17.8166975	18.2039835		18.244236
		0.0007	0.0008					0.0003	0.0003	0.0004		0.0006	0.0007		0.0005
		15.615043	15.617141					15.613802	15.612198	15.609403		15.5991906	15.6127407		15.6150
		0.0007	0.0007					0.0004	0.0003	0.0004		0.0006	0.0008		0.0005
		38.553807	38.584347					38.506368	38.487431	38.468839		38.7149734	38.4968113		38.5685
		0.0018	0.002					0.0011	0.0009	0.0013		0.0018	0.002		0.001

	North Cone				South Cone										
SA-0931	SA-1175A	SA-1175B	SA-1176	SA-1177	SA-1016A	SA-1016C	SA-1014A	SA-1014B	SA-0928	SA-1173	SA-0930	SA-1026A	SA-1026B	SA-1165	SA-1160
SE flank Ampato	N Flank Ampato	N Flank Ampato	N Flank Ampato	N Flank Ampato	SE flank Sabancaya	SE flank Sabancaya	SE flank Sabancaya	SE flank Sabancaya	SE flank Ampato	East flank Ampato	SE flank Ampato	East flank Ampato	East flank Ampato	W flank, Ampato	East flank Ampato
8,245,728	8,251,299	8,251,299	8,251,058	8,250,965	8,248,912	8,248,912	8,248,736	8,248,736	8,247,356	8,248,582	8,247,108	8,246,215	8,246,215	8,250,264	8,247,759
192,947	193,121	193,121	193,196	193,431	195,902	195,902	195,842	195,842	193,526	192,940	193,200	195,224	195,224	187,602	188,305
Lava flow	Lava flow	Lava flow	Lava flow	enclave co-magmatic	Scoria flow	Scoria flow	Juvenile block	Juvenile block	Lava flow	Lava flow	Lava flow	Juvenile block	Juvenile block	Lava flow	Lava flow
62.00	60.27	57.04	61.48	57.05	59.6	65.4	64.3	62.3	62.22	62.78	61.79	64.58	62.25	61.60	63.33
0.83	0.97	1.23	0.96	1.19	1.07	0.63	0.64	0.83	0.87	0.81	0.83	0.62	0.82	0.96	0.9
15.54	16.24	16.84	16.25	16.83	16.3	15.0	15.0	15.6	15.88	15.61	15.56	14.96	15.54	16.26	15.57
5.03	5.61	7.25	5.54	7.27	6.03	3.84	3.98	4.70	5.12	4.85	4.98	3.77	4.77	5.80	5.057
0.07	0.07	0.08	0.07	0.09	0.07	0.05	0.05	0.06	0.07	0.06	0.07	0.05	0.06	0.07	0.06
2.23	2.60	3.23	2.33	3.31	2.49	1.52	1.53	1.89	2.43	2.05	2.21	1.50	1.88	2.78	1.97
4.43	5.08	6.38	4.83	6.25	4.92	3.39	3.35	4.18	4.60	4.23	4.41	3.35	3.98	5.06	4.18
4.09	4.26	4.11	4.32	4.08	3.27	3.96	4.01	4.28	4.24	4.25	4.07	4.03	4.19	4.27	4.20
3.10	2.84	2.44	2.93	2.52	2.76	3.51	3.53	3.23	3.03	3.30	3.11	3.53	3.26	2.87	3.460
0.28	0.33	0.45	0.35	0.41	0.39	0.13	0.21	0.30	0.27	0.32	0.26	0.20	0.29	0.30	0.33
1.45	0.3	0.5	0.25	0.67	0.50	2.41	1.70	1.44	0.13	0.02	1.23	1.64	1.50	0.11	0.2
99.04	98.57	99.57	99.30	99.67	97.40	99.80	98.29	98.84	98.86	98.27	98.50	98.23	98.55	100.08	99.23
87.5	88.9	66.1	83.1	57.8	94.4	99.0	92.4	92.0	80.6	112.24	77.1	133.5	113.3	84.07	134.57
686.6	821.4	1001.2	833.6	930.1	905.1	599.1	593.7	755.0	714.8	755.71	678.1	598.0	722.3	762.27	727.46
1001.1	1036.3	1009.9	1083.6	980.0	1008.9	920.8	973.5	1112.6	972.4	1092.81	1004.9	974.4	1094.2	956.90	1013.10
9.3	10.1	12.1	8.8	12.4	9.1	7.1	6.8	7.6	9.79	8.57	9.25	6.32	7.64	10.88	7.58
113.5	128.6	177.4	118.4	159.6	139.4	81.9	84.0	103.1	117.95	105.43	113.22	79.24	103.75	137.75	111.29
32.3	49.3	50.6	32.5	44.1	41.9	22.4	23.4	22.3	38.69	37.43	34.19	23.26	27.51	44.92	42.08
14.6	16.1	20.9	16.4	19.8	17.6	10.4	10.4	13.8	15.29	13.42	14.48	10.79	13.15	17.69	13.90
23.4	23.4	28.3	23.3	28.4	28.0	14.2	15.2	16.9	28.31	21.57	24.08	13.19	17.60	31.31	24.53
13.1	12.6	13.5	12.2	14.0	11.9	11.1	12.1	11.9	12.63	11.81	12.49	11.64	11.74	14.02	14
132.0	129.0	185.2	140.1	163.4	191.8	67.8	78.6	142.2	128.48	145.34	134.01	74.91	131.48	139.42	142
7.8	8.2	8.3	9.6	7.1	9.0	8.6	8.0	8.6	7.75	9.23	8.01	11.27	11.15	7.69	9
38.4	38.1	37.0	39.4	35.0	40.0	34.5	41.2	41.8	36.13	44.16	37.03	38.14	41.13	37.25	45.1
77.8	80.1	80.4	82.4	76.5	80.7	66.4	82.6	83.9	72.57	90.06	73.97	78.06	84.89	76.23	91
32.9	34.9	38.5	35.5	35.7	36.9	26.7	32.3	35.4	31.80	36.76	31.97	30.35	34.67	34.06	39.2
5.9	6.5	7.1	6.3	6.7	6.6	4.6	5.8	6.1	5.60	6.08	5.38	5.49	6.07	6.19	6.7
1.3	1.5	1.7	1.6	1.6	1.6	1.0	1.2	1.5	1.27	1.44	1.25	1.22	1.43	1.57	1.5
3.9	4.0	4.9	4.1	4.6	4.2	3.0	3.5	3.9	3.86	3.97	3.74	3.49	3.95	4.25	4.4
2.5	2.5	2.7	2.3	2.7	2.3	2.0	2.2	2.2	2.37	2.23	2.26	2.07	2.27	2.58	3
1.2	1.2	1.2	0.9	1.1	0.9	0.7	1.0	1.1	1.15	0.73	1.00	0.95	0.97	1.04	1.2
1.0	1.0	1.0	0.9	1.0	0.8	0.9	1.0	0.9	0.95	0.89	1.01	0.93	0.92	1.09	1

11.3	8.5	4.3	8.9	5.0	6.0	15.1	15.2	10.6	10.66	10.91	11.04	15.01	11.27	9.84	16
0.7065485		0.707523	0.706656	0.706532	0.706418	0.706989				0.706477	0.706617			0.706477	
0.000006		0.000006	0.000006	0.000007	0.000005	0.000006				0.000007	0.000006			0.000007	
0.512394		0.512299	0.512383	0.512400	0.512409	0.512343				0.512391	0.512388			0.512391	
0.000005		0.000004	0.000004	0.000004	0.000007	0.000005				0.000005	0.000004			0.000005	
18.252469			18.2818010	18.32634	18.4239471	18.2097697					18.288371			18.2589901	
			0.0007	0.0006	0.0006	0.0008					0.0009			0.0004	
15.617225			15.6186655	15.618492	15.6241859	15.6135833					15.616835			15.6159368	
			0.0006	0.0006	0.0006	0.0007					0.0008			0.0005	
38.581405			38.6106823	38.624074	38.6407370	38.5463641					38.588260			38.5762494	
			0.0018	0.0015	0.0015	0.002					0.002			0.001	

								Scoriaceus tephra							**Corinta fallout**
SA-1144	SA-1024A	SA-1024B	SA-1156B	SA-1021	SA-1025	SA-1020A	SA-1020B	SA-1033C	SA-1033D	SA-1133B	SA-1134	SA-1131	SA-1033E	SA-1119	SA-1127A
South flank Ampato	East flank Ampato	East flank Ampato	W flank Ampato	East flank Ampato	East flank Ampato	East flank Ampato	East flank Ampato	Road Sallalli-Taya	Road Sallalli-Taya	Road Sallalli-Taya	Road Sallalli-Taya	W flank Ampato	S flank Ampato	South flank Ampato	Collpa, SW flank Ampato
8,239,566	8,247,589	8,247,589	8,248,533	8,248,490	8,246,378	8,248,490	8,248,490	8,237,095	8,237,180	8,233,726	8,232,315	8,241,471	8,237,181	8,239,566	8,242,318
195,040	194,478	194,478	187,545	194,022	195,049	194,022	194,022	190,769	190,761	185,941	185,904	186,112	190,762	195,040	183,658
Pumice	Lava flow	Lava flow	Juvenile block	Lava flow	Lava flow	Lava flow	Lava flow	Bomb juvenile	Fallout tephra	Fallout tephra	Scoria	Scoria flow	Scoria	Scoria flow	Fallout tephra
64.62	62.13	64.48	62.77	61.62	62.06	62.55	65.56	56.71	56.30	56.5	57.7	57.6	53.4	57.7	63.2
0.62	0.90	0.65	0.88	0.90	0.90	0.87	0.63	1.2	1.2	1.10	1.10	0.98	1.22	1.02	0.69
15.25	15.30	14.70	15.86	16.03	15.99	15.85	14.74	17.59	17.29	17.617	16.384	17.3	17.1	17.9	15.9
3.44	5.04	3.93	4.70	5.20	5.12	4.97	3.78	7.445	6.741	6.84	6.62	6.92	7.43	6.80	3.83
0.04	0.06	0.05	0.06	0.07	0.06	0.06	0.05	0.10	0.08	0.09	0.08	0.09	0.10	0.09	0.05
0.87	2.09	1.54	2.05	2.38	2.11	2.05	1.50	2.83	2.34	2.90	2.92	3.06	3.21	2.37	1.01
2.33	4.24	3.28	4.35	4.69	4.40	4.23	3.23	5.87	4.90	5.54	5.62	5.66	5.63	5.44	2.51
3.47	4.38	3.99	4.38	4.25	4.42	4.37	4.02	4.12	3.86	3.882	4.196	3.31	3.76	3.79	3.18
4.45	3.18	3.57	3.12	3.02	3.20	3.24	3.64	2.166	2.402	2.26	2.47	2.64	1.97	2.56	4.37
0.14	0.34	0.20	0.33	0.31	0.34	0.34	0.23	0.34	0.36	0.36	0.39	0.29	0.41	0.30	0.17
3.50	0.22	1.18	0.1	0.78	0.30	0.39	1.53	1.96	4.57	2.93	0.73	1.14	4.94	2.02	4.66
98.74	97.89	97.60	98.56	99.24	98.89	98.92	98.91	100.37	100.00	100.05	98.20	99.04	99.21	99.98	99.58
207	92.7	126.4	93.13	81.9	97.1	110.53	145.67	49.9	67.3	61.5	64.5	82	46	76	182
417	812.0	571.1	777.97	778.8	834.5	809.57	577.08	835.0	840.9	876.2	894.9	747	972	725	438
1100	1106.9	945.1	1060.94	1035.4	1130.0	1148.21	968.77	948.8	1165.7	1092.8	1069.7	958	1132	1026	1186
5.7	8.05	6.43	6.68	9.18	8.34	7.93	6.09	13.0	11.1	12.4	11.6	12.9	12.9	13.1	6.1
61	113.05	84.24	105.16	117.76	114.76	110.71	79.27	181.1	138.4	142.8	159.2	155	150	157	70
	30.11	24.86	27.65	33.42	30.34	29.39	24.20	7.5	24.8	57.5	61.0	33.0	87.7	33.0	1.3
6.5	14.39	10.66	13.44	15.39	13.97	13.50	14.96	21.2	25.3	25.4	31.9	20.3	24.8	18.6	9.3
4.6	22.67	15.04	20.57	24.20	20.60	20.55	15.23	16.4	25.4	35.8	38.2	25.8	51.3	15.2	5.1
17.6	11.52	10.93	12.2	12.46	12.43	11.70	11.33	16.8	14.9	15.6	14.4	16.1	16.6	17.4	18.2
324	144.14	66.61	114.8	117.24	147.50	143.3	67.9	207	238	229.7	222.2	217	203	221	342
12.8	12.18	7.90	8.0	9.05	10.79	9.1	8.1	7	8	8.27	7.67	7.7	8.3	8.1	12.6
44	41.99	33.38	35.33	37.85	45.37	42.8	40.4	33.8	42.7	41.96	42.18	37	44	38	49
96	86.74	73.67	73.04	75.11	93.27	86.10	78.58	72	89	85.94	82.21	74	87	78	109
35	36.03	26.63	31.21	33.40	38.62	36.16	31.80	35.8	39.0	38.94	39.17	34	45	36	41
6.3	5.96	4.67	5.26	5.68	6.43	6.24	5.43	6.7	6.8	6.94	6.81	5.7	7.9	6.6	7.1
1.2	1.54	1.09	1.34	1.35	1.58	1.39	1.25	1.6	1.8	1.64	1.68	1.50	1.86	1.57	1.22
4.4	4.12	3.05	3.89	3.89	4.12	4.00	3.66	5.0	4.6	5	5	4.6	5.6	4.9	4.9
3.1	2.24	2.00	2.47	2.20	2.38	2.36	2.25	3	3	3	3	3.2	3.4	3.4	3.3
1.3	1.06	0.95	0.92	1.02	0.98	0.98	0.75	1.5	1.3	1	1	1.3	1.5	1.6	1.5
1.55	0.87	0.88	1.03	0.92	0.94	0.90	0.98	1	1	1.2	1.2	1.34	1.16	1.47	1.55

19.8	9.31	14.43	11.29	10.29	10.03	12.23	17.40	5	5	5	4	7.6	2.7	8.0	21.8
		0.707419		0.706734				0.706990					0.706325	0.707235	0.707495
		0.000007		0.000006				0.000007					0.000006	0.000008	0.000006
		0.512291		0.512370				0.512312					0.512431	0.512292	0.512297
		0.000006		0.000006				0.000008					0.000006	0.000005	0.000004
				18.2579341				18.1959294					18.488539	18.1778390	18.206377
				0.0006				0.0005					0.0006	0.0006	0.0007
				15.61772504				15.6122403					15.625302	15.6120386	15.61673
				0.0004				0.0005					0.0006	0.0005	0.0007
				38.5653709				38.5849021					38.714928	38.5880291	38.637404
				0.002				0.001					0.0015	0.0015	0.002

											Central Cone				
SA-1127B	SA-1127C	SA-1127D	SA-1139C	SA-1139A	SA-1033B	SA-1033A	SA-1143	SA-1126	SA-1112A	SA-1112B	SA-0929	SA-1154	SA-1155	SA-1157	SA-1159
Collpa, SW flank Ampato	Collpa, SW flank Ampato	Collpa, SW flank Ampato	Collpa, SW Ampato	Collpa, SW flank Ampato	South flank Ampato	South flank Ampato	Road Sallalli-Taya	Qda. Chuyune	SW Ampato, Q. Vizcachane	SW Ampato, Q. Vizcachane	SE flank Ampato	East flank Ampato	East flank Ampato	East flank Ampato	East flank Ampato
8,242,318	8,242,318	8,242,318	8,245,165	8,245,165	8,237,068	8,237,067	8,245,596	8,243,053	8,243,120	8,243,120	8,249,119	8,249,484	8,249,870	8,249,948	8,250,248
183,658	183,658	183,658	184,842	184,842	190,779	190,778	185,315	183,819	184,012	184,012	194,027	193,676	193,443	193,215	192,988
Fallout tephra	Fallout tephra	Fallout tephra	Pumice	Fallout tephra	Fallout tephra	Fallout tephra	pumice	Bomb	Pumice	Scoria	Lava flow	Lava flow	Lava flow	Lava flow	Dome
64.2	62.8	61.4	62.92	61.8	64.1	63.0	63.93	65.2	65.8	64.5	61.65	60.79	64.52	62.8	62.5
0.63	0.67	0.66	0.65	0.71	0.67	0.63	0.65	0.60	0.60	0.64	0.93	0.9	0.7	0.88	0.86
15.1	15.3	15.4	16.19	16.6	15.1	15.3	15.54	14.9	15.0	15.3	16.01	16.96	14.93	15.856	15.597
3.45	3.62	3.61	3.56	4.02	3.61	3.44	3.45	3.29	3.24	3.54	5.38	5.217	4.228	4.70	5.02
0.05	0.05	0.05	0.05	0.05	0.05	0.05	0.05	0.05	0.04	0.08	0.07	0.07	0.06	0.06	0.07
0.91	0.99	1.28	0.91	1.07	0.92	0.93	0.94	0.88	0.82	0.94	2.36	2.49	1.90	2.05	2.25
2.40	2.56	2.62	2.34	2.40	2.43	2.35	2.48	2.41	2.30	2.47	4.74	5.14	3.57	4.35	4.36
3.20	3.29	3.31	3.31	3.24	3.21	3.16	3.55	3.53	3.64	3.53	4.34	4.51	4.06	4.379	4.131
4.33	4.40	4.51	4.06	4.07	4.64	4.33	4.45	4.52	4.75	4.33	3.00	2.738	3.555	3.12	3.17
0.17	0.17	0.18	0.16	0.19	0.17	0.16	0.18	0.16	0.16	0.16	0.31	0.33	0.27	0.33	0.30
4.27	4.68	5.47	4.00	4.39	4.47	4.63	3.70	2.78	2.88	2.81	0.42	0.4	0.5	0.06	1.03
98.68	98.49	98.46	98.15	98.52	99.29	98.06	98.93	98.36	99.26	98.25	99.20	99.56	98.29	98.56	99.25
181	183	182	174.3	173	194	183	201.2	196	204	188	84.1	83.6	142.3	90.8	110.7
425	449	478	437.7	481	429	427	447.0	419	410	447	791.6	892.8	616.8	778.0	709.0
1098	1089	1141	1163.1	1222	1109	1101	1152.8	1168	1137	1161	1104.9	1044.5	1059.5	1060.9	995.8
5.6	5.9	5.7	5.9	6.4	5.6	5.9	5.8	5.5	5.3	5.9	9.3	9.0	6.7	6.7	8.1
62	67	66	60.7	70	68	63	64.2	60	59	66	123.8	117.3	92.7	105.2	124.9
0.1	0.1			0.2	0.1	0.5				1.1	33.6	37.7	28.5	27.7	29.0
7.4	7.0	7.5	7.6	8.9	6.3	6.5	7.2	6.6	6.2	6.9	15.6	15.5	12.2	13.4	14.9
4.8	3.5	3.6	2.3	3.4	3.4	3.7	3.2	3.2	1.8	3.1	23.9	25.3	18.5	20.6	19.2
17.2	17.2	19.1	19.1	19.2	18.2	18.6	18.0	17.7	17.3	20.0	12.4	12	12	9.48	12
320	321	309	348.0	350	327	323	337.9	320	333	325	127.50	120	68	114.8	109
12.2	12.5	11.6	12.5	12.7	12.6	12.3	13.0	11.9	12.4	12.1	8.00	7	8	8.02	7.9
50	50	57	51.9	54	52	51	46.8	53	40	59	36.70	37.4	43.4	39.55	39
108	106	107	110.2	113	105	109	101.3	106	98	122	77.45	73	86	77.40	79.6
40	39	44	41.4	43	42	41	38.3	41	34	46	33.63	35.3	34.5	33.87	34.6
6.6	6.5	7.6	7.2	7.8	7.2	7.3	6.7	6.7	5.8	7.8	6.12	6.2	5.8	5.65	6.0
1.23	1.23	1.29	1.3	1.30	1.19	1.28	1.3	1.29	1.04	1.46	1.45	1.6	1.3	1.48	1.5
4.7	4.7	4.8	5.0	5.1	5.0	5.0	4.8	4.4	4.7	5.3	4.02	4.1	4.0	4	4
3.2	3.0	3.5	3.5	3.5	3.4	3.4	3.2	3.2	2.9	3.4	2.24	2	2	2	2.4
1.0	1.2	2.0	1.5	1.3	1.8	1.9	1.7	1.5	0.9	1.4	1.12	0.9	1.0	1	1
1.53	1.51	1.61	1.7	1.68	1.59	1.60	1.6	1.57	1.55	1.73	0.96	1	1	0.8	1

20.4	20.5	19.6	21.8	20.8	20.5	21.0	19.5	20.4	19.7	19.8	10.05	8	16	10	11.8
				0.707419					0.707523						0.706803
				0.000007					0.000006						0.000005
				0.512291					0.512299						0.512367
				0.000006					0.000004						0.000004
				18.2093179					18.20258272						18.2164890
				0.0007					0.0010						
				15.6186259					15.61818768						15.6151545
				0.0006					0.0009						
				38.6359098					38.64562665						38.5802631
				0.0017					0.0023						

Sabancaya

Basal Sabancaya

SA-0906	SA-0915	SA-0918	SA-0926	SA-1147	SA-0924	SA-1150	SA-1152	SA-0911	SA-0912	SA-1149	SA-0917	SA-0921	SA-0922	SA-0934	SA-1148
East flank	East flank Sabancaya	East flank Sabancaya	W flank Sabancaya	NE of crater Sabancaya	W flank Sabancaya	NE flank Sabancaya	NE flank Sabancaya	East flank Sabancaya	SE flank Sabancaya	NE of crater Sabancaya	Flank NE Sabancaya volcano	W flank Sabancaya	W flank Sabancaya	NW flank Ampato	NE flank Sabancaya
8,248,272	8,253,513	8,250,933	8,251,693	8,252,138	8,251,829	8,253,585	8,253,165	8,254,122	8,250,147	8,255,222	8,255,870	8,252,921	8,251,850	8,252,006	8,253,552
197,456	199,052	198,619	187,176	2,000,121	190,508	198,579	199,534	198,900	194,428	196,406	196,910	192,220	191,886	191,086	197,841
Lava flow	Lava flow	Lava flow	Lava flow	Lava flow	Lava flow	Lava flow	Lava flow	Lava flow	Lava flow	Lava flow	Lava flow	Lava flow	Lava flow	Lava flow	Lava flow
61.0	64.9	62.1	61.8	63.66	60.1	63.9	61.4	61.6	61.55	62.8	60.7	60.1	60.8	59.65	61.8
0.95	0.73	0.93	0.90	0.8	0.99	0.78	0.97	0.96	0.9	0.86	1.01	1.01	0.96	1.07	0.96
16.2	15.5	16.2	16.2	14.47	16.6	15.69	15.59	16.4	15.83	16.167	16.1	16.6	16.2	16.55	16.475
5.63	4.17	5.34	5.22	4.54	5.73	4.09	5.29	5.52	5.588	4.82	6.10	5.93	5.61	6.23	5.62
0.08	0.06	0.07	0.07	0.06	0.07	0.06	0.07	0.07	0.07	0.06	0.08	0.07	0.07	0.08	0.07
2.92	1.96	2.40	2.31	1.91	2.54	2.33	2.48	2.52	2.91	2.34	3.03	2.91	2.77	2.81	2.60
5.32	3.77	4.76	4.67	3.73	5.29	3.92	4.64	5.22	5.04	4.53	5.38	5.52	5.16	5.45	5.14
4.17	4.12	4.36	4.35	4.07	4.41	4.13	4.30	4.25	4.08	4.23	4.18	4.28	4.18	4.43	4.291
2.80	3.50	3.03	3.05	3.312	2.71	3.49	2.98	2.79	2.875	3.11	2.63	2.56	2.78	2.68	2.84
0.29	0.23	0.33	0.30	0.30	0.34	0.27	0.37	0.30	0.27	0.29	0.30	0.30	0.29	0.38	0.34
0.24	0.52	0.29	0.30	0.7	0.19	0.49	0.15	0.13	0.2	0.34	0.19	0.07	0.16	0.24	-0.05
99.59	99.48	99.74	99.14	97.50	99.00	99.13	98.23	99.74	99.35	99.51	99.67	99.33	98.93	99.59	100.12
87.7	80.9	75.7	95.6	121.3	107.2	134.7	94.5	105.4	92.3	113.8	81.0	91.9	84.3	94.0	90.9
750.1	635.7	851.1	776.5	659.0	851.8	660.8	824.7	777.0	697.9	721.1	735.8	785.2	741.6	868.9	786.0
958.2	1051.5	1120.0	1030.7	976.3	1017.1	1172.4	1078.8	990.7	911.0	1052.7	886.4	920.6	959.3	1091.9	1018.0
11.2	7.5	9.2	8.6	7.1	9.5	7.9	8.8	9.5	10.7	8.4	10.5	10.1	10.0	10.7	9.3
134.1	89.0	122.3	121.2	101.0	134.1	85.2	120.4	126.9	129.8	106.8	145.7	138.0	127.1	146.2	130.0
48.3	21.2	32.3	32.2	30.5	35.3	22.9	37.5	39.5	50.6	27.6	71.5	62.6	53.4	39.5	40.3
17.6	12.7	15.7	14.9	13.5	16.9	13.8	16.2	16.2	17.6	14.3	19.3	18.5	17.1	18.0	16.7
30.2	18.5	24.3	23.7	20.4	26.6	20.5	25.7	25.2	31.5	21.5	41.8	36.5	32.9	29.2	25.1
13.7	12.5	12.6	12.3	9.9	12.5	12.5	10.9	12.8	12.9	12.0	13.0	12.4	12.9	13.1	12.3
99.9	67.8	134.2	119.2	11.4	145.1	12.8	12.1	119.0	98.1	12.4	116.2	117.2	109.5	167.4	12.5
7.9	8.5	8.2	8.7	8.3	7.8	8.2	7.7	7.3	7.3	7.6	7.3	7.2	7.7	8.1	7.4
35.3	39.4	41.8	37.5	42.4	37.1	40.6	42.7	34.6	35.1	37.1	32.1	32.2	33.3	38.5	36.6
71.9	79.8	84.6	75.0	81.2	76.1	82.5	89.8	72.6	70.4	74.4	70.5	66.8	72.0	76.3	74.3
32.4	32.2	36.2	32.5	35.0	34.2	34.9	38.2	32.3	31.6	32.4	31.5	31.1	31.5	35.7	34.1
5.8	5.7	6.5	5.8	6.3	6.1	6.0	6.7	6.0	5.4	5.6	5.7	5.7	5.6	6.3	5.8
1.4	1.2	1.5	1.4	1.4	1.6	1.3	1.7	1.5	1.4	1.4	1.4	1.5	1.4	1.6	1.5
4.0	3.8	4.1	3.9	4.1	4.1	4.2	4.4	3.9	4.2	3.9	4.1	3.7	4.1	4.4	4.2
2.5	2.3	2.4	2.3	2.4	2.4	2.4	2.7	2.4	2.6	2.4	2.4	2.3	2.4	2.6	2.6
1.1	1.2	1.1	0.9	0.9	1.2	0.9	1.1	1.0	0.8	0.9	1.1	1.0	1.1	1.1	0.9
1.0	1.0	1.0	0.9	1.0	0.9	1.0	1.0	1.0	1.0	1.0	1.0	0.9	1.0	1.0	1.0

9.8	14.3	9.7	10.4	14.5	7.7	15.0	9.9	9.3	10.6	12.3	8.9	8.3	9.3	6.7	9.7
	0.707020									0.706888		0.706751		0.7065126	
	0.000006									0.000005		0.000006		0.000007	
	0.512343									0.512360		0.5123661		0.51240245	
	0.000005									0.000005		0.000010		0.000006	
	18.2119475									18.2245992		18.25375		18.3646968	
	0.0008											0.0005		0.0007	
	15.6175308									15.6141503		15.61592		15.6225128	
	0.0008											0.0005		0.0006	
	38.5770296									38.5800146		38.57911		38.6366061	
	0.0022											0.0020		0.0019	

								Terminal Cone				2017-2018 Activity			
SA-0916	SA-0909	SA-1015	SA-1153	SA-0904	SA-0908	SA-0910	SA-0920	SA-0907	SA-0914	SA-0905	SA-0919	SA-1701	SA-1810	SA-1811	SA-1812
East flank Sabancaya	N flank Sabancaya	SE flank Sabancaya	NE of crater Sabancaya	South dome of Sabancaya	East flank Sabancaya	East flank Sabancaya	East flank Sabancaya	NE flank Sabancaya	East flank Sabancaya	East flank Sabancaya	W flank Sabancaya	SE flank Sabancaya	SE flank Sabancaya	SE flank Sabancaya	SE flank Sabancaya
8,250,440	8,255,474	8,248,962	8,255,567	8,251,215	8,248,067	8,247,323	8,250,471	8,252,810	8,251,054	8,252,631	8,252,245	8252130	8252344	8252221	8252374
196,444	193,838	195,836	196,923	193,257	198,395	199,617	198,738	194,470	194,713	194,966	192,587	194412	194350	194322	194290
Lava flow	Lava flow	Lava flow	Lava flow	Lava flow	Lava flow	Lava flow	Lava flow	Lava flow	Lava flow	Lava flow	Lava flow	Block juvenile	Block juvenile	Block juvenile	Block juvenile
62.1	62.0	63.6	62.9	61.9	61.7	60.7	60.7	61.1	64.7	61.8	62.5	60.2	60.82	61.18	60.95
0.90	0.90	0.78	0.91	0.90	0.91	1.00	0.95	0.95	0.73	0.94	0.87	1.00	0.92	0.95	0.94
16.1	16.2	15.2	16.114	16.0	15.9	16.6	16.5	16.3	15.6	16.3	15.8	16.2	16.58	16.44	16.40
5.39	5.25	4.74	5.16	5.41	5.32	5.77	5.67	5.63	4.01	5.42	5.15	6.2	5.73	5.89	5.88
0.07	0.07	0.07	0.06	0.07	0.07	0.07	0.07	0.07	0.06	0.07	0.07	0.076	0.08	0.08	0.08
2.41	2.33	2.12	2.11	2.44	2.39	2.91	2.85	2.51	2.05	2.50	2.26	2.74	2.50	2.66	2.56
4.86	4.77	4.06	4.53	4.82	4.70	5.48	5.28	5.04	3.85	5.01	4.54	5.46	5.58	5.48	5.55
4.21	4.22	4.25	4.25	4.28	4.31	4.27	4.29	4.20	4.09	4.26	4.14	4.34	4.40	4.35	4.36
2.94	2.99	3.35	3.17	3.00	3.13	2.65	2.74	2.85	3.48	2.92	3.03	2.63	2.57	2.67	2.51
0.28	0.28	0.25	0.32	0.29	0.31	0.31	0.30	0.30	0.23	0.30	0.27	0.337	0.34	0.33	0.34
0.27	0.27	0.36	0.17	0.43	0.48	0.15	0.19	0.15	0.45	0.19	0.25	0.09	0.08	0.10	0.11
99.51	99.25	98.77	99.69	99.55	99.17	99.82	99.52	99.16	99.34	99.77	98.84	99.22	99.59	100.13	99.69
99.0	65.3	73.8	119.6	80.2	106.0	80.0	94.0	77.1	131.0	111.6	110.2	78	66.5	70.0	62.0
732.3	719.8	632.5	717.6	790.5	790.3	842.3	807.5	783.9	642.6	778.9	687.4	823	887.6	808.7	863.3
988.0	1036.4	1001.3	965.5	995.0	1127.6	1009.5	982.6	1033.2	1102.5	1030.8	992.7	998	990.6	1004.4	969.4
9.6	9.2	8.6	7.8	9.5	9.3	10.3	10.2	10.0	7.7	10.2	9.0	9.7	8.9	9.2	9.3
123.3	120.5	104.2	111.2	125.0	119.7	132.4	128.8	132.8	84.0	125.2	115.4	144	135.5	138.7	139.6
37.3	26.9	32.9	29.7	44.0	36.3	59.3	53.4	30.6	20.1	23.1	33.0	43.1	39.3	38.1	39.3
15.3	15.4	13.2	14.9	15.6	15.0	18.1	18.3	16.7	12.8	16.8	14.7	19.3	16.9	18.0	17.4
23.4	20.3	20.9	22.5	24.0	23.0	34.3	33.5	26.3	18.6	22.3	23.2	27.6	24.1	24.5	25.3
13.0	12.8	12.7	12.0	12.7	12.7	12.2	12.5	12.9	12.5	13.3	12.6	13.8	9.6	9.5	9.8
120.3	120.0	83.9	12.3	109.7	129.5	121.3	111.9	130.7	64.6	126.1	106.8	148	131.2	139.4	132.9
8.3	7.4	8.3	7.6	7.8	8.8	7.4	7.4	7.3	8.6	7.6	8.2	7.7	6.7	7.4	6.2
36.1	35.5	38.6	37.2	37.0	41.0	34.0	34.4	35.9	38.1	36.5	35.5	34.4	35.2	35.1	34.9
73.5	74.9	77.3	79.6	74.8	83.9	68.6	74.1	75.7	76.4	77.0	76.3	70.4	71.5	74.3	71.6
32.8	32.2	31.9	34.7	32.3	35.4	32.6	31.4	33.1	31.4	33.6	32.0	32.3	32.7	33.2	32.3
5.9	5.6	5.9	6.4	5.7	6.2	5.8	5.8	6.1	5.8	5.9	5.6	5.8	5.6	5.7	5.2
1.4	1.4	1.2	1.5	1.4	1.4	1.5	1.5	1.5	1.2	1.4	1.3	1.27	1.4	1.3	1.4
4.1	3.8	3.8	4.2	4.1	4.0	4.2	3.6	4.3	3.9	4.1	3.9	4.5	4.3	4.4	4.1
2.4	2.4	2.3	2.5	2.4	2.3	2.3	2.4	2.3	2.2	2.5	2.4	2.5	2.2	2.2	2.2
1.1	1.0	1.0	0.9	0.9	0.8	1.2	1.0	1.0	0.9	1.0	1.1	0.6	1.0	1.1	1.1
1.0	1.0	1.0	1.0	1.0	1.0	0.9	0.9	1.0	0.9	1.0	0.9	0.98	0.9	0.9	0.9

10.3	10.1	13.2	11.9	10.2	10.0	8.0	9.0	8.9	13.6	9.1	11.0	7.2	7.1	7.2	7.1
				0.706723		0.706723			0.707012			0.706695		0.706724	
				0.000007		0.000007			0.000005			0.000004		0.000006	
				0.512366		0.512366			0.512343			0.512371		0.512365	
				0.000005		0.000005			0.000003			0.000003		0.000002	
				18.2302636					18.1922663			18.2736840		18.2699870	
				0.0005											
				15.6143535					15.6142880			15.6186422		15.6155008	
				0.0005											
				38.5700707					38.5660087			38.6066403		38.5975522	
				0.0010											

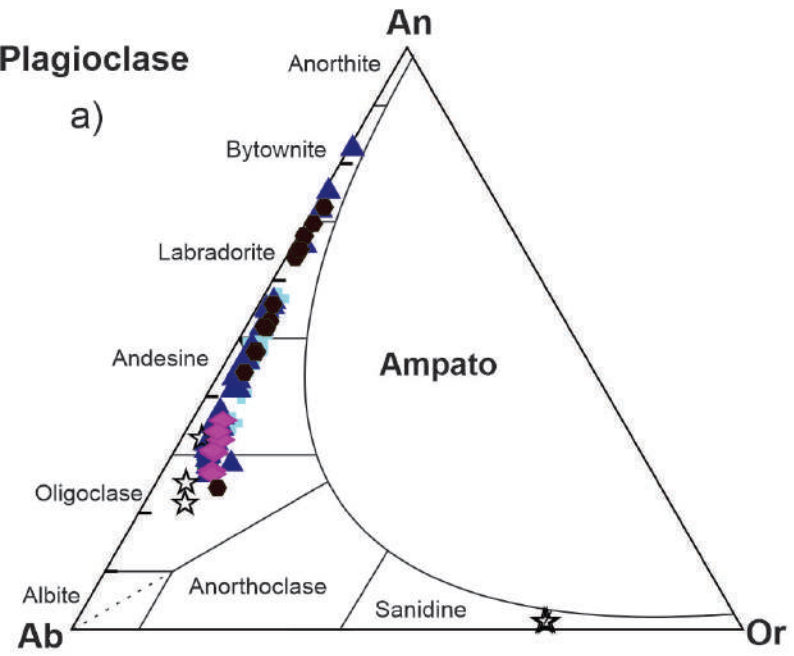
Plagioclase
a)
An
Anorthite
Bytownite
Labradorite
Andesine
Oligoclase
Albite
Ab
Anorthoclase
Sanidine
Or
Ampato

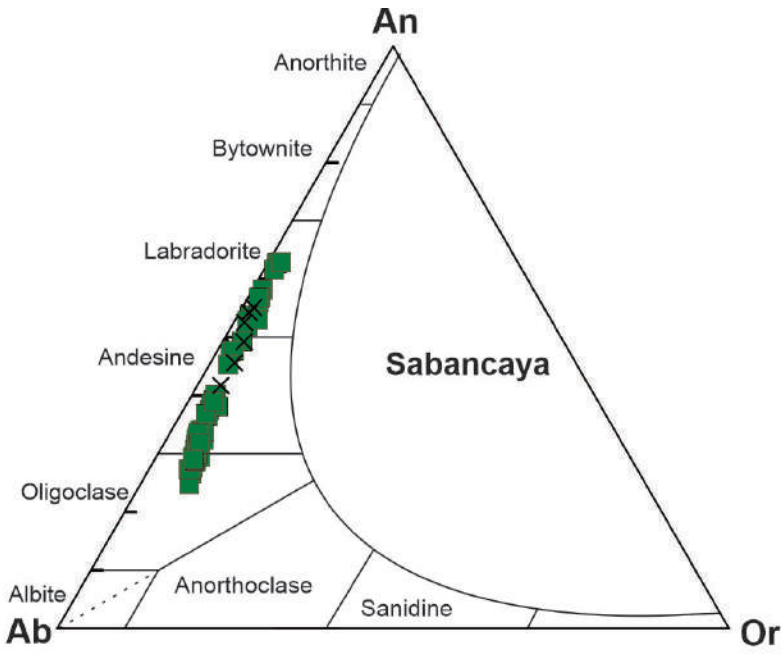
An
Anorthite
Bytownite
Labradorite
Andesine
Oligoclase
Albite
Ab
Anorthoclase
Sanidine
Or
Sabancaya

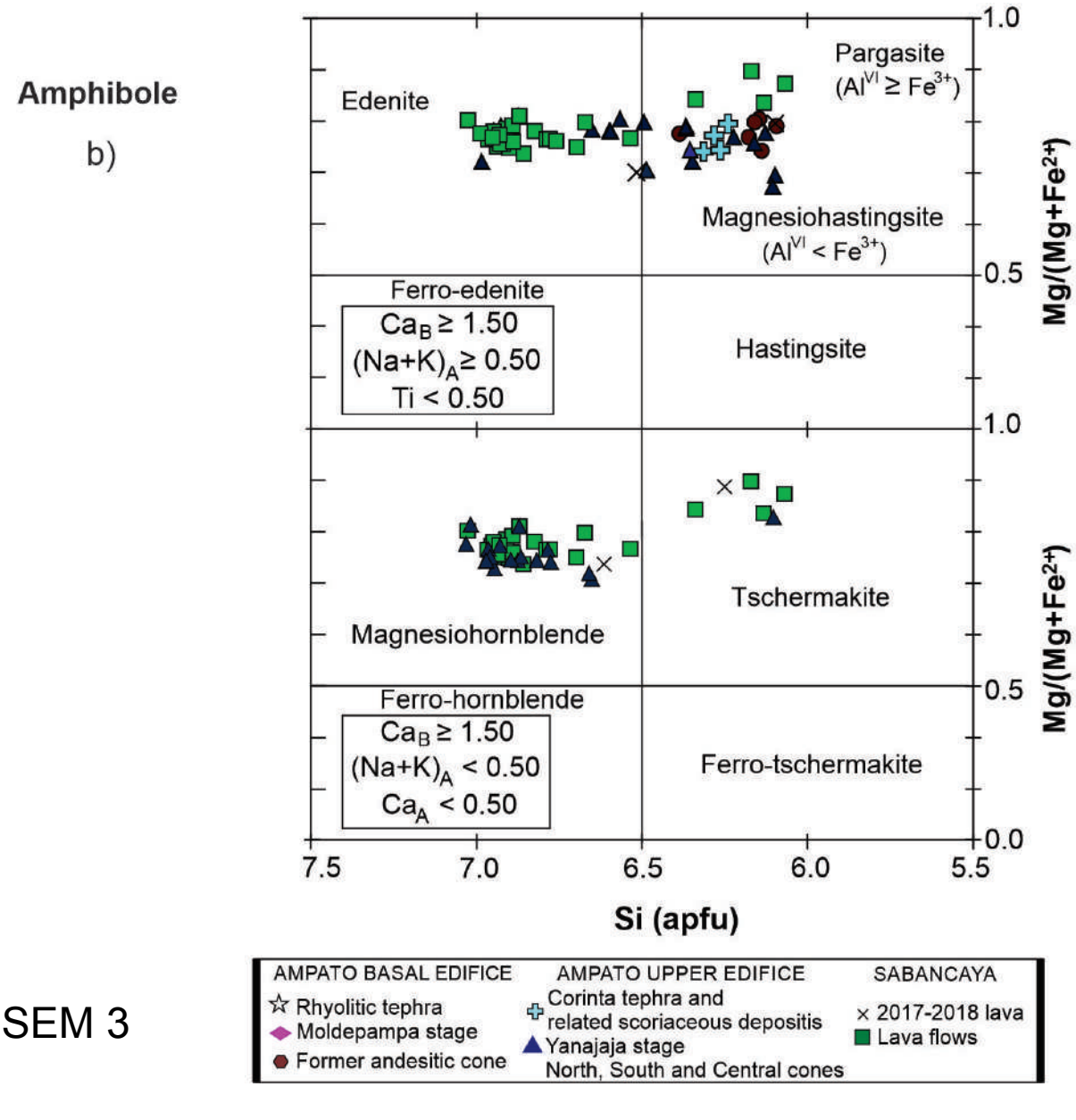
Amphibole
b)
Edenite
Pargasite
(Al^VI ≥ Fe^3+)
Magnesiohastingsite
(Al^VI < Fe^3+)
Ferro-edenite
Ca_B ≥ 1.50
(Na+K)_A ≥ 0.50
Ti < 0.50
Hastingsite
Tschermakite
Magnesiohornblende
Ferro-hornblende
Ca_B ≥ 1.50
(Na+K)_A < 0.50
Ca_A < 0.50
Ferro-tschermakite
1.0
0.5
1.0
0.5
0.0
Mg/(Mg+Fe2+)
Mg/(Mg+Fe2+)
7.5
7.0
6.5
6.0
5.5
Si (apfu)
AMPATO BASAL EDIFICE
Rhyolitic tephra
Moldepampa stage
Former andesitic cone
AMPATO UPPER EDIFICE
Corinta tephra and related scoriaceous depositis
Yanajaja stage
North, South and Central cones
SABANCAYA
2017-2018 lava
Lava flows

SEM 3

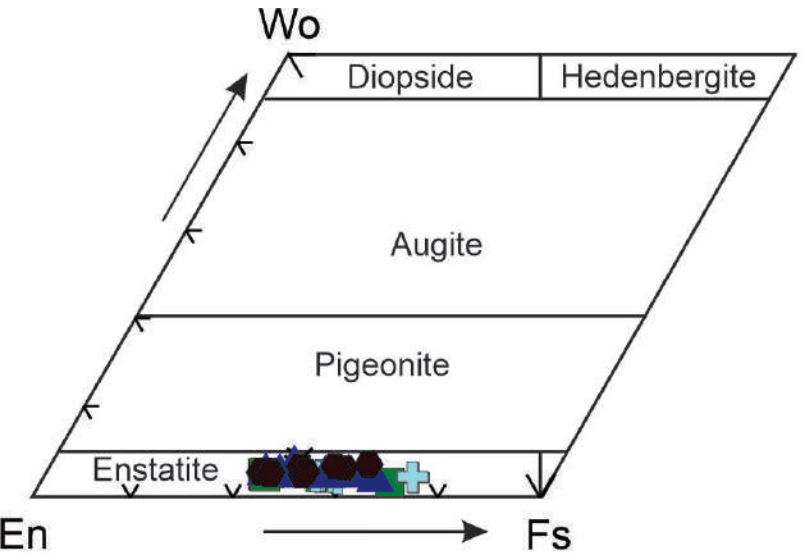

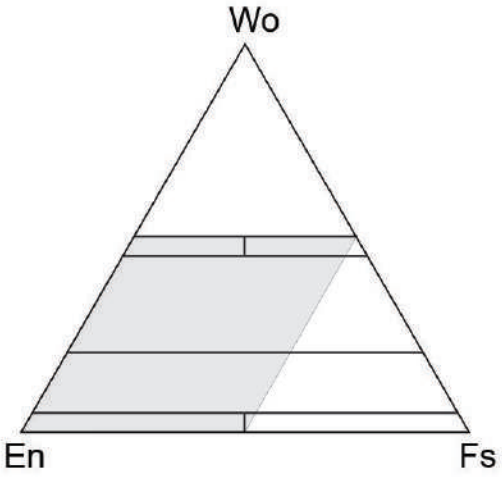

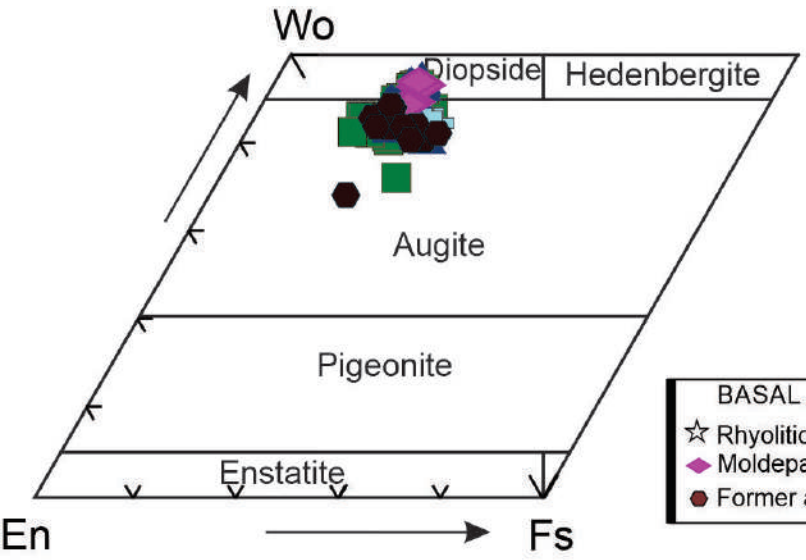

BASAL AMPATO
- ☆ Rhyolitic tephra
- ◆ Moldepampa stage
- ● Former andesitic cone

UPPER AMPATO
- ✚ Corinta tephra and related scoriaceous depositis
- ▲ Yanajaja stage North, South and Central cones

SABANCAYA
- × 2017-2018 lava
- ■ Lava flows

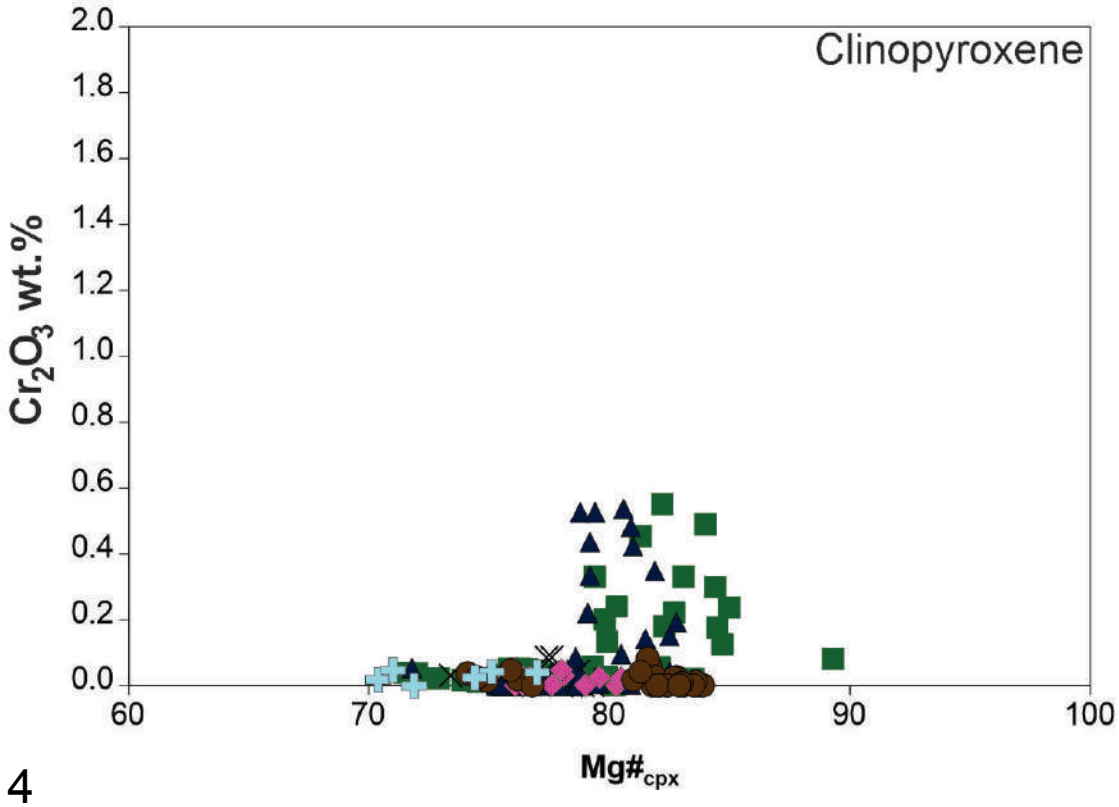

SEM 4